ALMA MATER STUDIORUM - UNIVERSITÀ DI BOLOGNA

Facoltà di Scienze Matematiche Fisiche e Naturali
Dottorato di Ricerca in Fisica, XIX Ciclo
Area 02 - Scienze Fisiche: FIS/04 Fisica Nucleare e Subnucleare

PhD Thesis

Cosmic Rays Anti-Deuteron Flux Sensitivity of the AMS-02 Detector

Francesca Giovacchini

Advisor:
Prof.
Federico Palmonari

External Advisor:
Dr.
Vitali Choutko

PhD Coordinator:
Prof.
Fabio Ortolani

Bologna, Italy, 2007

Contents

Introduction

The *Alpha Magnetic Spectrometer* (AMS) experiment is a space-borne high energy particle detector aimed at making a high precision measurement of Cosmic Ray (CR) and gamma fluxes at low Earth orbit from few hundred MeV/n up to few TeV/n. AMS-02, 7 tons superconducting spectrometer, developed by a world-wide international collaboration, will be ready at the end of 2008 to be installed on the International Space Station (ISS), where it will operate for at least three years.

In the last few decades the presence of antimatter in CR, namely antiprotons and positrons, has been confirmed through the measurement of their spectra with balloon-borne and space experiments. Indeed, light antinuclei, mostly antiprotons but also antideuterons, are produced in our galaxy as secondaries, mainly from the interaction of primary protons with the interstellar medium (ISM) of the Milky Way disc.

New exotic sources of these CR species could come from some Dark Matter (DM) candidates. A variety of experimental evidences, both from cosmology and astrophysics, points to the existence of "missing matter" in the Universe, but its nature is still a mistery. Recent results on Cosmic Microwave Background (CMB) measurements indicate that DM contributes to about 23% of the Universe energy density. At the same time, strong arguments based on Big Bang nucleosysthesis, large structure formation, cosmological measurments and the observations of several rotational galactic curves essentially constrain the search to non-baryonic Cold Dark Matter.

No known particle in the Standard Model of particle physics (SM) can fulfil this role and so new candidates should be found in new theories. Going beyond the SM, among the different candidates, the most studied one is nowadays the Lightest Supersymmetric Particle (LSP), arising from the suspersymmetric extensions of the SM (SUSY models). If the DM was made of the neutralinos, the most favorite LSP particle, one could hope to detect them indirectly through an excess of gamma rays, positrons, antiprotons and light antinuclei with respect to the known CR fluxes.

For kinematical reasons, antideterons from neutralino annihilation are expected to populate mainly the low energy band, whereas secondary antideuterons are produced with relatively higher energy. As a matter of fact, the fusion processes, which produce antideuterons from the merging of antiprotons and antineutrons, are favoured at low anergy, and this enhances the antideuteron formation from neutralino annihilation with respect to that from secondary origin. On the other hand, existent antiprotons data

are very well explained by secondary production in CRs, making the extraction of an eventual supersymmetric signal much more difficult. Therefore, antideuterons with kinetic energy below about 1 GeV/n are a much better probe for SUSY DM than antiprotons. Unfortunately, the antideuteron signal is very small with regard to the primary cosmic rays fluxes and even to that of antiprotons.

A very large acceptance spectrometer in space, with long exposure time and good particle identification, like AMS-02, is therefore required.

Aware of the importance of this topic, the AMS collaboration encouraged me to study the sensitivity of AMS-02 detector to this physics channel. This thesis decribes the detection capability of our experiment for rare events like antideuterons.

In the first chapter an overview of the CR physics and of the DM framework in which the antideuteron signal emerges as a promising probe for the DM indirect detection is given, together with a description of its features and theoretical basis.

The AMS-02 experiment is presented in the second chapter, where all its main subsystems and their detection capabilities are considered in detail.

Chapter 3 focuses on the Time of Flight (TOF) detector, whose particle velocity measurement is crucial for the low energy antideuteron detection. Some relevant results of the analysis of the TOF particle detection performance, as well as, of the study of its behaviour and stability under space conditions are provided.

Inelastic interactions for deuterons and antideuterons inside the detector have been introduced in the official AMS-02 MC code; the models and theoretical assumptions adopted to describe their cross section are discussed in chapter 4.

Chapter 5 concerns the selection criteria applied to the AMS-02 MC data in order to identify a clean sample of antideuteron, finding its detector acceptance and minimizing the background contamination. The minimal detectable flux for AMS-02 in three years of data taking is finally estimated and compared to the more recents prediction in literature for antideuteron flux, both produced from standard and from exotic sources.

Chapter 1

Antimatter in galactic Cosmic Rays

1.1 Presence of antimatter in Cosmic Rays

1.1.1 Introduction to Cosmic Rays

Cosmic Rays (CR) are charged particles coming to the Earth from all directions. They constitute a genuine sample of galactic matter, spanning a very wide energy range (from several MeV up to 10^{20} eV), consisting mainly of protons ($\sim 90\%$), but also of Helium nuclei ($\sim 9\%$), electrons ($\sim 1\%$), all other nuclei and antiparticles like antiprotons and positrons [1]. In addition to charged particles, also a detectable flux of energetic photons and neutrinos is present.

Cosmic rays can have different origins: some of them, called *primaries*, come unaltered from astrophysical sources, the others, called *secondaries*, are produced by inelastic scattering of primaries (*spallation* reactions) on the interstellar medium (ISM) or from the disintegration of unstable species.

Figure 1.1 shows the CR spectra of some important nucleic components. CR flux is fastly decreasing when energy increases following a power law with very few structures. First, at low energy the spectrum flattens and the flux reaches the maximum, because it is dumped by the solar wind (solar modulation). Indeed, the energy spectrum of galactic cosmic rays is influenced by the solar activity, which oscillates following the 11 year solar half-cycles. For kinetic energy higher than few GeV per nucleon, the energy spectrum is well described by a power law:

$$\frac{\mathrm{d}N(E)}{\mathrm{d}E} \propto E^{-\gamma} , \tag{1.1}$$

where γ is the spectral index, which is about 2.7 for all nuclei below the so called *knee* positioned around 4 PeV, where the spectrum steepens and the spectral index becomes equal to 3. The spectrum smoothly increases the slope up to few 10^{18} eV, corresponding to the *ankle*, where γ is around 2.5. Changes in the spectral index of the CR spectrum reflect the different origin and the propagation history of cosmic rays with different energy. In
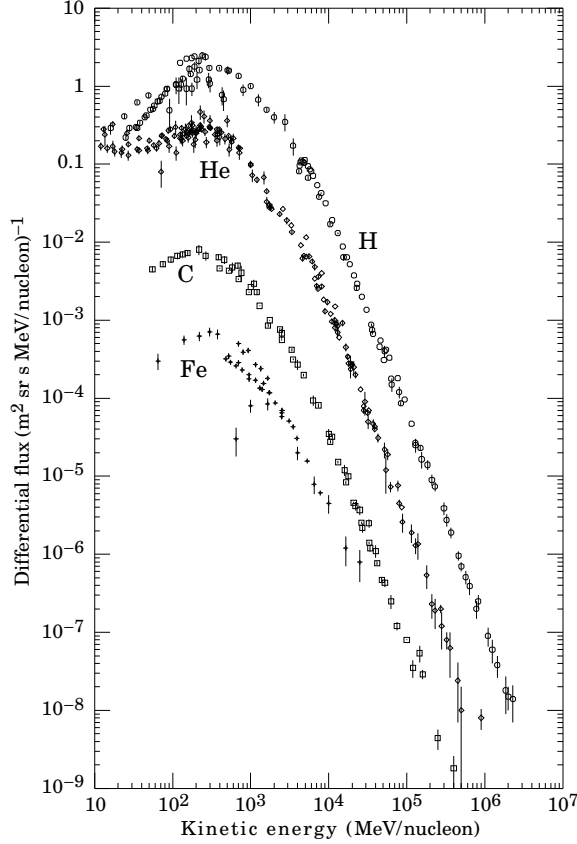
Figure 1.1: Measured differential flux for primary cosmic rays component: hydrogen, helium, carbon, and iron nuclei [2].

particular below the knee their curvature radius is smaller than the galactic disc thickness, hence their sources must belong to our Galaxy, where CR propagate by diffusion. In that energy range the sources are strongly suspected to be supernovae (SN) remnants [1].

1.1.2   Experimental evidence

Light antinuclei, mostly antiprotons but also antideuterons are produced in our galaxy as secondaries. They result from the interaction of high energy cosmic rays protons with the interstellar gas of the Milky Way disc. The first experimental evidence for the presence of antiprotons in cosmic rays goes back to 1979 [3], but the detector particle identification was inadequate and the measurements were compromised by background. Unambiguous detections of cosmic-ray $\overline{p}$s were performed by subsequent baloon-borne experiments like BESS93 [4] in the low-energy region (4 events betwee 0.3 and 0.5 GeV), which was followed by IMAX [5] and CAPRICE [6] detections. After BESS95 [7] results have been improved by BESS97 with the measurement of the $\overline{p}$ spectrum in the range 0.18 to 3.56 GeV, based
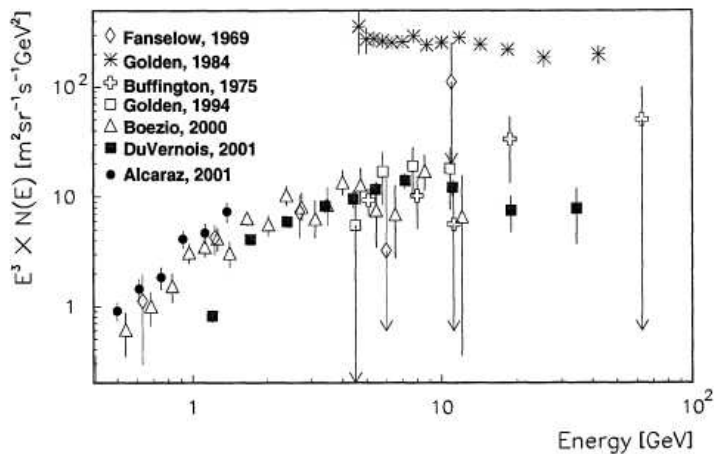
Figure 1.2: Compilation of positron flux measurements [9].

on 458 $\overline{p}$s collected during recent solar-minimum period [8]. A distinctive peak at 2 GeV in the $\overline{p}$ spectrum was detected, as expected by theoretical calculations for $\overline{p}$ originating from cosmic-ray interactions with the interstellar gas, to conclude that secondary component is dominant in CR antiprotons. A collection of experimental data on the antiproton spectrum, compared to some theoretical flux derived as described in the next section, will be shown in figure 1.4(b). On the other hand, so far no antideuterons or heavier antinuclei have been detected in Cosmic Rays.

Electrons and positrons are also present in CRs, but they have to be considered separately because of the absence of hadronic interactions and the significant electromagnetic energy loss during their propagation through the galaxy. These interactions make e^- and e^+ energy spectra much steeper than that of the other CR nuclei, resulting in a refractive index greater than 3 [10]. In the current understanding of the high energy lepton spectra in cosmic rays, they are dominated by the electron component. High energy electrons are believed to mainly originate from primary sources. Since secondary electrons and positrons are produced in pairs, the measured fraction $e^+/(e^+ + e^-)$ of the order of 10% in the region between 1 and 10 GeV indicates the presence of primary electrons and secondary electrons and positrons. The primary contribution to positron flux is difficult to be separated from the secondary one, because of uncertanties in the production mechanism. Data on CR electrons and positrons flux have been collected since 1970s, but reliable results come from the experiment CAPRICE94 and HEAT. A total of 3211 electrons, with a rigidity at the spectrometer between 0.3 and 30 GV, and 734 positrons, between 0.3 and 10 GV, were detected by CAPRICE94 [11]. HEAT experiment provided a measurement of the positrons spectrum in a wider energetic range [12] and a compilation of the collected data on positron flux is shown in figure 1.2. A slight indication of an eccess

in positron spectrum has been seen but new data with more statistics and good particle identification in a wide energetic range are necessary.

1.1.3   Expectations from astrophysical processes

As already observed light antinuclei and positrons are expected in Cosmic Rays from standard astrophysical sources as secondary products of spallation processes occurring during their diffusion in the Galaxy. CRs are diffused by the inhomogeneities of the magnetic field and many theoretical approaches may be adopted to model the galactic CR transport [1, 13].

The so called Leaky Box model and Slab model are extensively used in most of the theoretical works in this field. In the simplest model, namely Leaky Box model, the Galaxy is described as a finite propagation volume, delimited by a surface. Inside this volume each nucleus has a probability per unit time $1/\tau_{esc}$ to escape from the box and the densities of sources, interstellar matter and cosmic rays are considered homogeneous. This model is able to succesfully explain most of the observed CR stable fluxes using a single effective phenomenological parameter τ_{esc}.

In the Slab model, the number of nuclei of a given species have crossed a certain *grammage* is related to the destruction rate from inelastic collisions and the creation rate from spallation of all heavier nuclei. The grammage (in g cm^{-2}) has been introduced to express the column density of the matter crossed by the CR particle. Refined weighted Slab approaches have been also introduced and they are able to link Leaky Box models with more realistic diffusion models, explaining why Leaky Box works so well.

Diffusion Models represent a more realistic description of CR propagation. Astrophysical sources and interactions are considered to be confined in the thin galactic disc of $h \sim 100$ pc, while diffusion may occur both in disc and in halo. The diffusive halo is modelled as a cylinder of radius $R = 20$ kpc and half height L. The Solar system is located in the galactic disc ($z = 0$) at a distance $R_\odot = 8$ kpc from the Milky Way center as is shown in the schematic view of figure 1.3. Taking advantage of the cylindrical symmetry and assuming steady-state (no time dependance), the transport equation can be written for each species j:

$$K(E)\left(\frac{\partial^2}{\partial z^2} + \frac{1}{r}\frac{\partial}{\partial r}(r\frac{\partial}{\partial r})\right)N^j(E,r,z) - V_c\frac{\partial}{\partial z}N^j(E,r,z) \tag{1.2}$$

$$+2h\delta(z)\big(q_0 Q(E)q(r)\big) + 2h\delta(z)\left(\sum_k^{m_k > m_j} \Gamma^{kj}N^k(E,r,0) - \Gamma^j N^j(E,r,0)\right)$$

$$= 2h\delta(z)\frac{\partial}{\partial E}\left\{b^j(E)N^j(E,r,z) - d^j(E)\frac{\partial}{\partial E}N^j(E,r,0)\right\},$$

where $N^j(E) = \mathrm{d}n^j/\mathrm{d}E$ is the CR differential function, with n^j the total cosmic ray
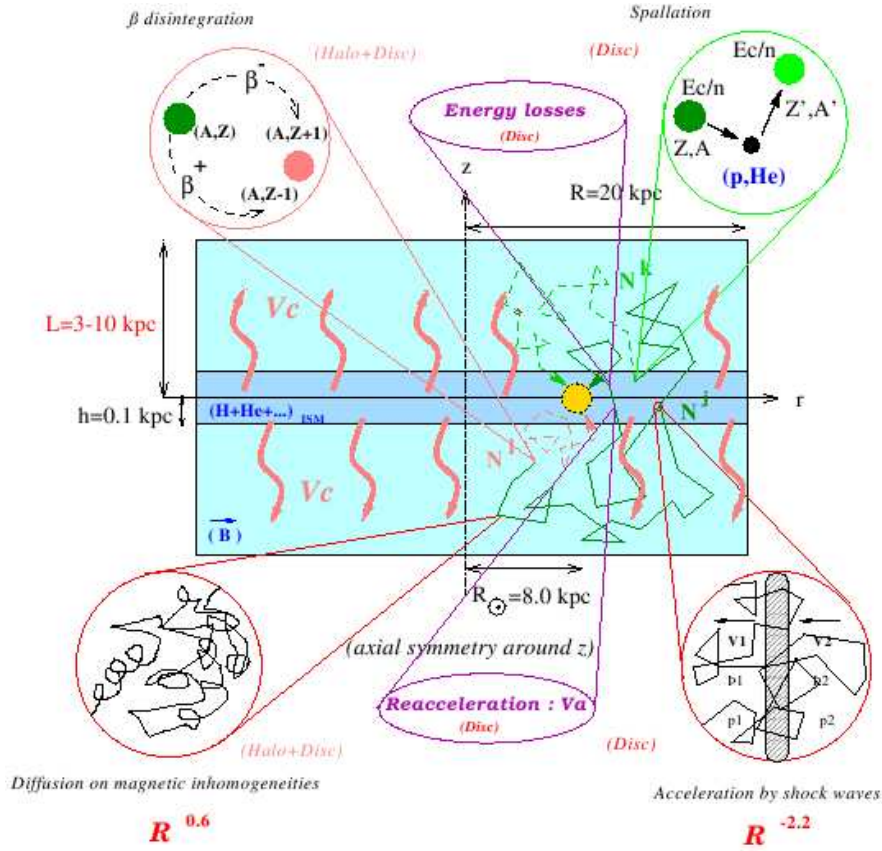
Figure 1.3: Schematic view of our Galaxy and physical processes affecting propagation (Ref. [13]).

number density of nucleus j. The quantities present in this equation are functions of spatial coordinates and of kinetic energy per nucleon E, which is the appropriate parameter to be used since it is conserved in spallation reactions. All the effects which play a relevant role in CR propagation are included in formula 1.2 where the following terms are listed in order: diffusion, convection, acceleration, nuclear reactions (spallation) and energy losses–reacceleration.

- The first is the diffusion term containing the coefficient K, that in principle should be replaced by a tensor, with parallel and transverse components, but, since the diffusion is usually assumed isotropic, we consider it as:

$$K(E) = K_0 \beta R^\delta \ ,$$

where the normalization constant K_0 and the spectral index δ are related to the astrophysical properties of the interstellar medium, that are quite unknown at the present time, and so they are indirectly derived by the analysis of cosmic ray observations.

- The medium responsible for diffusion is moving away from the disc, with a velocity V_c. This so called *convective* or *galactic wind* has the effect to dilute the energy of the particle located in the disc in a larger volume.

- Primary sources are included in the source term (third term in equation 1.2) depending on the normalized abundance q_0 and on the spectrum $Q^j(E)$. Secondary production coming from spallation or radioactive decay of a heavier species is counted in the following spallation term:

$$2h\delta(z) \sum_{k}^{m_k > m_j} \Gamma^{kj} N^k(E, r, 0) \ .$$

- Spallation processes are governed by the reaction cross sections with ISM of CR particles crossing the disc. The universal parameterization formula used to model such nucleus-nucleus interaction will be treated in detail in chapter 4. In order to derive not only the destruction rate but also the formation rate of new nuclei, the knowledge of the branching ratio into a particular channel is required.

- In the last term of equation 1.2 ionization losses and Coulomb energy losses in a completely ionized plasma are considered for CR nuclei. Also the reacceleration process is included and it is related to the Alfvén velocity V_a, the velocity of disturbances in the hydrodynamical plasma.

Finally, the free parameters of the model are: the diffusion coefficient $K(E) = K_0 \beta R^\delta$, the convective velocity V_c, the Alfven velocity V_A, the diffusive halo thickness L and the acceleration spectrum $Q(E)$. In order to find the solution it is necessary to solve a complete set of coupled equations, strating from the heaviest nucleus down to hydrogen. The spatial part can be solved analytically in cylindrical symmetry using expansion on Bessel functions. The second order energy-dependent diffusion equation must be solved numerically.

Recently, a careful and detailed examination of the galactic antimatter production has been done [14], where the $\overline{p}$ and $\overline{d}$, as well as $\overline{t}$, $^3\overline{He}$, and $^4\overline{He}$ flux in orbit near Earth has been evaluated. The results obtained are reported in figure 1.4(a). In these calculations are introduced the available hadronic production data for these particles and the proven coalescence model that will be treated in § 1.5.2. In particular the last accurate parametrization of the inclusive antiproton production cross section has been included.

To derive the expected antimatter flux not only secondary production of primary CRs with ISM, but also the rescattering of the secondary particles on the ISM during propagation have been taken into account. Indeed the contribution of the last process to the low momentum flux of CR particles is relevant. Hence secondary $Q_{\overline{A}}^{\mathrm{sec}}$ and tertiary $Q_{\overline{A}}^{\mathrm{ter}}$ source terms are included to consider, in the first case, the net creation of the antinucleus $\overline{A}$

(a)   (b)
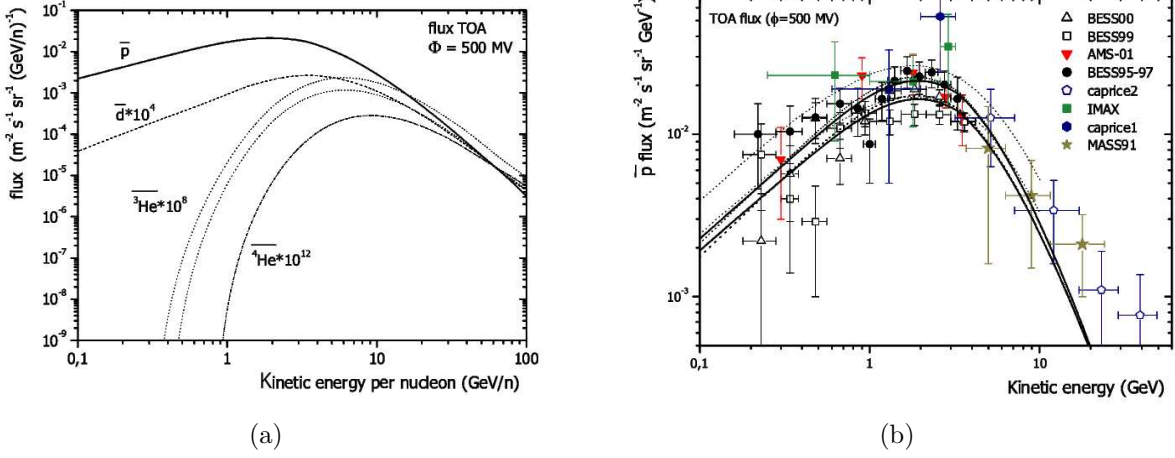
Figure 1.4: a) Galactic flux expected for $\overline{\mathrm{p}}$, $\overline{\mathrm{d}}$, $^3\overline{\mathrm{He}}$ and $^4\overline{\mathrm{He}}$ antimatter particles [14]. b) Collected experimantal data on antiproton flux superimposed onto the expected spectra as it is derived in Ref. [14]. The flux correponding to the single $\mathrm{pp} \to \overline{\mathrm{p}}X$ reaction without (solid line) and with (dashed line) the tertiary source contribution is plotted; the dotted line is referred to DTUNUC simulation code.

from CR interaction on the ISM, and second, the energy redistribution, through inelastic non-annihilating (NAR) reactions, of the produced antinuclei.

In the case of antiprotons, the secondary source term is given by:

$$Q^{\mathrm{sec}}(T_{\overline{\mathrm{p}}}) = 2 \sum_{i=\mathrm{CRs}}^{\mathrm{p,He,CNO}} \sum_{j=\mathrm{ISM}}^{\mathrm{H,He,CNO}} 4\pi n_j \int_{6m_{\mathrm{p}}}^{\infty} \frac{\mathrm{d}\sigma^{\mathrm{i+j}}}{\mathrm{dT}_{\overline{\mathrm{p}}}}(T_{\overline{\mathrm{p}}}, T_i)\Phi_i(T_{\mathrm{i}})\mathrm{dT}_{\mathrm{i}} \ , \tag{1.3}$$

where n_j is the number density of the considered nucleus in the ISM in cm^{-3} and $\mathrm{d}\sigma^{ij}/\mathrm{dT}_{\overline{\mathrm{p}}}$ is the differential antiproton production cross section. For the antiproton flux, the p–p reaction contributes about 56% to the $\overline{\mathrm{p}}$ production, the p–He up to 24%, the He–p up to 12%, and the He–He reaction up to 6%. The reactions p–CNO and CNO–p contribute to less than 2%, while He–CNO and CNO–He have been neglected because of the very low CNO nuclei flux and IS density.

The tertiary source term can be written as:

$$Q^{\mathrm{ter}}(T_{\overline{\mathrm{p}}}) = 4\pi n_{\mathrm{p}}\Bigg(\ 2 \ \int_{T_{\overline{\mathrm{p}}}}^{\infty} \frac{\mathrm{d}\sigma^{\overline{\mathrm{p}}\mathrm{p}\to\overline{\mathrm{p}}\mathrm{X}}}{\mathrm{dT}_{\overline{\mathrm{p}}}}(T'_{\overline{\mathrm{p}}}, T_{\overline{\mathrm{p}}})\Phi_{\overline{\mathrm{p}}}(T'_{\overline{\mathrm{p}}})\mathrm{dT}'_{\overline{\mathrm{p}}}$$

$$- \ 2\sigma_{in}^{\overline{\mathrm{p}}\mathrm{p}\to\overline{\mathrm{p}}\mathrm{X}}(T_{\overline{\mathrm{p}}})\Phi_{\overline{\mathrm{p}}}(T_{\overline{\mathrm{p}}}) \Bigg) \ , \tag{1.4}$$

where $\mathrm{d}\sigma^{\overline{\mathrm{p}}\mathrm{p}\to\overline{\mathrm{p}}\mathrm{X}}/\mathrm{dT}_{\overline{\mathrm{p}}}$ is the differential inelastic non-annihilating cross section for $\overline{\mathrm{p}}$s with incident energy $T_{\overline{\mathrm{p}}}$ emerging from the collision with an energy $T_{\overline{\mathrm{p}}} < T'_{\overline{\mathrm{p}}}$ and $\sigma_{in}^{\overline{\mathrm{p}}\mathrm{p}\to\overline{\mathrm{p}}\mathrm{X}}$ is
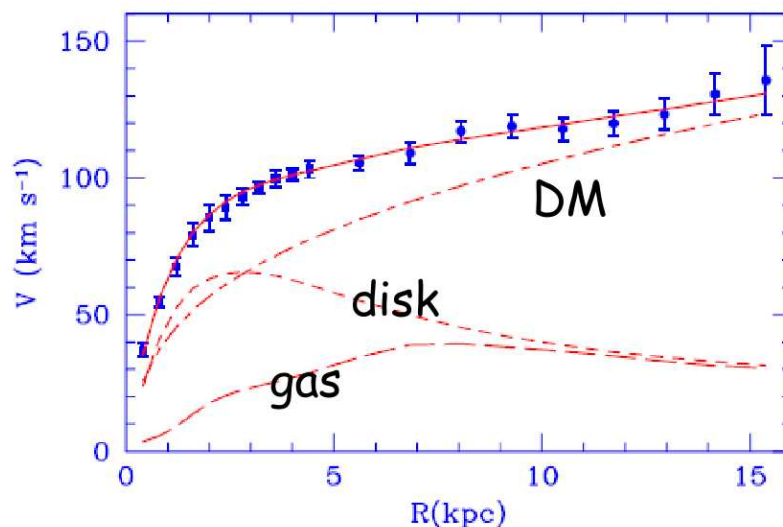
Figure 1.5: Rotation curve of M33 galaxy-M33. To the known distribution of luminous matter in the galactic disc and of gas, an additional contribute of Dark Matter in the halo is required to reproduce experimental points [16].

the total inelastic scattering cross section for $\overline{pp} \rightarrow \overline{p}X$ reaction. The NAR process is particularly efficient for antiprotons and its effect is to flatten out their spectrum at low energy as visible in figure 1.4(a) for the corresponding $\overline{p}$ flux. So the low energy tail of the $\overline{p}$ spectrum is repopulated by higher energy $\overline{p}$. In the same direction the effect of solar modulation acts shifting the spectrum toward lower energies. As a result, the secondary $\overline{p}$ is more abundant at low energy than previously thought, while some collected antiproton data are reported in figure 1.4(b) where also some theorethical predictions are plotted.

1.2 Observational evidences for Dark Matter

The first claims of experimental evidence of Dark Matter, formely called missing matter, came from pioneering work of J. Oort in 1932 and F. Zwicky in 1933. F. Zwicky, measuring the radial velocities of eight galaxies in the Coma cluster, observed an unexpected large velocity dispersion and he concluded that ~ 10 times more mass than luminous mass was needed to explain them [15]. So far a large set of experimental observations from galactic scales up to extragalactic ones converged to prove that non visible gravitating matter, so called Dark Matter (DM), is missing.

The most robust evidence for DM comes at galactic scales from the rotation curves of spiral galaxies, first studied by J. Oort in 1932[17], during the seventies were intensively measured over large distances[18, 19]. Mostly the profile of orbital velocity versus the distance from the galactic center was found to be constant (independent of radius) or

slightly rising, as shown in figure 1.5. According to Newtonian machanics, balancing centrifugal and gravitational forces, the measured profile obliges to assume that the main part of matter in galaxies is non shining and extends for a much bigger region than luminous one. From the study of these curves an estimation of the energy density Ω_{lum} (stars and gas) and Ω_{halo} (DM) could be inferred:

$$\Omega_{\text{lum}} \leq 0.01 \ ,$$
$$\Omega_{\text{halo}} \geq 0.1 \ .$$

The cosmological density Ω of a given species is quoted as:

$$\Omega = \frac{\rho}{\rho_{\text{crit}}} \ , \tag{1.5}$$

where ρ is the density of the species under study and $\rho_{crit} = 3H_0^2/8\pi G = 1.88h_0^2 \times 10^{-29}$ gcm^{-3} is the critical density, H_0 is the Hubble constant ($H_0 = 100h$ km^{2}s^{-1}Mpc^{-1}) and G is the gravitational constant. Moving to a larger scale, evidence for DM is confirmed by modern measurements on Clusters of galaxies coming from optical observations of galaxy dynamics, X-rays temperature of hot cluster gas and gravitational lensing (distortion of background images by foreground matter). If we consider the clusters of galaxies as a representative sample of the whole Universe, it is possible to infer an estimation of the matter density Ω_M:

$$\Omega_{\text{M}} \sim 0.2 - 0.3 \ . \tag{1.6}$$

The most accurate results on the Dark matter content of the Universe come from measurements at cosmological scales. Recent Cosmic MicroWave Background (CMB) measurements from WMAP [20], combined with other cosmological measurements, such as the galaxy power spectrum, sharply constrain cosmological parameters. Actually, as shown by COBE and confirmed by WMAP on the largest scales the distribution of galaxies is close to be uniform or isotropic. As we move to smaller scales, we see a rich structure that is not random but can be related to the primordial quantum fluctuations. The anisotropies of CMB are therefore strictly correlated to initial perturbation and to the geometry of the Universe. The CMB picture resulting from WMAP in the temperature range of ± 200 μKelvin is shown in figure 1.6[1]. The current estimation from WMAP combined with Sloan Digital Sky Survey (SDSS) gives the following value for the matter contribution to the total energy density of the Universe [21]:

$$\Omega_{\text{M}} = 0.24 \pm 0.02 \ , \tag{1.7}$$
$$\Omega_{\text{tot}} = 1.003 \pm 0.010 \ . \tag{1.8}$$

---

[1]Credit:NASA/WMAP Science Team
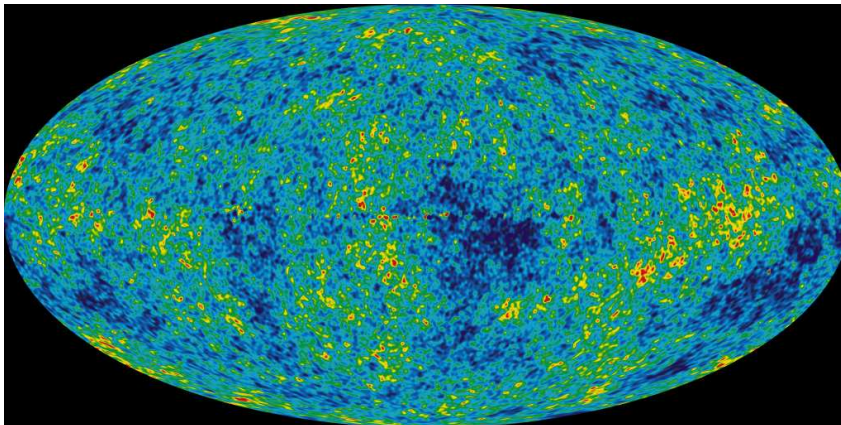
Figure 1.6: All-sky picture of the CMB in the temperature range of ± 200 μKelvin from three years of WMAP data. The signal from our Galaxy is subtracted.

1.3 Dark Matter Candidates

1.3.1 Baryonic DM

The simplest possibility to take into account is to suppose that Dark Matter is due to barionic objects which do not shine. Non *luminous* baryon matter could be constituted by low mass object as brown dwarfs ($0.08 M\odot$) and Jupiters ($0.001 M\odot$), or the results of stellar evolution like neutron stars, black holes and white dwarfs. These baryonic candidates are called MACHOs (Massive Compact Halo Objects) and can be detected in our galaxy, for example, through microlensing observations. This density is comparable to the one required by big-bang nucleosynthesis (BBN).

However an important ingredient in the motivation for non-baryonic dark matter comes from BBN limits on the average baryonic content of the Universe. The successful predictions of the relative ratios of deuterium, ^3He, ^4He, ^7Li from BBN provide strong limits on the value of Baryon density $\Omega_B = \rho_B/\rho_{\mathrm{crit}}$ [2]:

$$\Omega_B = 0.0223^{+0.0007}_{-0.0009}\ h^{-2} \quad \text{with} \quad h = 0.73^{+0.03}_{-0.04}\ . \tag{1.9}$$

Several independent estimates of the matter density in the universe point to a value one order of magnitude larger than the maximal value provided by baryons alone according to nucleosynthesis. The need for non-baryonic dark matter is therefore striking.

1.3.2 Non baryonic DM: WIMPS

As concluded in the previous section, the major part of Dark Matter is required to be non-baryonic. In large scale structure formation not only Ω_{M} is important, but also the type of particle that makes it up. To take into account the different effects of possible

candidate in structure formation, non-barionic DM is divided into two classes: Cold Dark Matter (CDM) and Hot Dark Matter (HDM).

If the particle is very light like massive but light neutrino, it will be relativistic at the time of its decupling from the thermal bath, when its rate of interaction became smaller than the expansion rate and it froze out. So at the time the structure starts to form they will free-stream out of galaxy-sized overdense regions and only very large structures can form early. Such type of particles are called hot dark matter, and the Universe structure forms according to a typical top-down scenario by the fragmentation of large structures into smaller ones. This behaviour is nowadays strongly discouraged in view of observations of the distribution of galaxies at very high redshift, but a hot dark matter component at around 10% level cannot be excluded [22].

Massive particles which were non-relativistic when decoupled form cold dark matter. In this case the large scale structure is generated in a hierarchical fashion, with small clumps merging in larger ones, forming galaxy halos and successively larger structures. In between hot and cold dark matter there may exist Warm Dark Matter (WDM), which could be made up of keV scale neutral particles (like the supersymmetric partner of the graviton, the gravitino). Warm dark matter is not particularly favoured at the moment, both for particle physics and structure formation reasons, but the possibility should be considered.

In addition, since these Dark Matter particles would be relics from the Big Bang, they should be stable particles whose relic densities match observations. At first-order, the contribution to Ω_M from a massive particle X depends only on its annihilation cross section σ_X and not explicitly on its mass. The resulting Ω_X is:

$$\Omega_X h^2 \sim \frac{3 \times 10^{-27} \text{cm}^3 \text{s}^{-1}}{\langle \sigma_A v \rangle} \ . \tag{1.10}$$

An interesting consequence of equation (1.10) is that massive particles which have interactions of the order of the weak interaction naturally give the correct contribution to Ω_M. The generic name for such a dark matter candidate is WIMP (Weakly Interacting Massive Particle), which contains no electrical charge, no dipole momentum, no strong force color charge and which can only interact via weak or gravitational force. Among WIMPs belong Kaluza-Klein particles, heavy 4th generation neutrinos and lightest supersymmetric particles (LSP) arising from different SUSY models. Another well motivated candidate is the axion, which is a hypothetical particle predicted from QCD symmetry breaking whose existence would ensure that the strong interactions conserve P and CP. Among the particle candidates for CDM the favorite one is presently the Lightest Supersymmetric Particle (LSP), and in particular neutralino, which is discussed in the following section.

1.3.3 MSSM and the neutralino

No candidates for such non-barionic relics of the Early universe are present in the Standard Model of particle physics (SM), but they can be found for example in its SuperSymmetric extension [23].

One of the strongest motivation to go beyond the Standard Model (SM) is the lack of protection of scalar masses in the SM. In order to avoid scalar masses to getting too large value, a new symmetry, called SuperSymmetry (SUSY), is introduced and it is unbroken down to the weak scale. To prevent proton decay, otherwise predicted from the theory, an additional discrete symmetry, called R matter parity, is imposed. For a particle of spin s, lepton number L and barion number B, R parity is defined as:

$$R = (-1)^{3(B-L)+2s} \ . \tag{1.11}$$

R is a multiplicative quantum number equal to -1 over the SUSY particles and equal to $+1$ over the ordinary particles. This means that supersymmetric particles can only be created or annihilated in pairs in reactions of ordinary particles. It also means that a single supersymmetric particle can only decay into final states containing an odd number of supersymmetric particles. In particular, this makes the lightest supersymmetric particle stable, since there is no kinematically allowed state with negative R-parity to which it can decay. As claimed previously, to be a good dark matter candidate, a particle has to be weakly interacting and stable, so in these models with R parity conservation, the lightest SUSY particle (LSP) is a good particle candidate for CDM.

Extending the SM in the minimal way, adding for each SM particle only one supersymmetric partner with the same quantum numbers, we obtain the Minimal extension of Super Symmetry Model (MSSM) [24]. The only addition to this doubling of the particle spectrum of the Standard Model concerns the Higgs sector, where two Higgs doublets H_1 and H_2 are required in order to give mass both to down and up quarks and to cancel anomalies. After electroweak symmetry breaking, the physical Higgs fields consist of two charged particles and three neutral ones: two scalar fields (h and H) and one pseudoscalar (A). The ratio of the two vacuum expectation values VEVs of the physical Higgs is:

$$\tan \beta = \langle H_2 \rangle / \langle H_1 \rangle \ , \tag{1.12}$$

which always enters as a free parameter in the MSSM. The supersymmetric sector of the model introduces some other free parameters: the mass parameters M_1, M_2 and M_3 for the supersymmetric partners of gauge fields (gauginos), the Higg mixing parameter μ and, in general, all the masses of the scalar partners of the fermions (sfermions) and all the trilinear couplings which enter in the superpotential.

The most general version of the MSSM, despite its minimality in particles and interactions, contains well over a hundred new parameters. In order to deal with manageable models, it is necessary to introduce some reasonable assumptions, which establish relations among the too many free parameters at the electroweak scale. Usually all the squarks

and slepton mass parameters are taken as degenerate to a common value $m_{\tilde{l}_i} = m_{\tilde{q}_i} = m_0$ and that all the trilinear couplings are vanishing except those of the third family which are unified to a common value A. In addition the gaugino masses are generally assumed to unify at M_{GUT} scale [25], and this implies that the U(1) and SU(2) gaugino masses are related at the electroweak scale by:

$$M_1 = (5/3) \, tan^2\beta \, M_2 \; . \tag{1.13}$$

In summary when all these conditions are imposed, the supersymmetric parameter space is completely described by six independent parameters: M_2, μ, $\tan\beta$, m_A, m_0 and A.

The neutralinos are four mass eigenstates defined as linear superpositions of the two neutral gauginos (fotino $\tilde{\gamma}$ and zino $\tilde{Z}$) and the two neutral higgsinos ($\tilde{H}_1$ and $\tilde{H}_2$):

$$\chi = a_1\tilde{\gamma} + a_2\tilde{Z} + a_3\tilde{H}_1 + a_4\tilde{H}_2 \; . \tag{1.14}$$

The lowest mass eigenstate plays the role of the lightest supersymmetric particle in the MSSM, and may then constitute the dark matter candidate in this model. It will be called the neutralino and its mass denoted by m_χ. To classify the nature of the neutralino it is useful to define the parameter P:

$$P = a_1^2 + a_2^2 \; .$$

The neutralino is called a *gaugino*, when $P > 0.9$, a *higgsino* when $P < 0.1$ and mixed when $0.1 \leq P \leq 0.9$. The corresponding phenomenology is drastically different leading to different predictions for CDM.

Neutralinos are expected to decouple from the hot plasma in the early Universe, when they are not relativistic. Their relic abundance can be determined:

$$\Omega_\chi h^2 = C \frac{g_*^{1/2}(T_{\mathrm{f}})}{g_{*s}(T_{\mathrm{f}})} \frac{1}{\langle \sigma_{\mathrm{ann}} v_{\mathrm{r}} \rangle_{\mathrm{int}}} \; , \tag{1.15}$$

where $C = 8.7 \times 10^{-11} \mathrm{GeV}^{-2}$ and $g_*(T_{\mathrm{f}})$ and $g_{*S}(T_{\mathrm{f}})$ denote the effective number of degrees of freedom for the energy density and for the entropy density, respectively, evaluated at the freeze-out temperature T_{f}; $\langle \sigma_{\mathrm{ann}} v_{\mathrm{r}} \rangle_{\mathrm{int}}$ is the neutralino pair annihilation times the pair relative velocity, averaged over the neutralino thermal density distribution, integrated from the freeze-out temperature down to the present temperature. The critical quantity to be evaluated is the neutralino annihilation cross section, which, depending on the neutralino mass, can get contributions from all the different final states.

1.4 Dark Matter detection

There are two basic ways to detect WIMP (Weakly Interacting Massive Particles) dark matter which is present in the halo of our Galaxy. The first method is direct detection

of these particles, by observation of nuclear recoil after WIMP-nucleus elastic scattering. The second method, indirect detection, exploits the possibility to detect products of the annihilation of DM particles, either in the galactic halo or in celestial bodies (namely the Earth and the Sun), where WIMPs may have been accumulated by gravitational capture. In the latter case, the signal consists of a flux of neutrinos emitted from the central regions of the body, and what is typically observed is a flux of upgoing muons produced by the charged current conversion of the muon neutrino component of the signal. In case of DM annihilation in the galactic halo, there are more possibilities: the signal may consist of gamma rays, neutrinos and antimatter (positrons, antiprotons and antideuterons).

1.4.1 Direct detection

From the particle physics point of view, direct detection relies on the scattering cross section of the WIMP with a nucleon of the detector nuclei. Qualitatively, the expected scattering rate is given by:

$$R = \frac{\rho}{M_\chi} \langle \sigma \ v \rangle \ , \qquad (1.16)$$

where ρ is the WIMP density near Earth, M_χ is the WIMP mass, σ is the elastic-scattering cross section and v is the average speed of the WIMP relative to the target. Considering the local density of DM roughly equal to 0.3 GeV/cm^3 and a typical mean WIMP velocity of 220 km/s [2], the interaction rate mainly depends on unknown WIMP mass and cross section. The latter depends on the nature of the couplings, that for neutralino WIMPs can be either spin-dependent or spin-independent. So in the first case targets with high mass nucleus from Ge to Xe are used, while in the second case nuclei of ^{19}Fe and ^{127}I are preferred for the search. However, the expected very low cross section of WIMPS on ordinary material makes these interactions quite rare. The more massive the WIMP, the more the energy deposited, but also the smaller the event rate. The low count rate requires that the experiments have extremely good background discrimination, very large detectors, and/or very long counting times.

Experimental results have reported a positive indication of a signal in terms of the annual modulation of the rate due to the Earth motion relative to the WIMP wind: in particular DAMA Collaboration (using NaI target) claimed to have detected a temporal modulation with the expected amplitude, phase and period. When interpreted as due to dark matter scattering, the allowed region for the scattering cross section versus the WIMP mass, is not compatible with the results of other experiments like CDMS ans EDELWEISS.

1.4.2 Indirect detection

Though WIMPs must be stable, nothing prevents them from annihilating with their antiparticle; indirect searches look for the annihilation products in the CR in order to detect

an excess with respect to the abundance predicted by known production processes. Neutralinos may annihilate into quark-antiquark pairs, into gauge bosons, into a Higgs boson pair and into a Higgs and a gauge boson. These in turn decay or hadronise leading to final states containing also ν, e^+, $\overline{p}$, γ and antinuclei. This indirect method is complementary to the direct one and it is becoming very promising thanks to powerful new detectors for cosmic gamma rays and neutrinos planned and under construction. Also several balloon-borne experiments and space experiments like PAMELA and more ambitious AMS-02 are under way. Unfortunately, since there are many other possibilities to create these antiparticles by astrophysical sources the interpretation is not always univoque.

Gamma rays may also result from loop-induced annihilations $\chi\chi \rightarrow \gamma\gamma$ and $\chi\chi \rightarrow Z\gamma$ giving mono-energetic photons $E_\gamma = m_\chi$ or $E_\gamma = m_\chi(1 - m_Z^2/4m_\chi^2)$ from the halo [22]. The rates of these processes are difficult to estimate because of uncertainties in the supersymmetric parameters, cross sections and halo density profile. A signature may be found in the continuum γ-ray spectrum in the form of a smooth bump at about one tenth of the neutralino mass. In this case experiments like AMS and GLAST satellite or air Cerenkov telescopes, that will explore a quite complementary energy range, would have good chances to detect this kind of signal. However, another possibility to detect dark matter in gamma-rays has recently been investigated. In practice the monochromatic spectral lines are expected to suffer a smearing due to red-shift. The signature would be a continuum from neutralino annihilations plus a characteristic redshift-smeared line with a very rapid fall-off beyond the energy corresponding to the neutralino mass. These measurements will give also the position of the source, being γ rays not sensitive to intergalactic magnetic fields.

An additional component to the secondary positrons spectrum may result from the χ decay chains or hadronisations. The actual shape of the spectrum depends on the preferred decay mode of neutralino. A lot of uncertainties effect the estimation of the positron background due to astrophysical sources. The Dark Matter signal is therefore more promising at high energies where this background is relatively small and well understood.

For kinematical reasons, antiprotons created by pair-production in cosmic ray collisions with ISM are produced with relatively high energy, whereas antiprotons from neutralino annihilation are expected to populate mainly the low energy band. However, it was found recently, as pointed out in § 1.1.3, that the secondary antiprotons may populate also the low-energy region to a greater extent than previously thought, making the extraction of an eventual supersymmetric signal much more difficult. Indeed, both for positrons and for antiprotons the uncertainties on the galactic propagation model and solar wind modulation make difficult to disantangle the primary supersymmetric signal from the secondary production. A very rare process in proton-proton collisions is the antideuteron production, which seems to be less rare in neutralino annihilation. However, the fluxes are so small that the possibility of detection seems a challenging task even for a large acceptance and long exposure experiment like AMS-02. These last two neutralino indirect

search channels ($\overline{\text{p}}$ and $\overline{\text{d}}$) will be largely treated along this chapter.

1.5 Antideuterons as a signature for SUSY Dark Matter

Antimatter cosmic rays are also expected from neutralino annihilation in our galaxy and so a primary component is going to add up to the secondary distribution. For kinematic reasons the flux of secondaries drops off at low energy, where vice versa the supersymmetric antimatter production is favoured. So an excess of low energy antinuclei would signal the presence of an exotic source. However, for antiprotons, it has been recently realized [26, 27, 28], as discussed in § 1.1.3, that the secondary spectrum is much flatter at low energy than previously estimated. This fact motivates antideuteron search, which does not experience such a problem.

1.5.1 Supersymmetric source term

If there are neutralinos in our galaxy, the source term for SUSY antideuterons production is defined as:

$$q_{\overline{\text{d}}}^{\text{SUSY}}(\chi + \chi \rightarrow \overline{\text{d}} + ...) = \langle \sigma_{\text{ann}} v \rangle \, \frac{\text{d}N_{\overline{\text{d}}}}{\text{d}E_{\overline{\text{d}}}} \left\{ \frac{\rho_\chi}{m_\chi} \right\}^2 \, , \tag{1.17}$$

where $\langle \sigma_{ann} v \rangle$ is the mean value over the distribution of the galactic velocity of the neutralino pair annihilation cross section σ_{ann} multiplied by the relative velocity v; $\text{d}N_{\overline{\text{d}}}/\text{d}E_{\overline{\text{d}}}$ is the antideuteron differential multiplicity, that will be discussed in detail in the following section; m_χ is the neutralino mass and ρ_χ is the mass distribution function of neutralinos inside the galactic halo.

Assuming that relic neutralinos behave as cold DM, this population is supposed to follow the dark matter density profile of the galactic halo:

$$\rho_\chi(r, z) = \xi \rho_{DM}(r, z) \, , \tag{1.18}$$

where ξ is a parameter ≤ 1 to consider the fact that relic neutralinos may not be responsible for the total amount of Dark Matter in the universe. This situation occours in many supersymmetric models.

For the Dark Matter density distribution can be assumed a spherical isothermal profile, which is a function of the radial distance r in the galactic plane and of the vertical coordinate z:

$$\rho_{DM}(r, z) = \rho_\chi^\odot \frac{R_c^2 + R_\odot^2}{R_c^2 + r^2 + z^2} \, , \tag{1.19}$$

where $R_\odot$ is the distance of the Sun from the galactic center, R_c is the core radius of the DM halo and $\rho_\chi^\odot$ is its density in the solar neighborhood. These parameters are

known with some uncertanties and they can be set to $R_c = 3.5$ kpc, $R_\odot = 8.5$ kpc and $\rho_\chi^\odot = 0.4$ GeV cm^{-3} as considered by some authors [28]. In particular a value of the local density, compatible with experimental observations from rotational velocities, may lay in the range $0.18 < \rho_\chi^\odot < 0.71$ GeV cm^{-3}. The source term $q_{\overline{d}}^{susy}$ is a combination of astrophysical factors, like the latter dark matter density profile, and particle physics issue, like neutralino self annihilation cross section, which depend on the properties of supersimmetric model. It is important to observe that, since the antideuteron primary flux depends on the square of neutralino density, it is particularly sensitive to this parameter and so the existing loose constraints on $\rho_\chi^\odot$ value imply strong variations in the calculations of the expected antideuteron flux. The presence of clumpiness in the DM distribution would also significantly increase this signal.

A key difference as regards the production mechanisms concerning standard astrophysical sources, lies in the fact that this new source is not confined to the galactic disc.

1.5.2 Antideuteron production

The computation of the $\overline{d}$ differential multiplicity induced by neutralino pair annihilations involves both factorization scheme and coalescence model and may be expressed as [29]:

$$\frac{dN_{\overline{d}}}{dE_{\overline{d}}} = \left(\frac{4P_{coal}^3}{3k_{\overline{d}}}\right) \left(\frac{m_{\overline{d}}}{m_{\overline{p}}m_{\overline{n}}}\right) \sum_{F,h} B_{\chi^h}^{(F)} \left\{\frac{dN_{\overline{p}}^h}{dE_{\overline{p}}}(E_{\overline{p}} = E_{\overline{d}}/2)\right\}^2 , \qquad (1.20)$$

where $E_{\overline{d}}^2 = m_{\overline{d}}^2 + k_{\overline{d}}^2$ and with two important assuptions: first, that the probability of producing a pair of antinucleons $\overline{p}$ and $\overline{n}$ is given by the product of the probability of producing a single antinucleon (*factorization*); second, that the $\overline{n}$ production cross section is equal to the $\overline{p}$ production cross section thanks to the isospin invariance. The hypotesis of factorization is certainly conservative. In the last term of equation (1.20) the differential multiplicity for antiprotons (or antineutrons) is written as:

$$\frac{dN_{\overline{p}}}{dE_{\overline{p}}} = \frac{dN_{\overline{n}}}{dE_{\overline{n}}} = \sum_{F,h} B_{\chi^h}^{(F)} \frac{dN_{\overline{p}}^h}{dE_{\overline{p}}} , \qquad (1.21)$$

where the annihilation is considered to proceed trough the various final states F towards the quark or the gluon h-state with the branching ratio $B_{\chi^h}^{(F)}$. Quarks and gluons are directly produced when a neutralino pair annihilates and consequently generate jets whose fragmentation and hadronization yeld the antiproton energy spectrum $dN_{\overline{p}}^h/dE_{\overline{p}}$. The hadronization is computed through Monte Carlo simulations.

The physical phenomenon which plays a key role in making the antideuteron flux at low energy a promising signature for the presence of neutralino Dark Matter is the fusion process. The coalescence function $C(\vec{k}_{\overline{p}} - \vec{k}_{\overline{n}})$, which describes the probability to form by fusion an $\overline{d}$ from a $\overline{p}$–$\overline{n}$ pair as a function of the difference of their initial momenta,

(a)   (b)
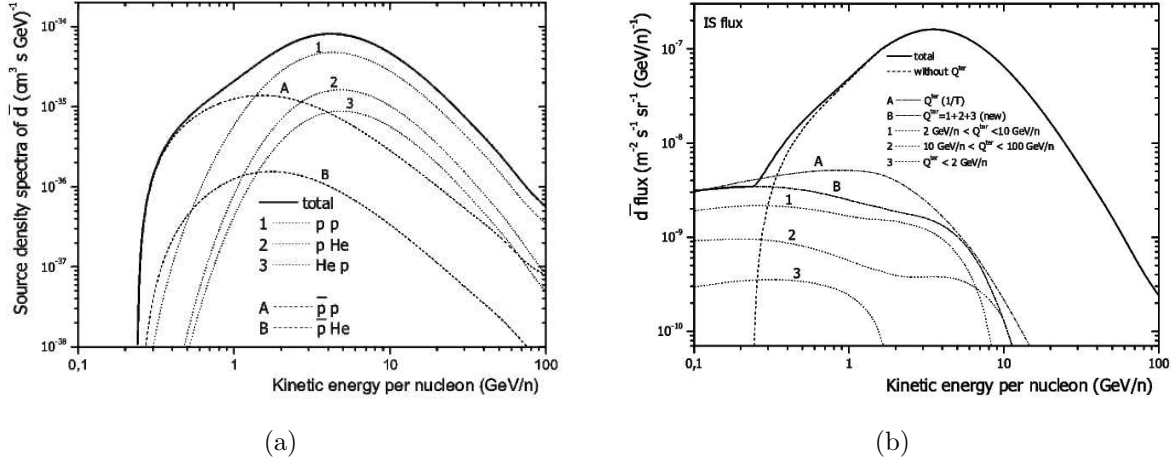
Figure 1.7: a) Source density spectra for antideuterons considering the different spallation process included in Q^{sec} as explained in the text [14]. b) The effect of the tertiary component on $\overline{\mathrm{d}}$ flux decomposed into individuals contributions [14].

is strongly peaked around $C(\vec{k}_{\overline{\mathrm{p}}} - \vec{k}_{\overline{\mathrm{n}}}) = 0$. The main hypothesis introduced in the coalescence model is that the two antinucleons merge togheter to form an antideuteron, if the difference of their momenta is less than a critical value, namely the coalescence momentum P_{coal}. A value of $P_{\mathrm{coal}} = 58$ MeV has been derived [30], not so far from the $\overline{\mathrm{d}}$ binding energy $\sqrt{m_{\mathrm{p}}\, B} \approx 46$.

Dark Matter neutralinos may be considered almost at rest in the galactic frame since their average velocity is of the order of 300 kms^{-1}. So in neutralino annihilation antinucleons are mainly produced at low energies, where the fusion process which produces antideuterons is more probable.

1.5.3   Galactic astrophysical source

Antideuterons are expected to be produced from standard astrophysical sources similarly to antiprotons, but with some crucial differences [14].

In order to make an accurate calculation of the $\overline{\mathrm{d}}$ flux, not only the pA $\rightarrow \overline{\mathrm{d}}X$ process, but also the competing reaction $\overline{\mathrm{p}}$A $\rightarrow \overline{\mathrm{d}}X$ gives a relevant contribution to be taken into account, although the antiproton flux is very much lower than the proton one. Actually, the computation of the differential cross section for pp $\rightarrow \overline{\mathrm{d}}X$ and $\overline{\mathrm{p}}$p $\rightarrow \overline{\mathrm{d}}X$ reactions, using the coalescence model described above, gives as result a cross section for the latter reaction four order of magnitude larger than for the former one. In addition, the distributions of the corresponding fluxes are very different: the $\overline{\mathrm{p}}$p $\rightarrow \overline{\mathrm{p}}$p($\overline{\mathrm{n}}$n) reaction is centered at much lower energies than the pp $\rightarrow$ pp($\overline{\mathrm{p}}$p)($\overline{\mathrm{n}}$n) as can be seen in figure 1.7(a).

The source terms $Q^{\mathrm{sec}}(T_{\overline{\mathrm{d}}})$ and $Q^{\mathrm{ter}}(T_{\overline{\mathrm{d}}})$ presented for antiprotons, respectively in equa-

tion 1.3 and 1.4 of § 1.1.3, can be adapted to be valid for antideuterons just changing label $\overline{p}$ with $\overline{d}$. In the secondary source term only p–p, p–He and He–p incoming channels are taken into account, while heavier components are neglected. The contribution to the flux coming from these collisions, shown in figure 1.7(a), is peaked around 4 GeV/n, above the $\overline{d}$ production threshold and where the $\overline{d}$ cross section is large, whereas the decreasing at higher energies is due to the power low distribution of the primary proton flux. Therefore for kinematical reasons, a spallation reaction creates very few low energy particles and over the entire low energy range below 1.5 GeV/n the dominant contribution to the IS galactic $\overline{d}$ flux is given from the $\overline{p}p \rightarrow \overline{d}X$ reaction. At energies above 2 GeV this contribution becomes negligible.

In the tertiary source term the effect of non-annihilating inelastic scattering of secondaries on the ISM (NAR process) are considered. This redistribution mechanism has significant different effects on the shape and intensities of $\overline{p}$ and $\overline{d}$ flux, simply because the NAR cross section is much smaller for $\overline{d}$s than for $\overline{p}$s. It is clear in figure 1.7(b) that the tertiary contribution is negligible for antideuterons; this fact explains the rapid drop in the $\overline{d}$ secondary spectrum, quite different from what happens in the $\overline{p}$ case, as illustated in § 1.1.3.

So, low energy secondary antideuterons are suppressed and energy loss mechanisms are less efficient in shifting the antideuteron energy spectrum towards low energies.

1.5.4   Antideuteron flux

To derive the antideuteron SUSY flux, the Minimal Supersymmetric extension of the Standard Model (MSSM), described in § 1.3.3, is used as a theoretical framework. In the work we are refering to [29], the free parameters of the theory span in the following ranges:

$$20 \text{ GeV} \leq M_2 \leq 500 \text{ GeV}, \qquad 20 \text{ GeV} \leq |\mu| \leq 500 \text{ GeV},$$
$$80 \text{ GeV} \leq m_A \leq 1000 \text{ GeV}, \qquad 100 \text{ GeV} \leq m_0 \leq 1000 \text{ GeV},$$
$$-3 \leq A \leq +3, \qquad 1 \leq \tan\beta \leq 50 , \tag{1.22}$$

according to the constraints coming from all the experimental limits achieved at accelerators and in particle physics. It is further required a supersymmetric configuration to provide a neutralino relic abundance in accordance with the cosmological bound $\Omega_\chi h^2 \leq 0.7$ [2].

Neutralinos are Majorana fermions and will annihilate each other in the halo producing leptons, quarks, gluons, gauge bosons and Higgs bosons. These products can decay or form jets which hadronize giving rise to standard particles like antiprotons. For the evaluation of the averaged annihilation cross section $\langle \sigma_{ann} v \rangle$, all the tree-level diagrams which are responsible for neutralino annihilation and which are relevant to $\overline{p}$ production have to be considered: $q\overline{q}$, $l\overline{l}$, W^+W^-, Z^0Z^0, W^+H^-, Z^0H_1, Z^0H_2, H_1H_3 and H_2H_3. For
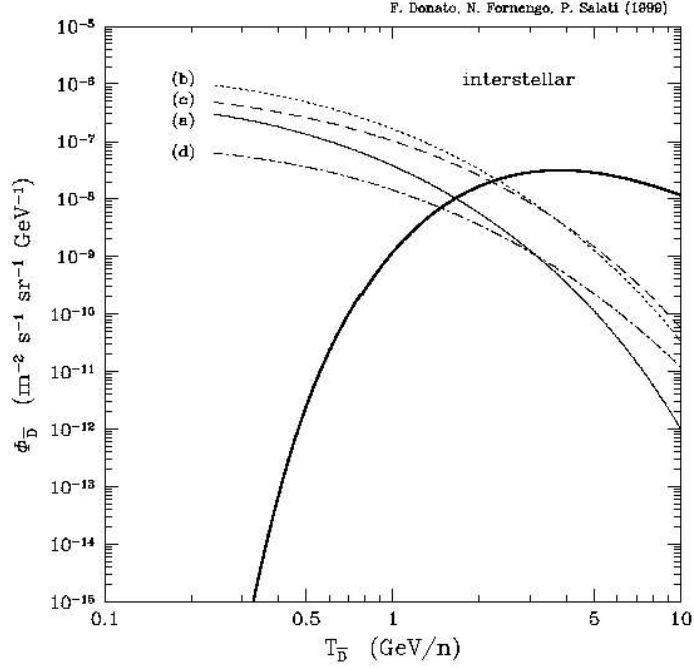
Figure 1.8: The predicted antideuteron primary flux is plotted according to four different points in the SUSY parameter space. In particlular in case (c), dashed line, the neutralino is a gaugino-higgsino mixture; while in case (a), dotted line, it is a pure gaugino [29].

each final state all the relevant Feynman diagrams are considered [27]. The $\overline{p}$ differential distribution $dN_{\overline{p}}/dE_{\overline{p}}$ has been evaluated as discussed in § 1.5.2, where the branching ratios B has to be computed using the Monte Carlo code for all annihilation final states F which may produce $\overline{p}$. The effect of propagation on primary antideuterons from remote regions of the galactic halo to the Earth has been treated as referred in [28] for antiprotons. The resulting energy spectra for the supersymmetric antideuterons component is shown in figure 1.8. In this figure four supersymmetric examples are respectively featured by the solid (a), dotted (b), dashed (c) and dot-dashed (d) curves, as obtained spanning the supersymmetric parameter space. The primary fluxes flatten at low energy where they reach a maximum, because $\overline{d}$ production from neutralino annihilation is favoured. Actually, the annihilation takes place at rest in the galactic frame making more probable the coalescence of primary $\overline{d}$ at low energy. The supersymmetric signal is the largest below 1 GeV, where the secondary antideuteron *background* (heavier solid line) vanishes.

The secondary $\overline{d}$ flux, more recently estimated by [14], is presented in figure 1.9(a). The $\overline{d}$ spectrum drops sharply at low energies depleting the low energy region below 1 GeV where the primary species are mostly produced, as shown in figure 1.8. Even when the effect of modulation is considered, as shown in figure 1.9(b), at low energies the $\overline{d}$

(a)   (b)
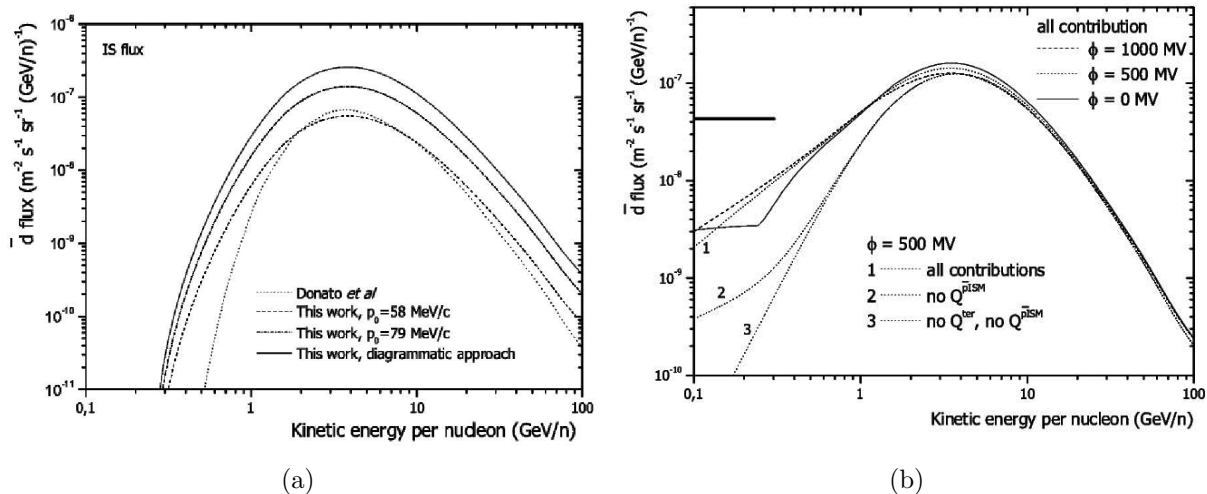
Figure 1.9: a) The present results on secondary $\overline{\mathrm{d}}$ spectrum are presented: three curves obtained for the different parameterization considered in Ref. [14] are compared to the spectrum previously estimated in [29], reported in figure 1.8. b) The effect of solar modulation is taken into account. The curves labelled 1,2,3 gives the contribution of new source terms explained in § 1.5.3 [14].

supersymmetric flux is significantly above the secondary one.

Antideuterons appear therefore as a much cleaner probe of the presence of supersymmetric relics in the galactic halo than antiprotons. The price to pay however is a much smaller flux. Actually a typical primary spectra may reach up to 10^{-6} m^{-2}s^{-1}sr^{-1}GeV^{-1}, which is four orders of magnitude fainter than the $\overline{\mathrm{p}}$ one.

It is finally important to remark that present predictions of the primary component of the antideuteron flux, like that of the antiproton, are affected by a large uncertanty, mainly related to the fact that the source of primary fluxes is located inside the diffusive halo, whose size is unknown. The predicted flux may be much larger than the reference flux in [29] and new work is in preparation [2].

The importance of this physics channel is also confirmed by the development of a new dedicated experiment, the Gaseus Antiparticle Spectrometer (GASP) [31], which will explore many supersymmetric configurations. To conclude, since antideuteron signal is so rare and suppressed with respect to the others cosmic rays components like protons but also antiprotons, a very large acceptance spectrometer in space, with long exposure time and good particle identification, is required. This task is particularly challenging also for an experiment like AMS-02, whose detection power and sensitivity to this signal are explored in this thesis.

---

[2]F. Donato, private communications

Chapter 2

The AMS-02 experiment

The *Alpha Magnetic Spectrometer* (AMS) is a particle spectrometer designed to operate in space for the measurement of the properties of Cosmic Rays. It will be installed on the International Space Station (ISS), as shown in picture 2.1, to collect data for at least three years on low Earth orbit at about 400 km in altitude.

The successful precursor, AMS-01, was boarded on the space Shuttle discovery (NASA, STS-91 flight) for ten days in June 1998. The detector had been operational for about 180 hours collecting more than one hundred million cosmic ray events which led to significant results [32, 33, 34, 35, 36]

The AMS-02 design has been improved in order to fulfil the requirements of large acceptance (0.5 m^{2}sr), wide energy range, very long exposure time and excellent particle identification. These qualities make AMS-02 unique in the search for cosmic antimatter nuclei, dark matter indirect signatures and in refining the current CRs knowledge.

With AMS-02 high statistic accurate measurement of cosmic rays spectra, as well as their relative abundance and isotopic composition will be possible, which will be of crucial importance for our current knowledge of CR acceleration and propagation models.

In particular the secondary to primary ratio CR components (d/p, B/C, ^{3}He/^{4}He) are used to test the propagation models [13] and in figure 2.2(a) the B/C spectra expected for 6 months of data taking with AMS-02 it is shown as example. The ^{10}Be/^{9}Be is directly related to the CR confinement time in the galaxy and to the effective thickness of the galactic halo. These measurements are important also because CRs represent the background for the search for new physics signals.

In searching for primordial antimatter, AMS-02 should be able to collect approximately 2×10^9 He events in three years and thus lower the limit on $\overline{\text{He}}$/He of 3 order of magnitude with respect to the current one as shown in figure 2.2(b).

The annhilation of neutralino is expected to deviate the spectra of rare CR as $\overline{\text{p}}$, e^+, γ and $\overline{\text{d}}$. AMS-02 will allow to combine all indirect Dark Matter search channels, constraining the existing models.

AMS will contribute to the study of diffuse gamma background, both for galactic and
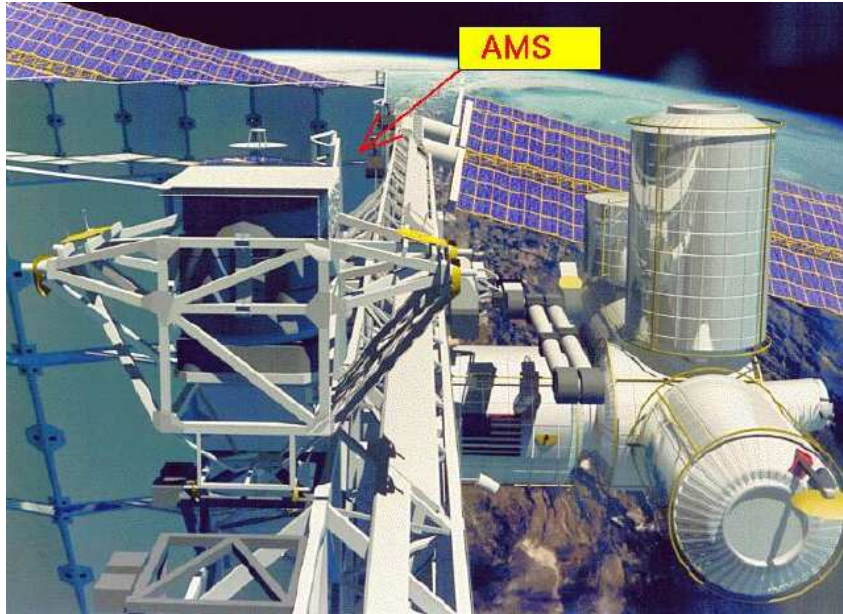
Figure 2.1: AMS-02 detector in the International Space Station (ISS).

extragalactic source location [38].

2.1 Detector overview

A particle with a given charge Z and rigidity R, moving through a region where a magnetic field exists, will have a trajectory depending only on the particle instantaneous rigidity and on the local magnetic field. In order to identify the incident particle, its rigidity is reconstructed from the measurement of the trajectory and it is related to particle mass as follows:

$$R = \frac{pc}{Ze} = \gamma\beta \, \frac{m_0 c^2}{Ze} \; , \tag{2.1}$$

where p is the relativistic momentum, m_0 is the particle rest mass, c is the speed of light in vacuum, $\beta = v/c$ and $\gamma = 1/\sqrt{(1 - \beta^2)}$. So to identify the incident particle is necessary to measure its trajectory (hence rigidity), velocity and charge.

Figure 2.3 shows a schematic view of all the AMS-02 sub-detectors, that are listed above, starting from the top to the bottom:

- A twenty layers Transition Radiation Detector (TRD) which will ensure a rejection factor electrons (or positrons) against hadrons of 10^3 to 10^2 in the energy range from 1.5 to 300 GeV;

- Four layers Time of Flight (TOF) hodoscope which provides primary trigger, measures time of flight ($\sim$ 120 picoseconds of resolution) and particle charge;

(a)   (b)
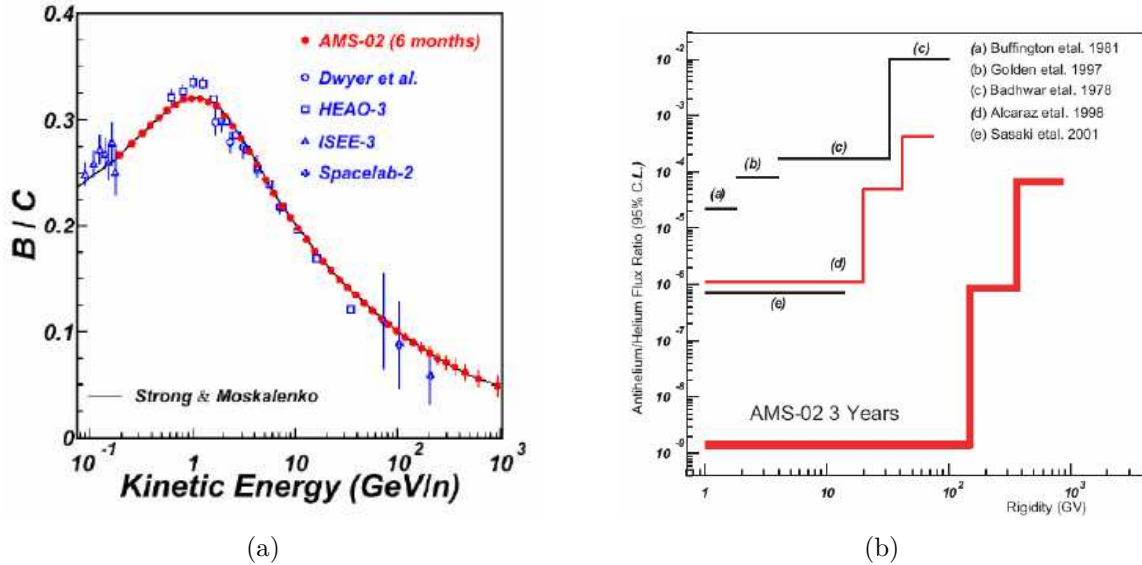
Figure 2.2: (a) Example of AMS-02 sensitivity for B/C ratio after 6 months of data taking compared to recent measurements and theoretical predictions [37].(b) Limit on $\overline{\text{He}}$/He ratio expected for AMS-02 after three years of data collection compared to previous measurements.

- The superconducting magnet which provides a bending power of $BL^2 = 0.86$ Tm^2.

- Eight layers of double sided silicon detectors, which provide particle rigidity and charge resolution of nuclei up to iron ($Z=26$).

- Veto, or Anti Coincidence counters (ACC) which ensure that only particles passing through the magnet aperture will be accepted.

- A Ring Imaging Cherenkov Counter (RICH), which measures the velocity (to 0.1%) and charge of particles or nuclei.

- A 3-D sampling calorimeter (ECAL) which measures the energy of gamma rays, electrons and positrons and distinguishes electrons and positrons from hadrons with a rejection of 10^4 in the range between 1.5 GeV to 1 TeV.

The design of AMS-02 sub-detectors has to meet a set of specific constraints imposed by launch and space conditions. All the detectors and related electronics are built with redundant philosophy. The main AMS-02 subsystems are examined in the following paraghraphs, except for Time Of Flight, which chapter 3 covers in detail.

AMS 02
(Alpha Magnetic Spectrometer)

TRD

TOF
(s1,s2)

Cryocooler

Vacuum
Case

Tracker

ACC

Magnet

He Vessel

TOF
(s3,s4)

RICH

ECAL

AMS on ISS for 3 years

R.Becker (MIT)
May 7, 2003
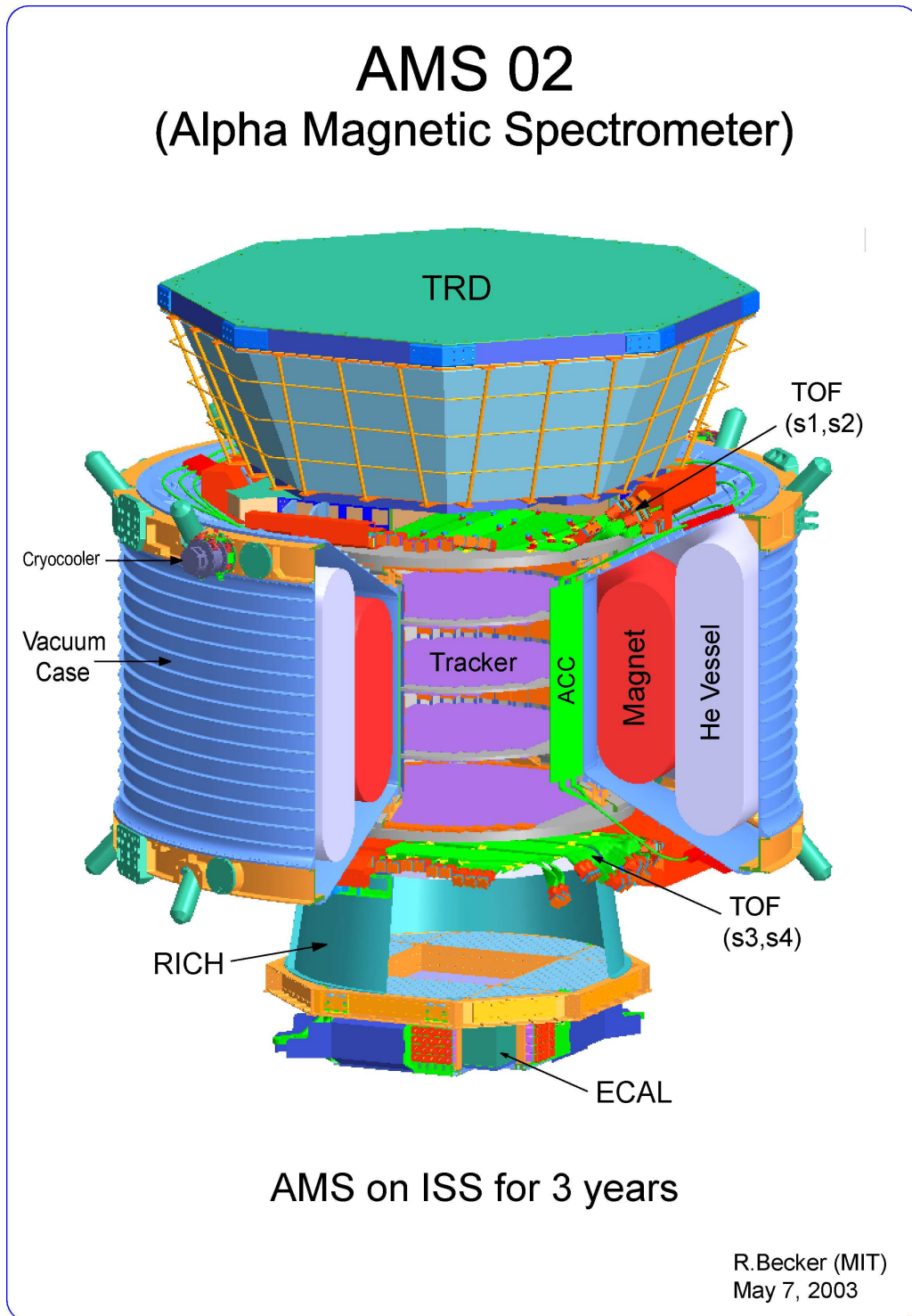
Figure 2.3: Schematic view of the AMS-02 detector where all the subdetectors are clearly visible.

(a) (b)
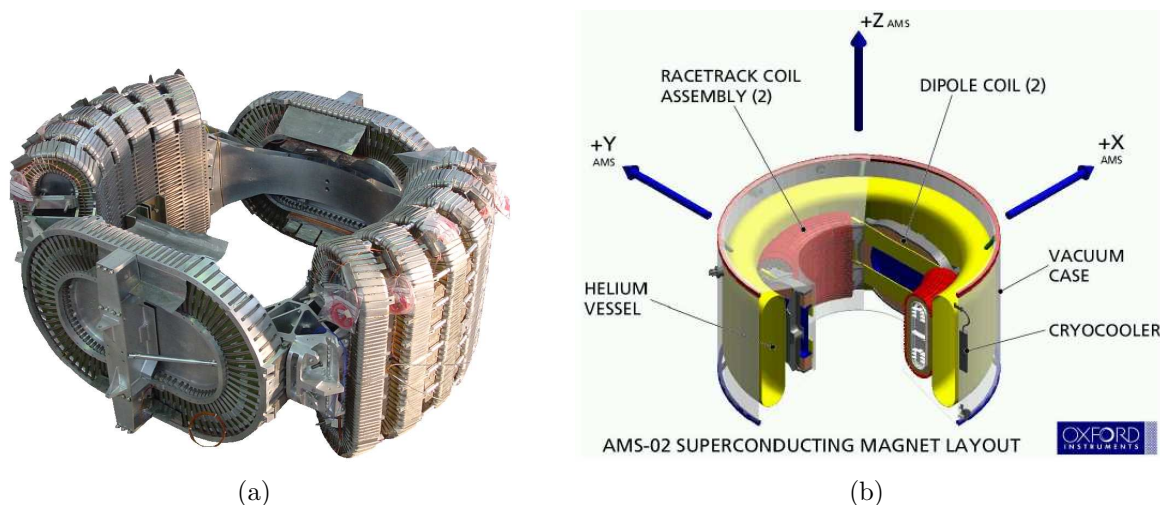
Figure 2.4: (a) The fully assembled superconducting magnet. (b) Layout of the magnet.

2.1.1   Superconducting magnet

The AMS-02 magnet will be the first large superconducting magnet to be used in space[39]. The design is therefore particularly challenging, especially for the cooling system required to keep the magnet operational and safe.

The AMS-02 magnet, shown in the two pictures of figure 2.4, consists of two dipole coils, which generate the majority of the transverse magnetic field, and two series of six smaller racetrack coils. The racetrack coils are included to minimize the magnitude of the field outside AMS and the coils arrangement is designed to give a high magnetic field inside and a very low field outside the experiment. In particular, it is necessary to minimize the magnetic dipole moment to avoid a torque in the ISS caused by the interaction with the Earth's magnetic field. The generated magnetic field is pointing in the x direction with a central value of 0.86 T and a dipole bending power of 0.78 Tm^2. In figure 2.5 the magnetic field expected by simulations inside and outside the magnet is illustrated.

All superconducting coils are situated around the inner cylinder of the vacuum tank and are cooled to a temperature of 1.8 K by a system of pipes, connected to a 2500 litre superfluid helium tank. The coils and helium vessel are enclosed in radiation shields and multi-layer superinsulation. The magnet will be launched at its proper operating temperature, with no current circulating in the coils. It will be charged only after the successful installation of the experiment on the ISS.

2.1.2   Silicon Tracker

The AMS-02 Tracker[40] consists of 8 layers of silicon detectors, to be arranged on the cylindrical support structure shown in figure 2.6(a). The Tracker detector provides an

(a)   (b)
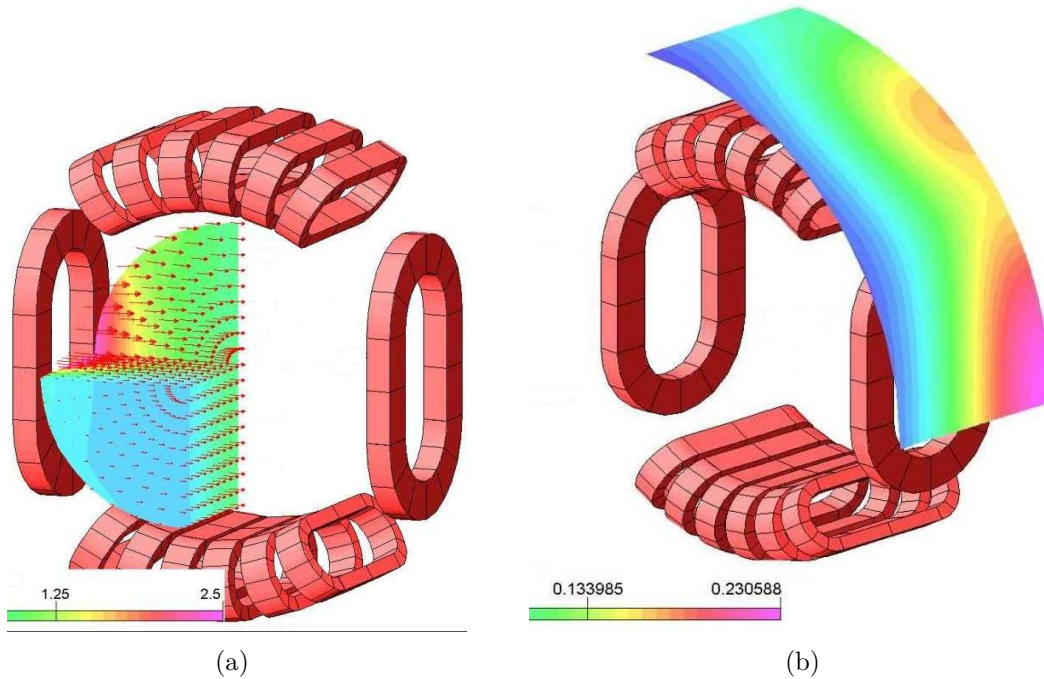
Figure 2.5: The magnetic field (in Tesla) expected inside (a) and outside (b) the AMS-02 magnet coils.

accurate measure of charged particles' trajectory along about 1 m inside the bore of the superconducting magnet. In addition to that, the measurement of the energy loss in the silicon wafers allows the charge of the traversing particle to be determined.

The Silicon Tracker consists of about 2500 sensors, which are electrically grouped together in ladders of 7 to 15 silicon sensors each one giving a total of 192 ladders. The silicon sensors are double sided to increase the trasparency of the Tracker, with p^+ and n^+ strip implantations running in orthogonal directions on the opposite face of the sensor, to provide the measurement of two coordinates. The junction side (or S–side) strips, which measure the bending coordinate, have an implantation pitch of 27.5 μm and a read out pitch of 110 μm. The ohmic side (or K–side) strips are implanted with a pitch of 52 μm, whereas the read out pitch is 208 μm. The S–side and K–side front-end electronics hybrids are mounted at one extremity. An electromagnetic interference shield in the form of a doubly metalized film surrounds each ladder. A fully equipped Tracker plane can be seen in figure 2.6(b).

Due to the large number on read-out channels, corresponding to ~ 3 Mbit raw data per event, data reduction is compulsory and it is performed by Tracker Data Reduction boards. Critical issues for the Tracker are to maintain the required mechanical precision and low noise performance in space environment.

(a)

(b)
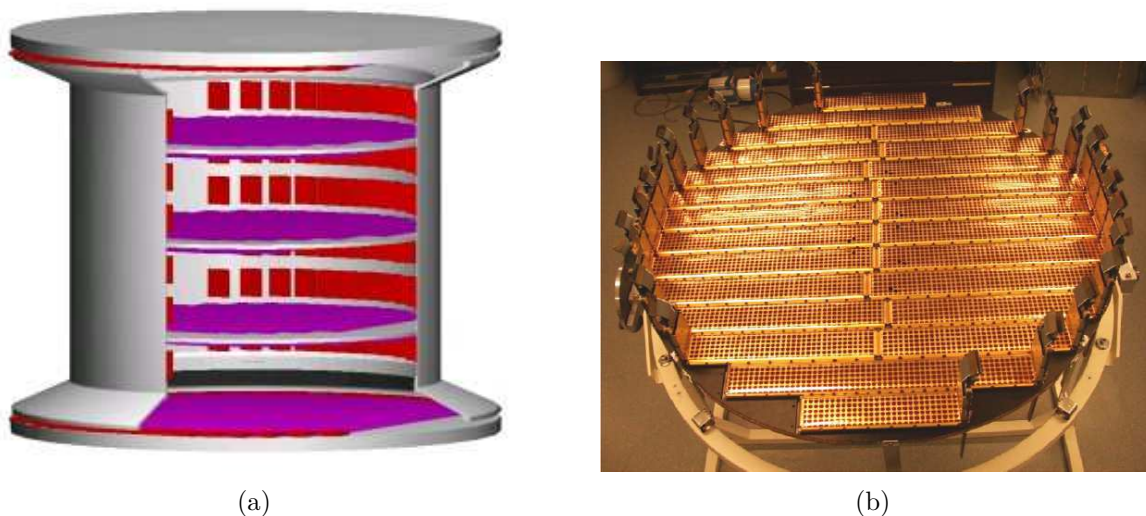
Figure 2.6: (a) Tracker cylindrical support structure. (b) One of the eight layers of microstrip-silicon sensors ready to be installed.

To evaluate the performance of the AMS Tracker 6 final ladders have been exposed to a test beam at CERN under proton and ion beams[41][42]. A good charge separation has been verified up to Iron. The Tracker spatial resolution for different ion species is presented in figure 2.7(a), as well as its rigidity resolution in figure 2.7(b).

2.1.3 Anti-Coincidence Counter

The Anti Coincidence Counter (ACC) system is placed between the innermost face of the magnet and the cylindrical support structure of the Tracker. This detector has the important task of flagging particles entering the tracking volume from the side, or even δ-rays or secondaries produced by normal particles or back-scattered against the electromagnetic calorimeter.

The ACC system is composed by 16 plastic scintillator paddles (Bicron BC–414) of $826 \times 230 \times 8$ mm, displaced in order to form a cylinder of an inner diameter of 109.1 cm. The whole detector structure can be seen in figure 2.8(a), whereas one counter prototype is shown in figure 2.8(b). Photons produced in the scintillator are routed to both paddle sides by means of wavelength shifting fibers (Kuraray Y-11(200)M) of 1 mm diameter, which are inserted in the scintillator according to a layout visible in figure 2.8(c), studied to ensure maximum uniformity in spacial trigger efficiency. At both ends of each paddle the wavelength shifting fibers are grouped into two bundles, that are matched to clear optical fibers (Bicron CF-98), transporting the scintillation light to the PM photocathodes, that are located far-away. Due to the high magnetic field, fine mesh phototubes have been chosen (Hamamatsu R-5946) and they are of the same kind as those used by the TOF
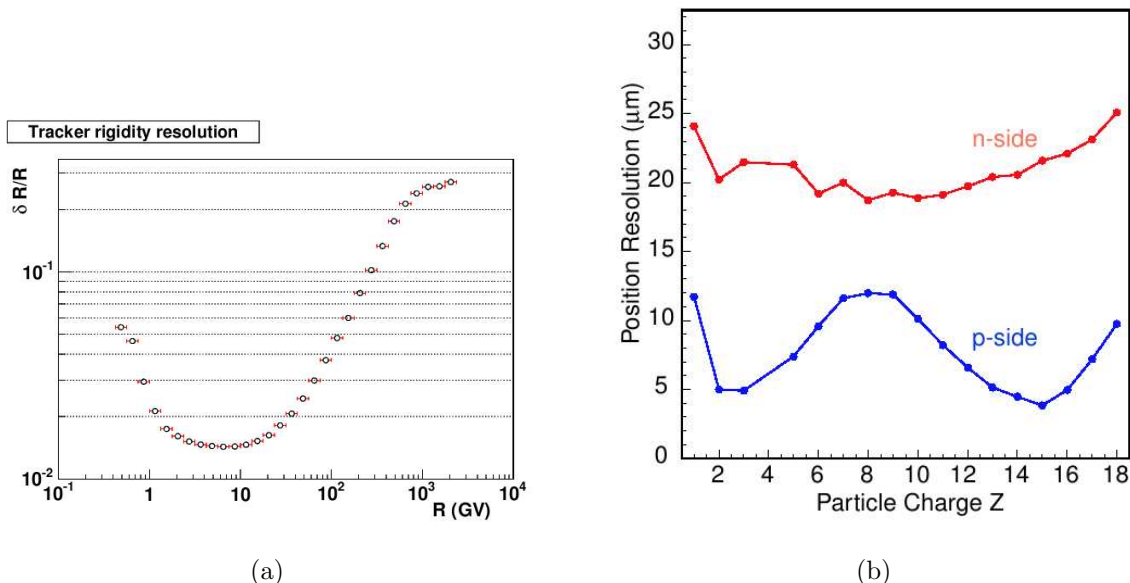
Figure 2.7: (a) Tracker rigidity resolution evaluated by means of AMS-02 MC data [43]. (b) Resolution of the position measurement in Tracker, as a function of the ion charge in the bending (p- side) and non bending (n-side) coordinates, estimated from beam test data [42].

system. The ACC signal is sent to the Level-1 trigger logic and it could be included as a Veto. The ACC system performances were also tested under a 10 GeV proton beam at CERN in 2003, showing no inefficiencies over 350000 events.

2.1.4 Ring Imaging Cherenkov Counter

AMS-02 detector includes a Ring Imaging Cherenkov Detector (RICH) [44, 45], placed on the lower part of the spectrometer, between the lower TOF and the Electromagnetic Calorimeter. The RICH is designed to provide an accurate measurement of the particles velocity in a wide energetic range above the TOF operating region and to give a precise and independent measurement of the nuclei electric charge up to Fe. Moreover, it will provide an additional contribution to the electron/proton and positron/antiproton separation.

As shown in figure 2.9, AMS-02 RICH detector is a proximity focusing type of imager, consisting of a radiator plane placed at the top of the counter, separated from the photon detection plane by a drift space, 46 cm deep. The detection plane has an empty $64 \times 64 \text{ cm}^2$ area in its centre, matching the active area of the electromagnetic calorimeter (ECAL) located below, in order not to spoil the ECAL measure. A high reflectivity mirror with conical shape encloses the detector volume increasing the geometrical acceptance. The radiator (radius 60 cm) is made out of aerogel tiles with a refractive index $n = 1.05$ and

(a)   (b)   (c)
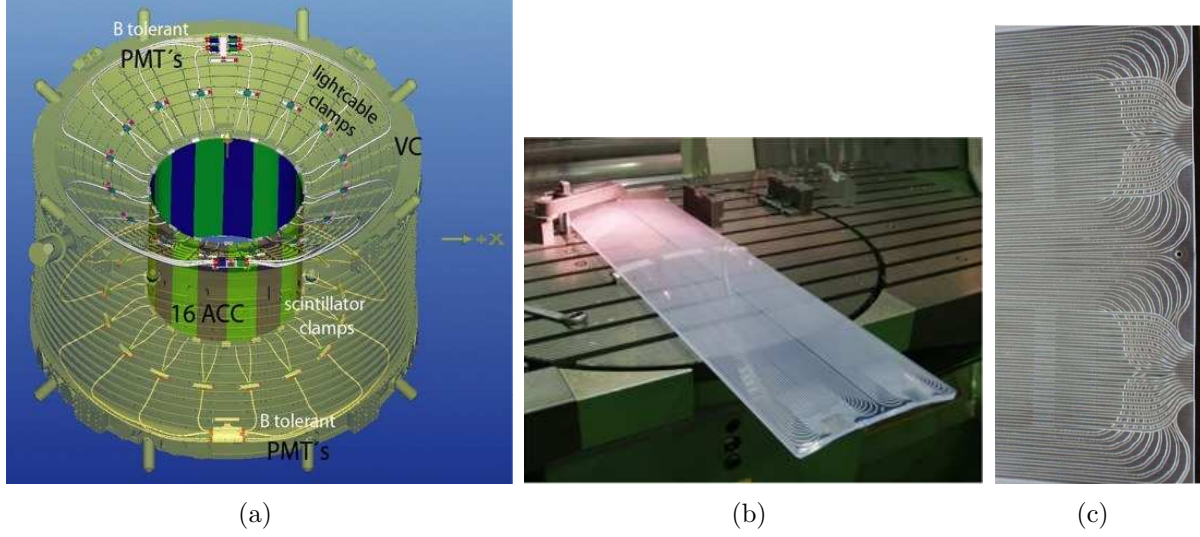
Figure 2.8: (a) 3-D view of Anti Coincidence Counter system installed on AMS-02. (b) Final ACC paddle. (c) Zoom on one counter side, where it is possible to appreciate the layout of the two readout groups of wavelength shifter fibres.

2.7 cm thick, surrounding the central 35×35 cm^2 area equipped with 5 mm thick Sodium Fluoride ($n = 1.33$). The detector plane supports an array of 680 light guides and 4×4 multianodes PMTs (R7600-00-M16 Hamamatsu).

A Ring Imaging Cherenkov detector measures the Cherenkov photon cone emitted when a charged particle with a velocity above the local speed of light crosses a radiator:

$$\beta_{\text{threshold}} = \frac{1}{n} \, , \tag{2.2}$$

whereas the Cherenkov cone angle is a function of particle β:

$$\theta_{\text{c}} = arcos(\frac{1}{n\beta}) \, . \tag{2.3}$$

The number of emitted photons is given by the Frank-Tamm formula[46]:

$$\frac{dN_{\text{ph}}}{dE} = \frac{2\pi\alpha}{hc} \, Z^2 L \, \sin^2 \theta_{\text{c}} \, . \tag{2.4}$$

The Cherenkov cone is reconstructed from the spatial coordinates of hit PMT pixels and knowing the direction of the incoming particle. So from the measurement of the angle θ_c is derived the particle β, whereas the photon counting (equation 2.4) gives an estimation of the absolute value of particle charge Z. The refractive index and the materials for AMS-02 RICH radiator are chosen in order to meet the requirements of wide energetic range, high number of emitted photons and β resolution. The momentum range per
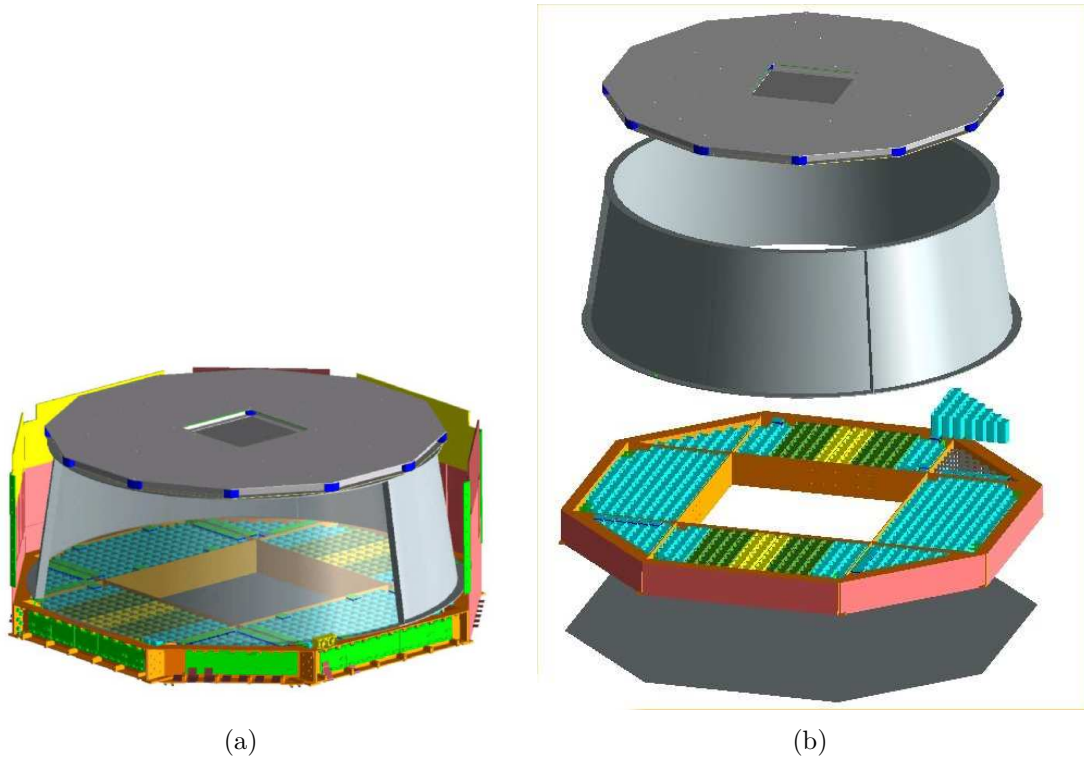
Figure 2.9: (a) RICH detector structure.(b) Exploded view of main RICH components; from the top: radiator, mirror and detection plane.

particle nucleon expected for different refractive indices is reported in the figure 2.10(a). The central region of the radiator has been covered with NaF tailes, to recover part of the lost acceptance due to the ECAL hole, as explained in figure 2.10(b). The momentum range covered by sodium fluoride radiator is between 1 and 5 GeV/c per nucleon, whereas higher momenta are provided by silica aerogel with a comfortable overlap for intermediate momentum values.

In order to define the detector design and study its performances, a RICH prototype was tested with cosmic muons and with ion beam at CERN in 2002 and 2003 [45, 47, 48]. The β resolution has been estimated, as well as the uncertainty of particle charge reconstruction, both with and without mirror. In figure 2.11(a) and figure 2.11(b) two typical rings formed in the RICH protype are shown, without reflection in the mirror and with reflection respectively.

2.1.5 Transition Radiation Detector

The AMS-02's uppermost element is a Transition Radiation Detector (TRD), whose flight model ready to be assemled is shown in figure 2.12(a). Together with the ECAL, TRD
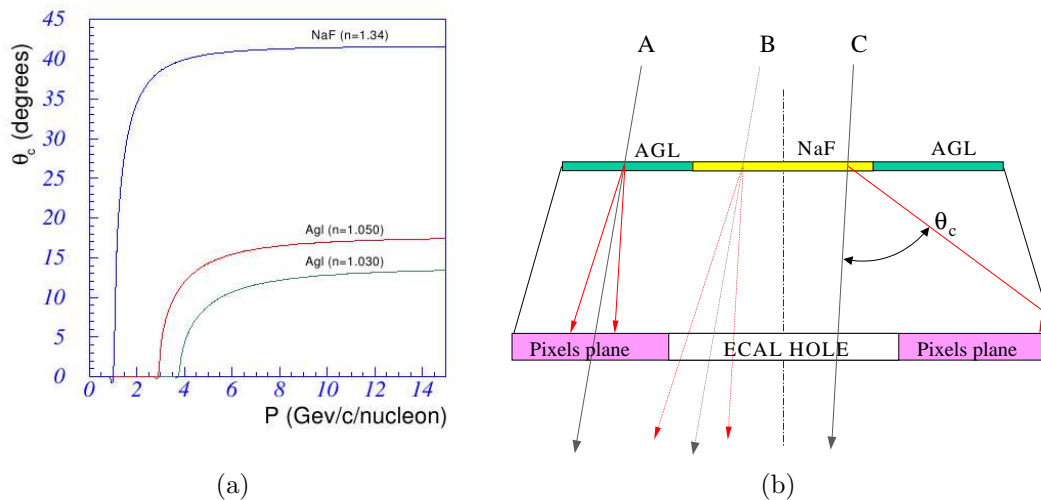
Figure 2.10: (a) Dependence of the Cherenkov angle on particle momentum for different radiator refractive indices. (b) Cherenkov photons emitted by particle B would fall in the ECAL hole in case of Aerogel radiator, but a similar particle C using NaF as a radiator generates a wider cone falling within the detector area, because of the different refractive indices.

plays an important role in the positron/proton separation, that is particulary important since cosmic radiation flux is dominated by protons. Transition radiation (TR) consists of soft x-rays which are emitted when charged particles traverse the boundary between two media with different dielectric constants ϵ as explained in figure 2.12(b). To fulfil all the electromagnetic continuity conditions at the boundary, a number of TR photons proportional to the particle relativistic Lorentz's factor $\gamma = E/m$ is produced. The phenomenon begins around $\gamma > 300$ for a typical radiator material, whereas TR photon flux tends to saturate for $\gamma > 1000$ [49, 50]. At a single boundary, the probability of emission is still very small, of the order of 10^{-2}, but this is enhanced by using a gleece radiator material (polyethylene/polypropylene) containing ~ 100 of such boundary transitions.

The AMS-02 TRD, as can be appreciated in figure 2.12(c), has a conical octagon structure of a carbon fiber and aluminum honeycomb sandwich material to minimize weight and keep maximum angular acceptance. It consists of 20 layers of straw tube modules and irregular fleece radiators with a total of 328 modules (16 straws each). The upper and lower 4 layers of tubes run along the field direction measuring bending plane and the 12 middle layers in the perpendicular direction measure the non bending plane. This configuration allows for 3D tracking in the TRD and supports a better resolution in the bending plane. The Transition Radiation Detector (TRD) for the AMS-02 detector requires a detection medium of Xe/CO_2 gas mixture (80/20). This gas has to be stored, mixed and distributed through the TRD and these tasks are accomplished by the TRD

<div align="center">(a)   (b)</div>
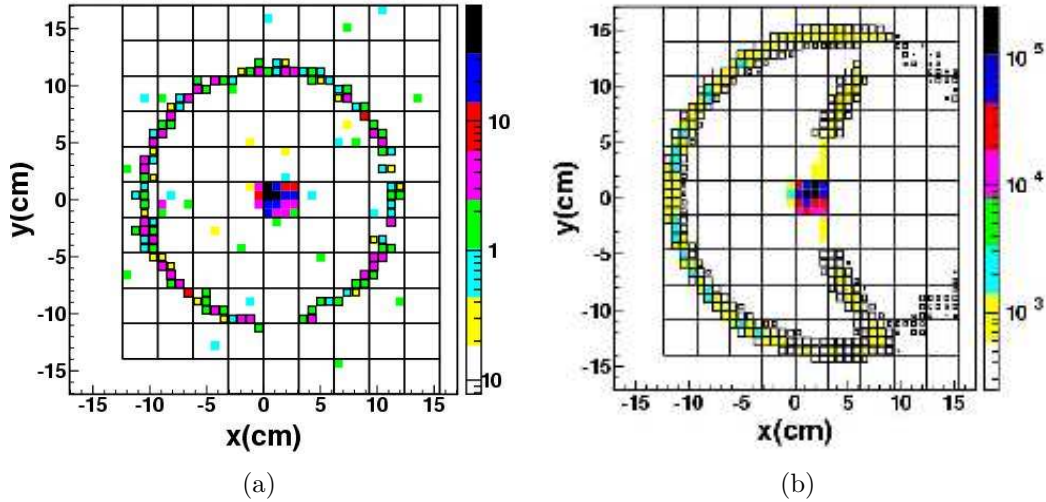
Figure 2.11: (a) A ring generated by a Boron ion ($Z = 5$) in the RICH prototype detection plane.(b) Signal produced by an event of Oxigen ($Z = 8$) with reflection in the mirror (the not coulored right part of the ring is added artificially by the reconstruction algorithm) .

Gas System[51].

2.1.6 Electromagnetic Calorimeter

The Electromagnetic Calorimeter (ECAL) of the AMS-02 experiment is a fine grained lead-scintillating fibre sampling device designed to perform a precise 3-D imaging of the longitudinal and lateral shower development, providing high discrimination between hadronic and e.m. cascades and good energy resolution[52, 53, 54]. A picture of the flight model is shown in figure 2.13(a).

The ECAL is located at the bottom of the experiment and it covers the reduced field of view left by the hole in the RICH detection plane. The ECAL has an active area of 658×648 mm^2 and a thickness of 166.5 mm, for a total weight of 496 kg. It is composed of nine superlayers, each one consisting of grooved lead foils, 1 mm thick, interleaved with layers of 1 mm diameter scintillating fibers glued by means of epoxy resin. All the fibres included in a superlayer are running in one direction only, so the detector imaging capability is achieved by piling up in turn superlayers with fibres along bending direction (4 layers) and non bending one (5 layers), as shown in figure 2.13(b).

In each superlayer the light signal coming from the fibers is collected by 36 photomultipliers (R7600 00-M4 Hamamatsu) placed altenatively on one side, through plexiglass light guides, shaped as a truncated pyramid. Each photomultiplier has a cathodic effective area

(a)   (b)

(c)
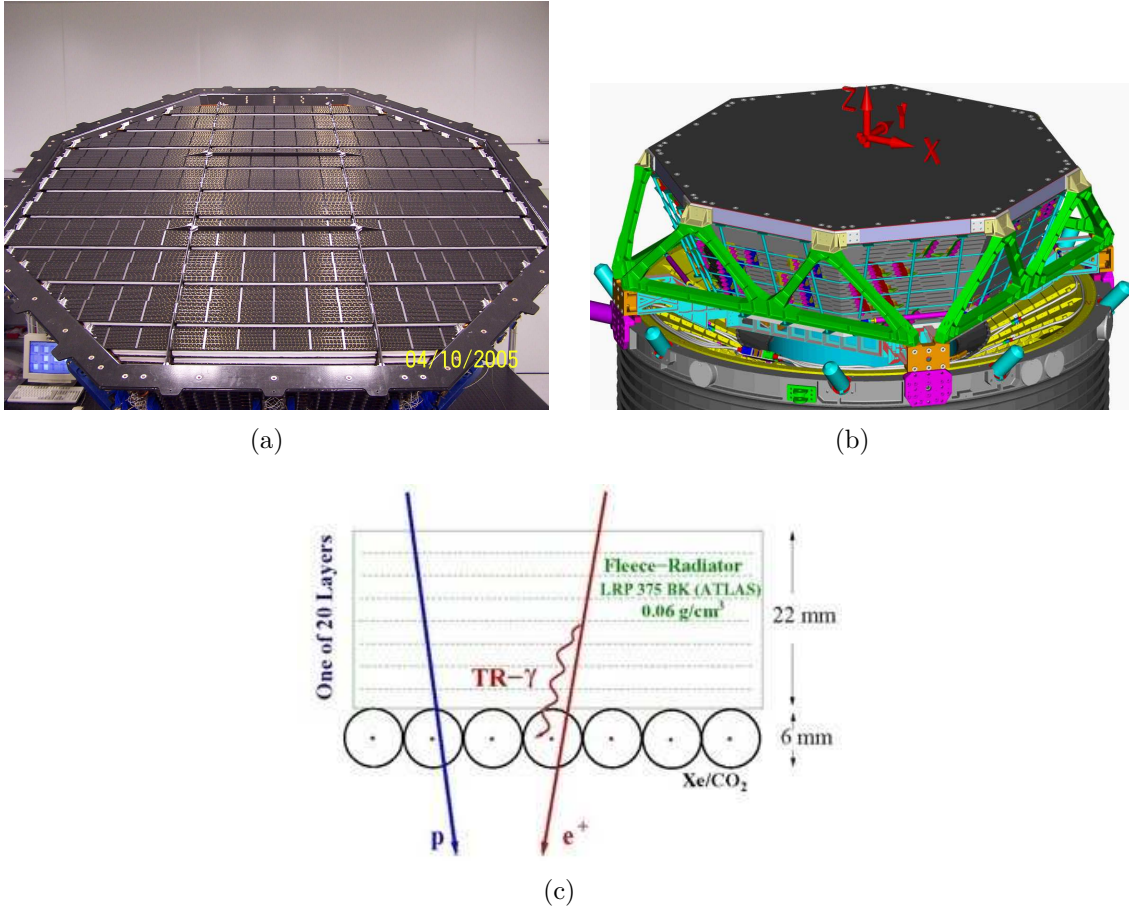
Figure 2.12: (a) Picture of the TRD flight model. (b) TRD mechanical structure. (c) Working principle of Transition Radiation emission and collection in TRD.

of 18×18 mm^2 divided into four square regions of equal area: the resulting granularity is therefore 9×9 mm^2. The region read out by one of the four PMT cathodes is called cell. The calorimeter is subdivided into 1296 cells, corresponding to 324 photomultipliers. A charged particle impinging vertically on the ECAL will cross ~ 17 radiation length and the shower longitudinal profile is finally sampled by 18 independent measurements. On july 2002 the engineering model of the ECAL partially equipped with 63 PMTs in one corner was tested at CERN SPS beam line. The energy resolution as a function of the beam energy are shown in figure 2.14. The calorimeter also provides a stand alone photon trigger capability to AMS-02 as it will be discussed in § 4.3.3.

(a)
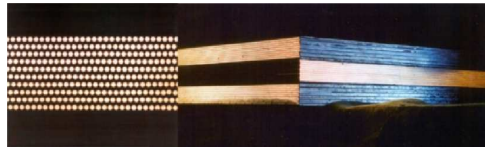
(b)

Figure 2.13: (a) Picture of the ECAL flight model. (b) Fibers in a superlayer (left) and 3 superlayers piled up with crossed x and y fibers direction (right) .
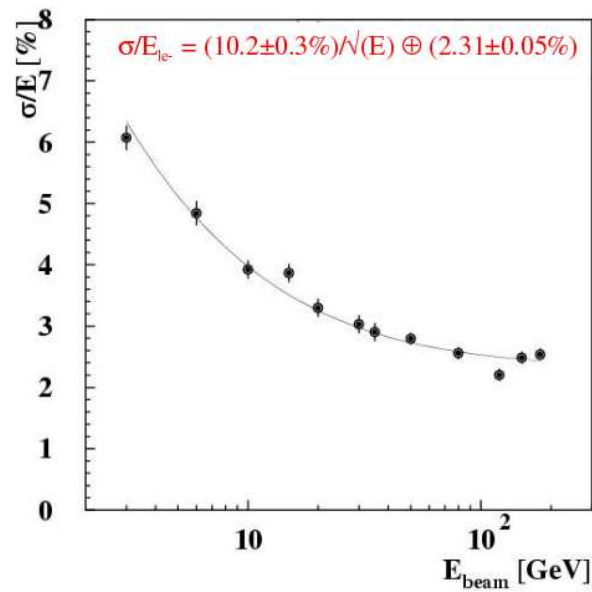
Figure 2.14: ECAL Energy resolution as measured during beam test 2002 at CERN SPS [55].

Chapter 3

AMS-02 Time of Flight System

The antideuteron signal from primary supersymmetric origin is expected to be detectable at low energy, below 1–1.5 GeV/n, as largely presented in the first chapter. In the AMS-02 spectrometer, the measurement of the particle β is provided both by the Time of Flight (TOF) and the Ring Imaging Cherenkov (RICH) detectors, in two complementary energetic ranges. In particular, the interesting low energy region is covered by TOF, while the RICH starts operating for $\beta > 0.75$. The latter detector is characterized by a much better β resolution (0.1%), but smaller acceptance.

The TOF system covers the full acceptance of the AMS-02 spectrometer and, being made of fast scintillator counters, it is in charge to provide the fast trigger (FT) to the experiment with a negligible inefficiency. Its time resolution (~ 0.1 ns) is good enough to provide a separation between upward and downward particles at the 10^{-9} level, a fundamental feature for the antimatter search. Finally, from the measurement of the particle energy loss, the absolute value of its charge can be derived up to $Z \simeq 20$ [56].

A detailed study of the particle detection performance of the TOF is therefore needed as well as an extimation of its behaviour and stability under space conditions. Two beam tests were carried on to study the TOF velocity and charge resolution. In addition, a set of tests were performed to estimate the radiation damage and the thermal dependance of the detector properties, whereas qualification tests are required to verify its behaviour at space conditions.

3.1 TOF Design overview

The TOF system of AMS-02, completely developed and built at the INFN Laboratories of Bologna, consists of four planes of plastic scintillator counters covering the whole AMS-02 acceptance. In each plane, with a sensitive area of ~ 1.2 m^2, the paddles are partially overlapped to avoid geometrical inefficiencies, while counters of adjacent planes are orthogonal, in order to guarantee a good granularity to the trigger. The central scintillator counters are 1 cm thick, 12 cm wide, with lenght variable from 117 to 134 cm. To cover
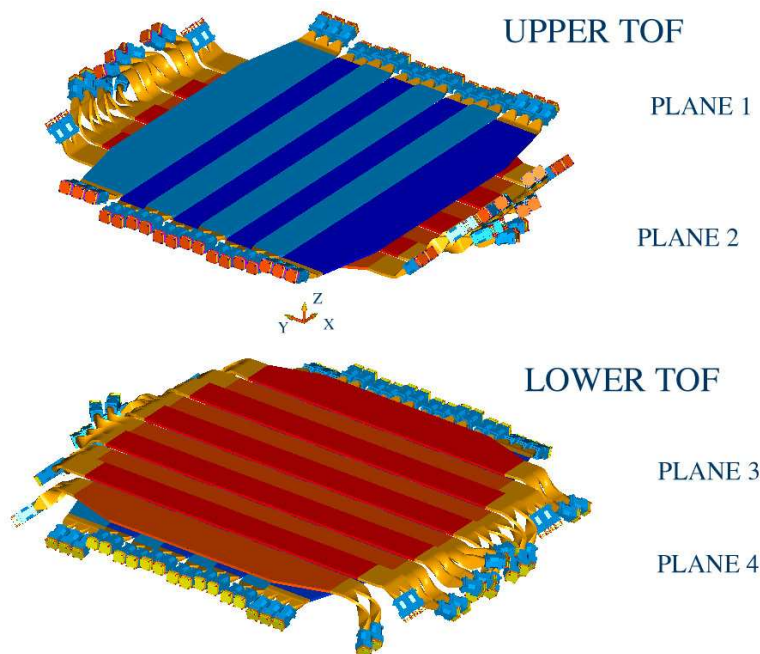
Figure 3.1: Scheme of the AMS-02 TOF. Upper and Lower TOF are separated by a distance of about 1.2 m.

the whole geometrical aperture, the external counters of each plane have a trapezoidal shape. At trigger level, the TOF system is seen as inner matrices of 6×6 and 6×8 (for plane 3) squared cells of 11.5 cm side, while the surrounding cells have a larger granularity.

The four TOF planes are arranged as shown in figure 3.1 to form two units placed one above and the other below the superconducting magnet at a distance of around 1.2 m, called Upper TOF (UTOF) and Lower TOF (LTOF). The two planes of the UTOF are made of 8 scintillation counters each one, while LTOF has 10 and 8 scintillation counters respectively in plane 3 and 4. Counters of planes 1 and 4 are parallel to the magnetic field direction (x-axis), whereas those of planes 2 and 3 are parallel to the y-axis.

The light emitted by means of scintillation effect when a charged particle crosses the paddle sensitive area, is collected at both ends of each counter by two (or three) PhotoMultiplier Tubes (PMT) per side. In order to minimize the effect of the strong magnetic field generated by the superconducting magnet, whose intensity reaches 0.2 T for some PMTs, a set of bent light guides modelled *ad hoc* was produced in such a way to minimize the angle between the field direction and the PMT axis. *Fine mesh* PMTs (Hamamatsu R5946) were chosen for their high magnetic field tolerance. The reduced weight budget (about 238 kg for the whole TOF system) imposed a lower number of PMTs per counter side and a lower number of scintillator counters per plane with respect to AMS-01 detector.
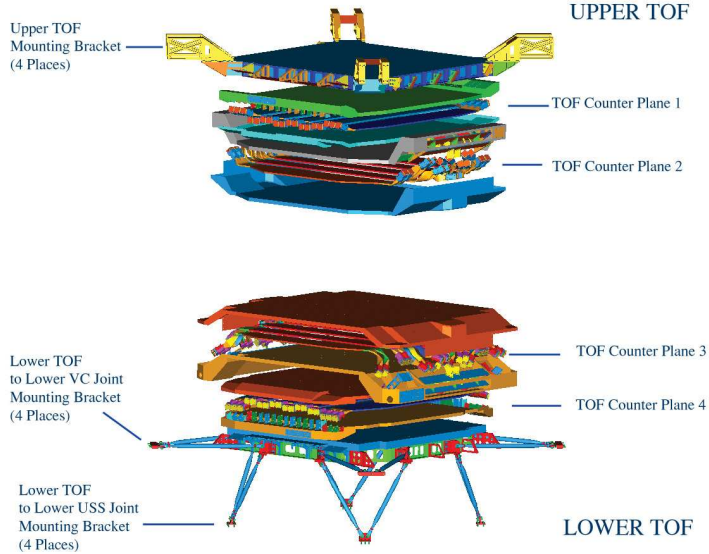
Figure 3.2: Exploded view of Upper and Lower TOF systems.

The 34 paddles are mounted in the 4 planes, which are enclosed by aluminized carbon fibre boxes. Internally, the two planes are connected to each other through carbon fibre supports and aluminum screws. Outside the assembly is fixed to the support structure, a "sandwich" made of an aluminum honeycomb panel glued to two aluminium sheets, then attached to a main aluminium structure. In the Lower TOF the main structure is connected to the LUSS (Lower Unique Support Structure) by means of 16 rods. An exploded view of the LTOF and the UTOF mechanical structures is shown in figure 3.2.

3.1.1 TOF scintillator counters

The TOF system is formed by 34 paddles subdivided into 4 planes, arranged as shown in figure 3.1. The sensitive material is an organic plastic scintillator (polyvinyltoluene EJ-200 provided by Eljen-Technology [1]), which combines two important properties: fast timing and long optical attenuation length.

- In a scintillator, the energy lost by charge particles crossing the scintillator material is (partially) emitted in form of visible photons. On the base of the *fluorescence* machanism, the excited molecules promptly decay from an unstable state releasing photons, that in first approximation follow an exponential law:

$$N = N_0 \exp \frac{-t}{\tau} \ , \tag{3.1}$$

---

[1]`http://www.eljentechnology.com/products.html`.
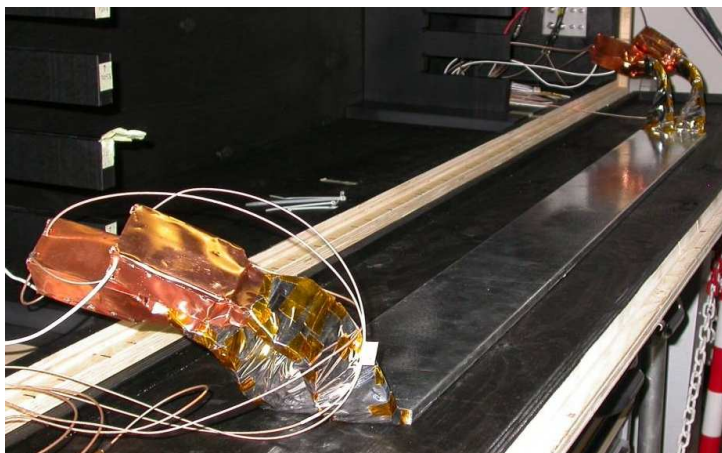
Figure 3.3: One TOF counter ready to be assembled in the TOF structure.

where N is the number of emitted photons at time t, N_0 is the number of emitted photons at time $t = t_0$ and τ is the decay constant, which for the scintillator chosen for AMS-02 TOF is of about 2.1 ns.

- The emitted photons may be reabsorbed while passing through the scintillator material itself. This effect is mainly caused by an unavoidable partial overlapping of emission and absorption spectra. Macroscopically, the light intensity I at a distance x between the photons production and their detection decreases with x as follows:

$$I(x) = I(0) \exp \frac{-x}{\lambda} \ , \tag{3.2}$$

where the parameter λ is the bulk attenuation lenght, which for EJ-200 is about 3.8 m, as measured from the producer. In addition, the counter geometry plays an importat role on the actual light attenuation as has been previously studied [57, 58]: for example the measured attenuation lenght of TOF counters 136 cm long λ and with straight light guides was estimated about $\lambda \sim 230 \pm 15$ cm. Because λ is sensibly greater than the counter length, the attenuation length does not represent a problem for the TOF counters.

These characteristics make EJ-200 scintillators particularly useful for time-of-flight systems using scintillators greater than one meter long.

All the TOF counters have a rectangular shape except for the outermost ones, which are trapezoidal. The shape of the external counters was chosen to match the desired geometrical aperture and at the same time fulfil the weight constraints. Inside the counter, the scintillation light is internally reflected until it reaches the two edges, where plexiglass light guides bring it to the photomultipliers. The figure 3.3 shows a typical counter with the light guides and the photomultipliers.
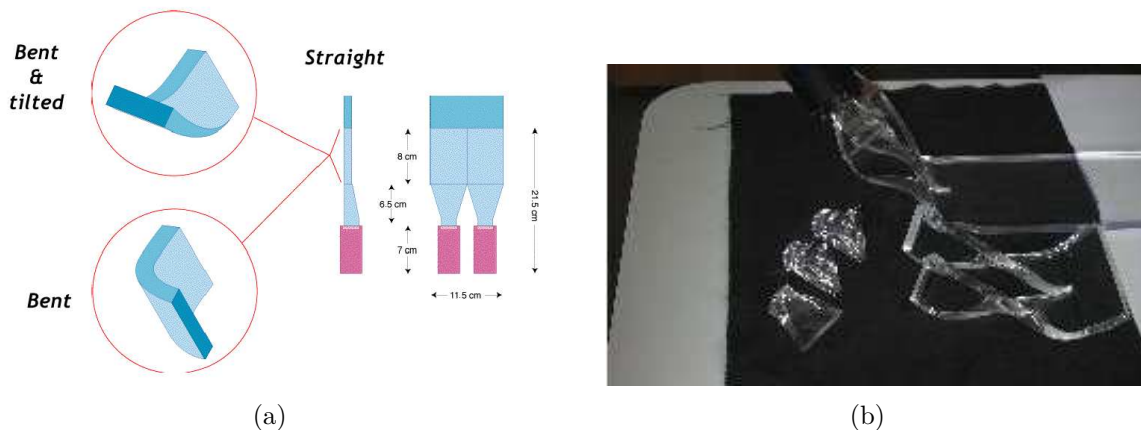
Figure 3.4: (a) Straight, tilted and twisted light guides have been built with special tools. In the scheme it is possible to distinguish the extender, the light guides and the conical junctions. (b) A picture showing twisted light guides and conical parts.

The light guides consist of three plexiglass parts shown in figure 3.4: a straight *extender* that prolongs the scintillator paddle which; one bent and/or twisted light guide piece per each PMT (only for planes 2 and 3); a *conical* junctions which the PMTs are fixed to. All the conical parts are identical to match both the rectangular shape of the light guides and the circular photocathode of the PMT. The shape of each light guide has been determined according to the position of the PMT in order to reduce the angle between the magnetic field and the PMT axis. Between the guide and the PMT window a soft transparent pad (made of Dow Corning 93-500 material) is placed to guarantee the needed optical and mechanical couplings.

The phototube is enclosed into a black plastic box (wrapped with a conducting foil as shown in figure 3.3), which provides the fixing to the light guide. The scintillator, the extenders and the light guides are wrapped with a thin Mylar foil, that both improves reflectivity blocking external light and protects the surfaces from dust and small debris that may be produced by the enclosing carbon fiber 0.5 mm thick boxes, that provide the needed rigidity. Light tightness is given by a large carbon fiber envelope 0.7 mm thick that encloses the couple of adjacent planes and their photomultipliers.

3.1.2 Fine-mesh photomultipliers

Time Of Flight System of AMS-02 will operate in the strong (2.5 kG) and badly shaped fringing field of the dipole superconducting magnet. This fact led to select both for TOF and ACC systems of AMS-02 the cylindric Hamamatsu R5946 *fine mesh* photomultiplier with tightly packed mesh dynodes, which, thanks also to their quite high operating voltages (about 2000 V), have a relatively low sensibility to magnetic field. These PMTs can

(a)   (b)
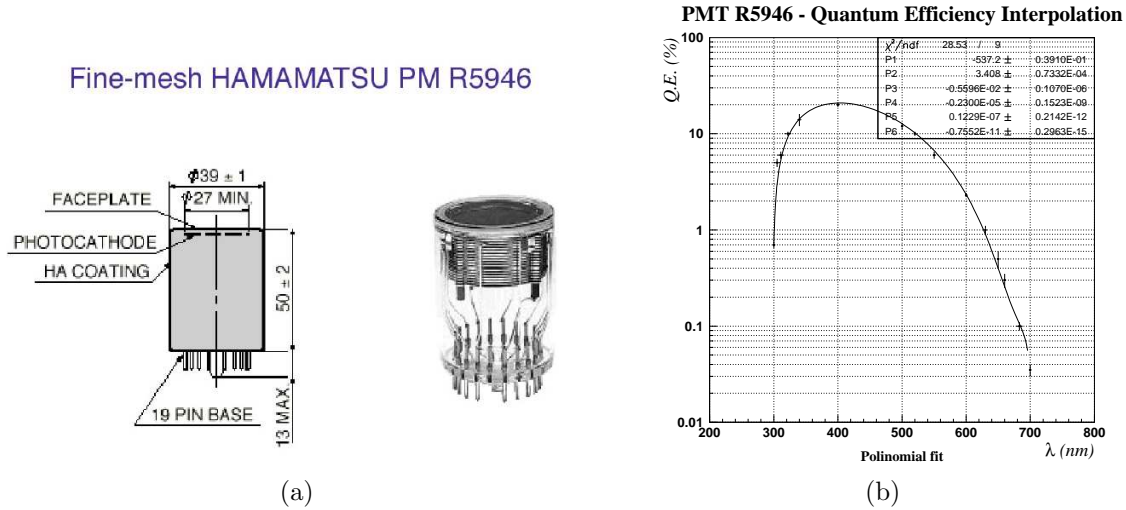
Figure 3.5: (a) Scheme of Hamamatsu R5946 fine mesh PMT. (b) R5946 PMT quantum efficiency fit of the experimental data provided by the producer.

indeed work with the high intensity field of AMS-02, but they show a strong dependence on the angle between the field direction and the PMT axis. The measurements carried on in Bologna with magnetic field up to 0.4 Tesla show that angles larger than 20 degrees are critical. For higher values the PMT single photoelectron response and the PMT transit time worsen rapidly [59, 60]. PTMs of planes 1 and 4, and many phototubes of the other two planes are positioned with angle lower than 20 degrees. Tilted and twisted light guides are used to avoid angles greater than 35 degrees.

The Hamamatsu R-5946 PMT, whose sceme is shown in figure 3.5(a), has a bialkali photocathode, a boron-silicate glass window and 16 bialkali dynodes. The spectral response shown in figure 3.5(b) ranges from 300 to 600 nm with a maximum response at $\simeq 420 \pm 20$ nm (corresponding to a quantum efficiency of about 20%) [61]. The light from every paddle is transmitted to two PMTs (or three) per side for redundancy.

Some restrictions are imposed to the choice of the disposition of the 144 PMTs on the TOF. The PMTs placed on the same counter side should have similar gain and working voltage in order to have similar response and timing. In addition, these PMTs have to work with voltage below 2300V and they are powered in couple. To optimize their disposition, considering also the effect of the magnetic field, the combined use of two meta-heuristc algorithms, simulated annealing and genetic algorithm, was implemented and an accettable solution was found [62].

44
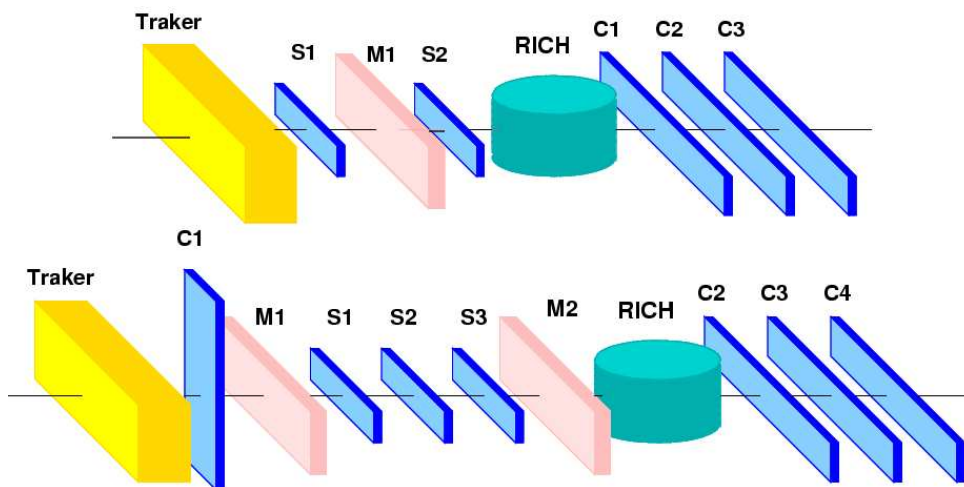
Figure 3.6: Schematic views of the test beam setup in 2002 (above) and 2003 (below), where C_i are the TOF counter prototype, M_i are the wire chambers and S_i are additional scintillator counters used to give the common trigger.

3.2 TOF Performance: beam test

Prototypes of AMS-02 TOF polyvinyltoluene scintillator counters were tested at CERN in 2002 and 2003 with standard NIM and CAMAC electronics at the SPS ion beam facility. The primary line (20 A GeV/c Pb in 2002 and 158 A GeV/c In in 2003) was directed against a Be target producing secondary nuclei from proton to the incident ion itself with a small spread in β [63]. Mass over charge selection was done tuning the magnets of the T8 selection line. Runs with A/Z=1, 2, 9/4, 7/3 were used to get large statistics of all main CR species.

The schemes of the setup adopted in beam tests 2002 and 2003 are illustrated in figure 3.6. During the 2003 test [64, 65], 4 TOF counters equipped with different light guides, were set along the ion beam line together with AMS-02 RICH [47][44] and Tracker prototypes [41, 42]: 3 over 4 scintillators were made of Eljen EJ-200, adopted for the AMS-02 TOF, whereas the last one was made of Bicron BC-408, used in AMS-01.

3.2.1 Velocity measurement

The TOF system allows the reconstruction of the particle velocity $v = \beta c$ through the measurement of the time $t = \ell/v$ spent by the crossing particle to go along the path $\ell = L/\cos\theta$ between upper and lower TOF planes (L is the distance between the planes
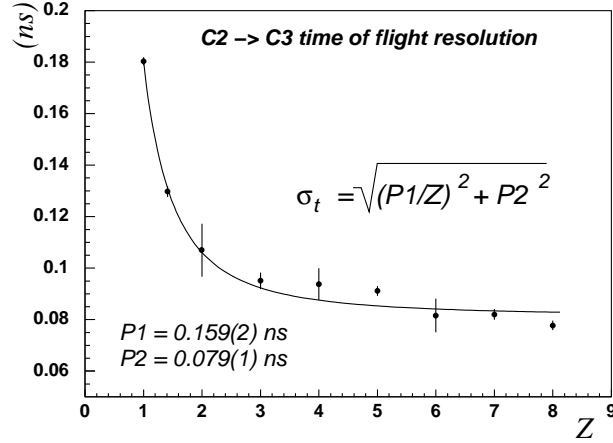
Figure 3.7: Time of flight resolution vs. atomic number from beam test data.

and θ is the trajectory angle). Hence, the time of flight t:

$$t = \frac{L}{\beta c \cos \theta} \; , \tag{3.3}$$

with associated Gaussian uncertainty σ_t. The derived uncertainty on β will be:

$$\sigma_\beta^2 = \frac{L^2}{c^2} \left(\frac{\sigma_t^2}{t^4 \cos^2 \theta} + \frac{\sigma_\theta^2 \sin^2 \theta}{t^2 \cos^4 \theta} \right) \simeq \frac{L^2}{c^2} \frac{\sigma_t^2}{t^4 \cos^2 \theta} \; . \tag{3.4}$$

The second term inside the parentheses can be safely neglected thanks to the very good angular resolution of the Tracker.

Thus, the β resolution is strictly correlated to the time of flight resolution, which was measured between two different TOF counters both during beam test 2002 and 2003. The resolution obtained in the worst case for counters with curved and twisted light guides is shown in figure 3.7 and it is 180 ps for protons and about 100 ps for light ions [66, 64].

3.2.2 Particle charge determination

The absolute value of the electric charge of a particle crossing the scintillator can be measured by looking at its energy loss. For particles heavier than electrons, the mean rate of energy loss is a function of the properties of the medium (density ρ, atomic number z and mass number A) and of the incident particle velocity β and charge Z, as espressed from the well known Bethe Bloch formula [67]:

$$-\frac{\mathrm{d}E}{\mathrm{d}x} = 2\pi N_A r_e^2 m_e c^2 \rho \frac{Z}{A} \frac{z^2}{\beta^2} \left[\ln \left(\frac{2m_e \gamma^2 v^2 W_{\max}}{I^2} \right) - 2\beta^2 - \delta - 2\frac{C}{z} \right] , \tag{3.5}$$

Ion	σ_Z	Ion	σ_Z	Ion	σ_Z	Ion	σ_Z
H	0.15	B	0.21	F	0.29	Al	0.34
He	0.14	C	0.24	Ne	0.37	Si	0.5
Li	0.17	N	0.29	Na	0.34	P	0.4
Be	0.23	O	0.31	Mg	0.34	S	0.4

Table 3.1: TOF counter mean charge resolution up to S ion measured with beam test data taken in 2003.

where r_e and m_e are the classical radius and the mass of the electron, N_A is the Avogadro number, I is the mean ionization energy of the medium, W_{max} is the energy transferred in a single collision. The parameter δ represents the *density effect* which acts at high energies and C is the *shell correction* working at low energies. In plastic scintillator the relativistic rise is negligible and therefore, in the energetic range explored by AMS-02, the energy loss can be roughly considered not dependent on particle β and proportional to its Z^2.

Two measurements of the charge, which are not statistically independent, are provided from the two-PMT anodes signal coming from the two sides of each counter. The collected data during beam test 2002 and 2003 were analysed and the best side of each counter was used to estimate the particle charge. The charge resolution reported in Table 3.1 for ions up to S is the average of the four tested counters. Custom electronics boards [68] are being developed for AMS-02, which will extend the charge range up to $Z = 20$. TOF scintillator counters show a good charge resolution in particular up to Nitrogen and Oxygen nuclei.

During beam test a prototype of the RICH detector was placed along the same beam line and a common trigger was sent to both systems. An independent value of the particle $|Z|$ was reconstructed by RICH from the counting of the number of the detected photo-electrons along the ring. A study of the combined Z reconstruction power was done and an example of the correlation between the two measurements is shown in figure 3.8(a).

The scintillator response is not a simple linear function of the ionization energy density, but it is well modelled by the Birks-Chou law [69]:

$$\frac{\mathrm{d}\mathcal{L}}{\mathrm{d}x} = \frac{A(\frac{\mathrm{d}E}{dx})}{1 + kB(\frac{\mathrm{d}E}{\mathrm{d}x}) + C(\frac{\mathrm{d}E}{\mathrm{d}x})^2} \; , \tag{3.6}$$

where $\mathcal{L}$ is the scintillator luminescence which is in first approximation proportional to the energy loss $\mathrm{d}E/\mathrm{d}x$, B is the density of excited or damaged molecules, k is the probability of these molecules to absorb a photon, so called *quenching effect*, C is a small correction parameter due to saturation.

Cosidering the beam tests data, all particles crossed the same material with approximately the same β, hence the mean energy loss is a function only of their atomic number
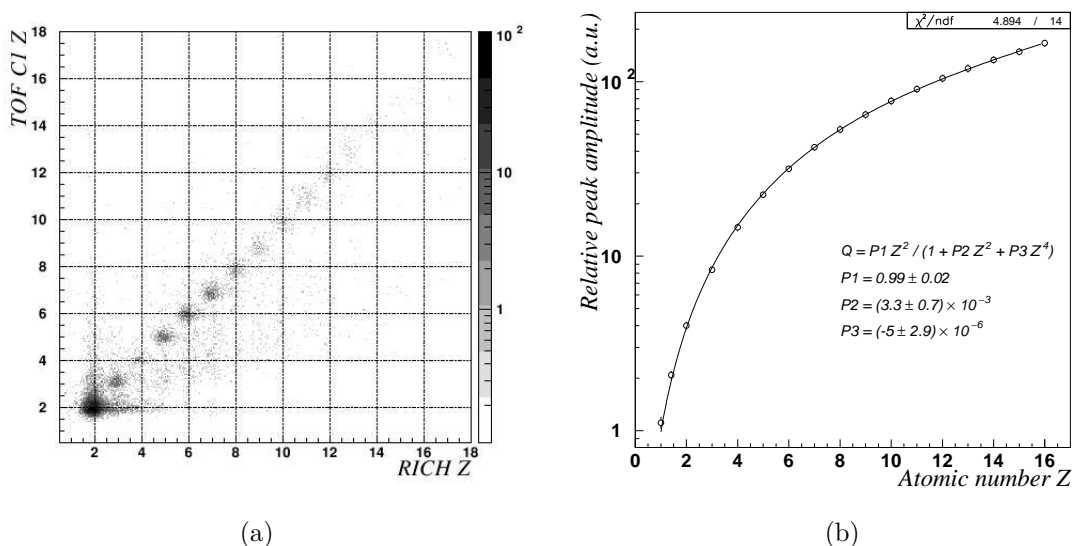
Figure 3.8: (a) Correlation between TOF and RICH particle Z measurements from beam tests data 2002. (b) Fit of the measured average amplitude in arbitrary units vs. the atomic number Z.

Z, and the measured charge of the PMT anode signal is related to the particle Z as follows:

$$Q = \frac{P_1 \, Z^2}{1 + P_2 \, Z^2 + C \, Z^4} \, , \tag{3.7}$$

where the parameter P_1 is proportional to the PMT gain, P_2 to the Birk parameter kB and P_3 to the Chou parameter C. P_2 and P_3 depend only on the scintillator properties. The fits of the luminous response vs. Z for all the tested counters give compatible results for kB and C parameters. Figure 3.8(b) shows the global fit obtained with the averaged amplitude peaks of the four counters tested in 2003 [65, 64, 66]. The uncertainties associated to each point are of the order of 5%.

The estimation of the Birks-Chou parameters kB and C for polyvinyltoluene EJ-200 scintillators yelds to: $kB = (1.2 \pm 0.5) \times 10^{-3}$g MeV^{-1} cm^{-2} and $C = (-6.4 \pm 6) \times 10^{-7}$g^2 MeV^{-2} cm^{-4}.

3.3   Operation in space

The AMS-02 experiment to be installed on the ISS for a period of at least three years, will experience typical external ISS payloads environmental conditions. In particular, the ISS, orbiting in its Low Earth Orbit, receives typical fluxes of LEO satellites. TOF location in AMS-02 makes it subjected not only to these direct impinging fluxes (Solar
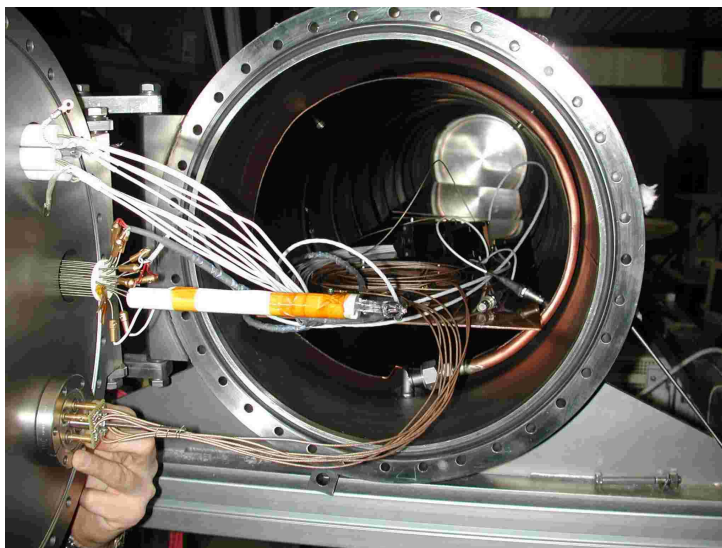
Figure 3.9: Picture of the thermo-vacuum simulator built in the Bologna INFN-Laboratories.

visible radiation, Hearth albedo and Infrared Earth contribution), but also the reflections contributions of the ISS elements. The preferable and likely most probable attitude will be the so called MPA (Minimum Propulsion Attitude) which minimizes, when the Space Shuttle is docked to the ISS, the propellant needed to maintain the orbit against the drag forces of the residual atmosphere. The percentage of the TOF bulk thermal dissipation is low compared to the external impinging heat fluxes, so the proposed thermal concept is based on the detector completely covered by Multi Layer Insulation (MLI) [70]. Carlo Gavazzi Space (CGS) is responsible for the TOF thermal model.

The TOF system must be able to operate in space for a long time without human intervention and to survive the strong acceleration produced by the shuttle launch. A set of tests has been arranged in order to study the behaviour of the TOF components in the foreseen conditions of temperature and radiation. A space qualification test required by NASA, consisting of a termo-vacuum test (TVT) and of a vibration test, has to be done on TOF Upper and Lower flight module detectors. LTOF succesfully passed these test in July and October 2006, while for UTOF are scheduled for June 2007.

3.3.1 PMT thermovacuum test

In order to reproduce space temperature and vacuum conditions expected for the TOF system, a space simulator, which is shown in figure 3.9, was built in the Bologna INFN-Laboratories. A set of PMT Hamamatsu R-5946 was tested in the simulator with pressure kept at about 10^{-7}–10^{-6} mbar and temperature varying between $-30°$ and $+55°$C.

Firstly, the stability at high temperature of the main PMT characteristics was estab-
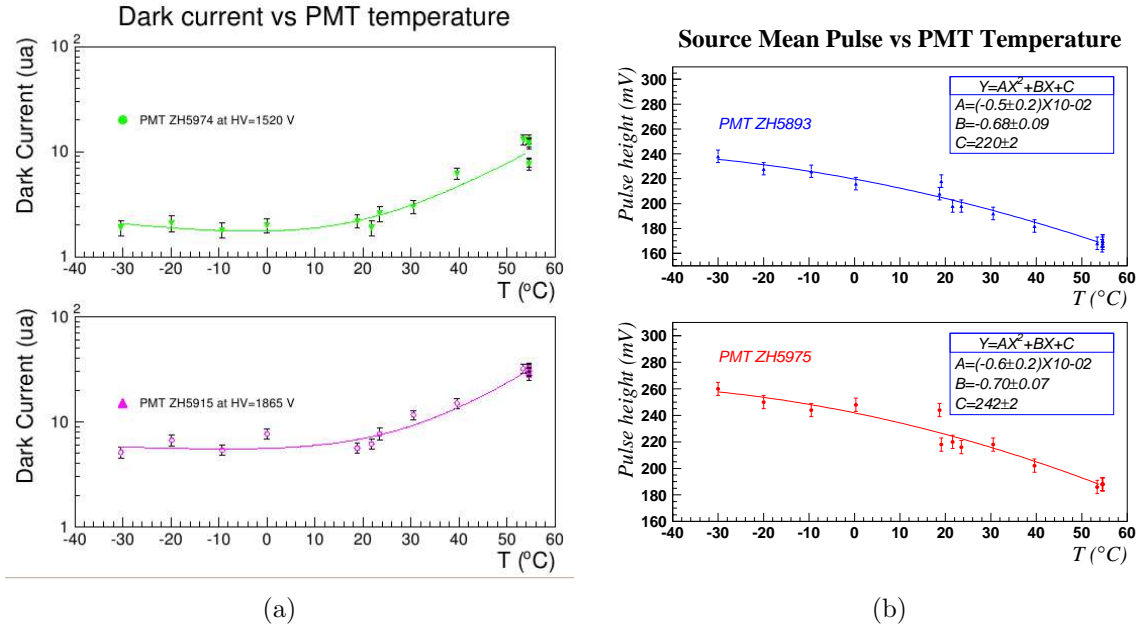
Figure 3.10: (a) Dark current measured for two PMTs as a function of temperature. (b) PMT pulse height as a function of temperature.

lished calibrating them before and after being kept inside the simulator one week with power supply off (non operating) at +60°C and one week with HV on (operating) at +55°C.

A second test was carried on to study the PMT bahaviour as a function of temperature. Inside the simulator both PMT dark current and pulse height signals were monitored at different temperatures. The dark current measured for 4 PMTs shows a rapid rise after 20°C in agreement with literature. Other 2 PMTs were equipped with a small scintillator and a β source in order to measure their pulse height. Both measurements were obtained by means of a digital oscilloscope and the results are illustraded in figure 3.10.

The measured PMT pulse heights are well fitted with a parabola accordingly to the literature [71], and they are compatible with each other. As confirmed by our results, the quantum efficiency for bialkali photocathodes, like them that are mounted in R-5946 PMTs, is expected to decrease with temperature with an anode sensitivity temperature coefficient of about -0.4% per Celsius degree at the wavelength of maximum emission (425 nm) of EJ-200 plastic scintillator (Ref. to figure 8-1 page 204 of [61]). To conclude, fine mesh PMTs seem not suffer a long exposure at high (55°C–60°C) temperatures, but they show a clear output variation with temperature, in agreement with literature within the operating range foreseen for the TOF on the ISS.
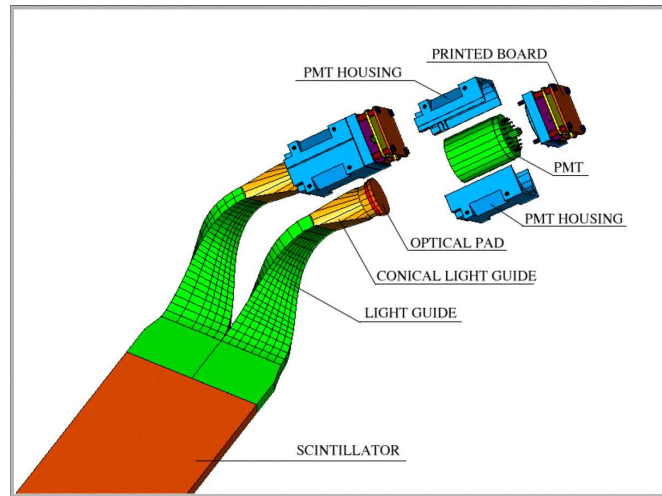
Figure 3.11: TOF counter side exploded view

3.3.2 TOF radiation hardness

The TOF materials must be radiation hard enough to keep their characteristics stable for 10 years in space, where the absorbed dose is estimated around 0.5 krad/year. It is known that the radiation-induced darkening occurs in the majority of optical materials. Indeed, organic materials are sensitive to radiation because of the generation of reactive intermediate free radicals, which takes place when covalent bounds are excited or ionized by radiation [72, 73]. A set of studies about the radiation damage on each single part making up the TOF counter was performed using gamma sources.

One side of the TOF counter, including epoxy joints and light guides, was irradiated at the GIF (Gamma Irradiation Facility - CERN) with ^{137}Cs gamma source. At 60 cm from the source, where the counter was placed, the dose rate was of the order of 11.5 rad/h (in water). A total dose of 4.5 ± 0.4 krad in the central part of the counter and 3.1 ± 0.3 krad at one side was achieved. No measurable changes were found in the attenuation length and in the number of photoelectrons, when compared to the measurements done before the irradiation and respect to the non-irradiated side.

In collaboration with the ISOF-CNR Institute of Bologna, several radiation damage tests were carried out on every TOF counter part: a silicon optical pad, a plexiglass conical light guide and a small sample of scintillator ($42 \times 55 \times 10$ mm^3). These parts can be clearly distinguished in figure 3.11.

The facilities employed were: the Gamma Cell of ^{60}Co (ISOF-CNR) characterized by an activity of 4.27×10^{13} Bq (in date 21 Feb '05) and a dose rate of 1.51 ± 0.22 krad/min (in water); a Perkin-Elmer spectrometer (lambda 45 model) with 2 lamps (deuterium lamp for the UV region and a halogen one for $\lambda > 326$ nm) and a monochromator with 0.1 nm resolution.
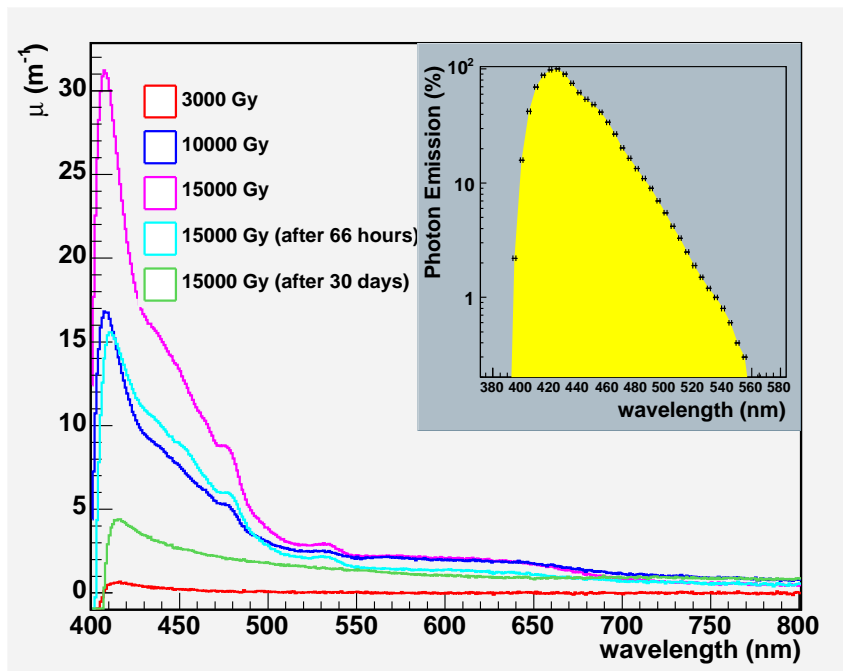
Figure 3.12: Induced absorption coefficient in the wavelenght range 400-800 nm for different absorbed doses. In addition, the recovery after 1.5 Mrad is shown. In the inset, the EJ-200 emission spectrum is included.

First, the optical pad was irradiated at several dose levels up to 15 krad, corresponding to three times the maximum absorbed dose expected in ten years. The optical transmission spectra of the pad in the range 190-1100 nm were measured before and after each irradiation by the spectrometer. The optical pad transmission spectrum convoluted with the scintillator emission spectrum (inset of figure 3.12) does not show any appreciable variations of the integrated light output.

A similar study was performed on light guides. Even though the integrated transmittance spectrum in the scintillator emission region is stable within 5%, it is possible to recognize some small absorption structures. The two most important types of radiation damage in plastic scintillators [74] are the production of new stable absorption centers that decrease the light transmission, and the deterioration of fluor and shifter molecules that reduce the light production. Both effects produce a loss of light output to the exit face. The concentration of colour centres is estimated from optical transmission measurements because it is proportional to the induced absorption coefficient μ defined as follows:

$$\mu = \frac{1}{\mathrm{d}} \ln \left(\frac{T_0}{T} \right) , \tag{3.8}$$

where T_0 and T are the transmission before and after irradiation and d is the sample length in meters. The scintillator sample was irradiated up to 400 krad observing negligi-

ble variation on the transmission spectrum. That dose corresponds to about one hundred times the expected dose for the whole AMS mission. Above this threshold in agreement with literature [75], an absorbing peak at about 410 nm increases as is shown in figure 3.12, where the radiation induced absorption coefficient μ is plotted as a function of the dose. The absorption in the lower wavelength region of the spectrum can be related to a deterioration of the wavelength-shifter molecules. In figure 3.12 the measurements done some hours after the irradiation are also included to appreciate the recovery of the scintillator. A deeper investigation of recovery time of our scintillators is in progress and a study with β sources instead of γ is in preparation using the LINAC electron accelerator of Fossatone di Medicina, Bologna.

3.3.3   Space qualification of LTOF

Space qualification tests are required from NASA to check the detector functionality in normal operating space conditions and to asses that the mission goals will be fulfilled even in the most pessimistic conditions. The fully assembled LTOF flight model detector underwent a thermal vacuum test from 2 May until 10 June 2006 and a vibration test in October 2006 fulfilling succesfully all the requirements. Both tests were performed at SERMS Laboratories, Universitá di Perugia, Polo Scientifico Didattico di Terni (Italy). The Carlo Gavazzi Space planned the TVT temperature profile and was the test conductor, responsible for producing the TVT and TV final conformity report released by the Italian Space Agency (ASI).

The purpose of these tests was to demonstrate the capability of the LTOF detector to operate when exposed to extreme temperatures expected in orbit. In order to check potential functional degradations or malfunctionings, the apparatus behaviour was monitored in Bologna after the complete assembly, in Terni along all TVT phases and after TV test, finally again in Bologna. In addition, the readout counter signals were aquired for an additional detailed off-line analysis. In figure 3.13 is shown the insetion of the LTOF in the TVT chamber of SERMS Laboratories. I was deeply involved in this crucial phase of the LTOF qualification, but detailed description of the test development and results would go beyond the scope of this thesis. They are instead fully covered in Ref. [76].

The LTOF is now ready to be integrated with the other AMS-02 sub-detectors, while the UTOF is undergoing the final assembly phase and its space qualification tests are scheduled for June 2006. The integration at CERN will start in July 2007 for the Lower TOF and in October for the Upper TOF.

Figure 3.13: Pictures of the LTOF during TVT test in Terni documenting its insertion in the SERMS TVT chamber.

Chapter 4

AMS-02 Monte Carlo simulation for (anti)deuterons

In experimental physics, a detailed knowledge of the response function of the detector is fundamental in order to test and tune the particle reconstruction algorithms. The charged Cosmic Rays pattern in the AMS-02 detector is studied through a simulation program based on the GEANT3 package. FLUKA package is used to simulate hadronic interactions [77], whereas nuclear interactions and heavy-ion collisions are simulated by means of RQMD code ([35] and references therein).

The detector geometry is described in detail including mechanical drawings, and additional experimental measurements are also introduced into the simulation code. The particle trajectory along different sub-detectors is divided into small steps, and at each step interactions and energy losses within the matter are randomly generated according to their probability. Physical signals are then converted into the equivalent detector response and the event reconstruction proceeds as it would do for real data. These data are a useful benchmark to study selection criteria for particle identification and to develop analysis strategies to be applied to real data.

GEANT3 and additional packages allow the tracking of deuterons and antideuterons inside AMS-02, simulating ionization energy loss and multiple scattering, but nuclear inelastic interactions are not included for these physics channels. To take into account these processes we introduced into the AMS-02 Monte Carlo code the nuclear models we are going to describe below in this chapter.

4.1   Deuteron inelastic cross section

In the collision of an incident Cosmic Ray with a target nucleus of the detector, nuclear reactions are involved. The inelastic (or reaction) cross section σ_{inel} gives the probability

that a nucleus N_i undergoes a nuclear reaction with another nucleus N_j:

$$N_i + N_j \Rightarrow X \ .$$
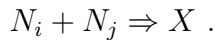
The inelastic cross section is obtained by subtracting the elastic cross section σ_{el} from the total cross section σ_{tot}:

$$\sigma_{\text{inel}} = \sigma_{\text{tot}} - \sigma_{\text{el}} \ ,$$

where σ_{el} represents the probability of scattering:

$$N_i + N_j \Rightarrow N_i + N_j \ .$$
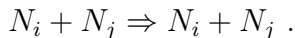
In the simplest approach considering nuclei as hard spheres, the cross section is proportional to the geometrical area of the nucleus (πr_{geom}^2) that scales as $A^{2/3}$, where A is the mass number of the nucleus.

In 1950, Bradt and Peters[78] proposed a first order correction to take into account the wavefunction overlap of the two nuclei, a projectile N_P and a target N_T:

$$\begin{aligned} r_{\text{eff}} &= r_{\text{geom}} - \Delta r \ , \\ \sigma_{\text{inel}} &= \pi (r_P + r_T - \Delta r)^2 \ . \end{aligned}$$

Actually most of the semiempirical models approximate the inelastic cross sections as:

$$\sigma_{\text{inel}} = \pi r_0 (A_P^{1/3} + A_T^{1/3} - \delta_0)^2 \ ,$$

where r_0 is the nucleon radius, δ_0 is the overlap parameter or *trasparency*, that could be a constant or an energy dependent parameter, and A_P and A_T are the projectile and target mass numbers, respectively. This form of parameterization works nicely for high energies, but for charged ions, as the energy decreases, the Coulomb interaction becomes important and changes the reaction cross section significantly.

The parameterization with the best fit to most measurements of nucleus-nucleus inelastic cross section is currently the universal parameterization proposed by Tripathi and coworkers[79]. This model provides a unified, consistent and accurate picture of the reaction cross section for any colliding system of nuclei (n+N_j, p+N_j, N_i+N_j) for a wide energy range. According to that model:

$$\sigma_{\text{inel}} = \pi r_0^2 (A_P^{1/3} + A_T^{1/3} + \delta_E)^2 (1 - R_c \frac{B}{E_{\text{cm}}}) X_m \ , \qquad (4.1)$$

where r_0=1.1 fm, E_{cm} in the colliding system center of mass kinetic energy in MeV and E is the projectile kinetic energy in MeV/nucl.

The second last term is the Coulomb interaction, which modifies the cross section at low energies and becomes less important as the energy increases. Actually if the energy of the system is quite below its Coulomb potential, the projectile particle will not be able

to penetrate and, as a consequence, nuclear reactions will not be likely to happen. The Coulomb interaction barrier parameter B depends on energy and is given by:

$$B = \frac{1.44 Z_P Z_T}{R} \ ,$$

where Z_P and Z_T are atomic numbers of the projectile and target, and R is the radius for evaluating the Coulomb barrier height:

$$R = r_P + r_T + \frac{1.2 \ (A_T^{1/3} + A_P^{1/3})}{E_{\mathrm{cm}}^{1/3}} \ .$$

The parameter r_i is the equivalent hard sphere radius and it is related to the $r_{\mathrm{rms},i}$ as described in [80]:

$$r_i = 1.29 \ r_{\mathrm{rms},i} \ .$$

The energy dependence of the reaction cross section at intermediate and high energies is mainly caused by two effects: transparency and Pauli blocking. This is taken into account in the δ_E term:

$$\delta_{\mathrm{E}} = 1.85 S + \frac{0.16 \ S}{E_{\mathrm{cm}}^{1/3}} - C_E + \frac{0.91 \ (A_T - 2 Z_T) \ Z_P}{A_T A_P} \ ,$$

where:

- S is the mass asymmetry term, related to the volume overlap of the collision system, and defined as:

$$S = \frac{A_P^{1/3} A_T^{1/3}}{A_P^{1/3} + A_T^{1/3}} \ .$$

- C_E accounts for the trasparency and Pauli blocking and is given by:

$$C_E = D \left[1 - \exp \left(-\frac{E}{T_1} \right) \right] - 2.292 \ \exp \left(-\frac{E}{792} \right) \ \cos \ (0.229 \ E^{0.453}) \ ,$$

where D could be nicely connected to the density of the colliding system for medium and heavier systems and simulates the effects of Pauli blocking. In the case of deuteron being a projectile particle, the best value for D and T_1 parameters are:

$$
\begin{aligned}
T_1 &= 23 \ , \\
D &= 1.65 + \frac{0.1}{1 + \exp \left[(500 - E)/200 \right]} \ .
\end{aligned}
$$

For neutron-nucleus interaction there is no Coulomb interaction, but the cross section is modified from the imaginary part of the optical potential. This effect is taken into account in the last term X_m of eq. 4.1, whereas X_m is equal to one for the other reactions. For example, the inelastic cross sections obtained in the case of deuteron-proton and deuteron-Carbon interacting systems are shown in figure 4.1(a) and figure 4.1(b) respectively.

(a)   (b)
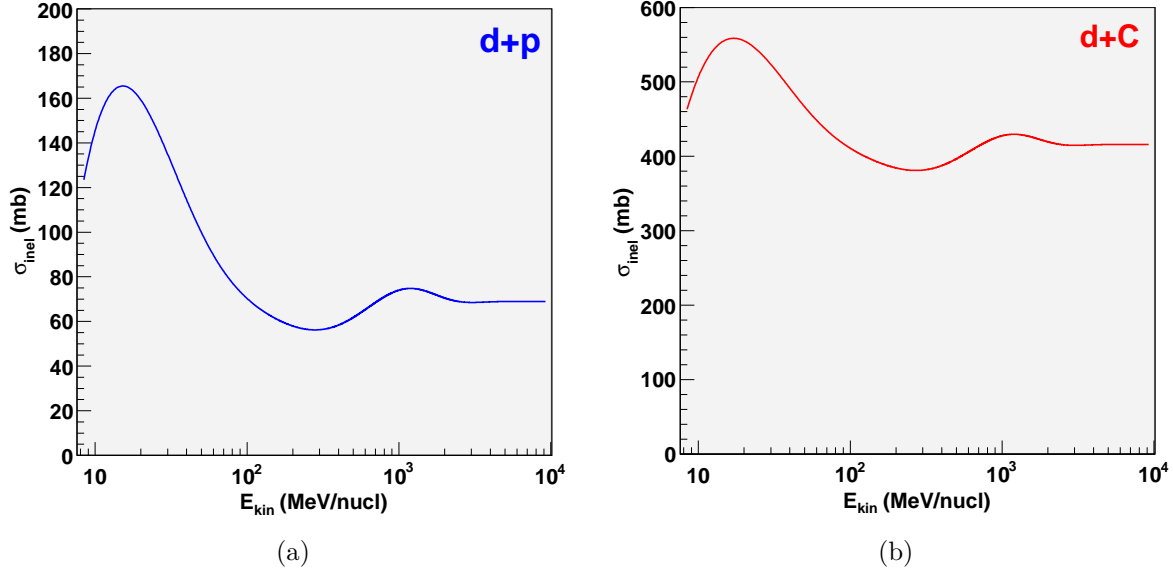
Figure 4.1: (a)Inelastic cross section obtained from Tripathi formula for deuteron-proton system, and (b) for deuteron-Carbon system.

4.2 Antideuteron inelastic cross section

To study the behaviour of incident antideuterons through the detector, an estimation of $\sigma_{\text{inel}}(\bar{\text{d}}, N_j)$ is necessary in order to take into account nuclear interactions. So far only few experimental data on antideuterons are available [81, 82, 83], so we are forced to build on a model.

At high energies the antideuteron inelastic cross section could be approximate to a constant with the general dependence on the target nucleus area[81, 14]:

$$\sigma_{\text{inel}}(\bar{\text{d}}, N_j) = 105 \ A^{2/3} \text{mb} . \tag{4.2}$$

But antideuterons at low kinetic energy (0.2–1.2 GeV/nucl) play a crucial role in searching for indirect Dark Matter. In particular in this range their inelastic cross section is expected to change a lot and therefore, according to our intent, this approximation is not accurate enough.

A possible solution can be found thanks to the CPT invariance of nuclear force, that has been experimentally checked for the $\bar{\text{p}}$d and $\bar{\text{d}}$p systems[82]. Assuming that the $\bar{\text{p}}$d cross section is the same as the $\bar{\text{d}}$p cross section at the same centre of mass energy:

$$\sigma(\bar{\text{p}}, \text{d}) = \sigma(\bar{\text{d}}, \text{p}) , \tag{4.3}$$

for a general nucleus N_j with atomic number A, using the relation of the equation 4.2,
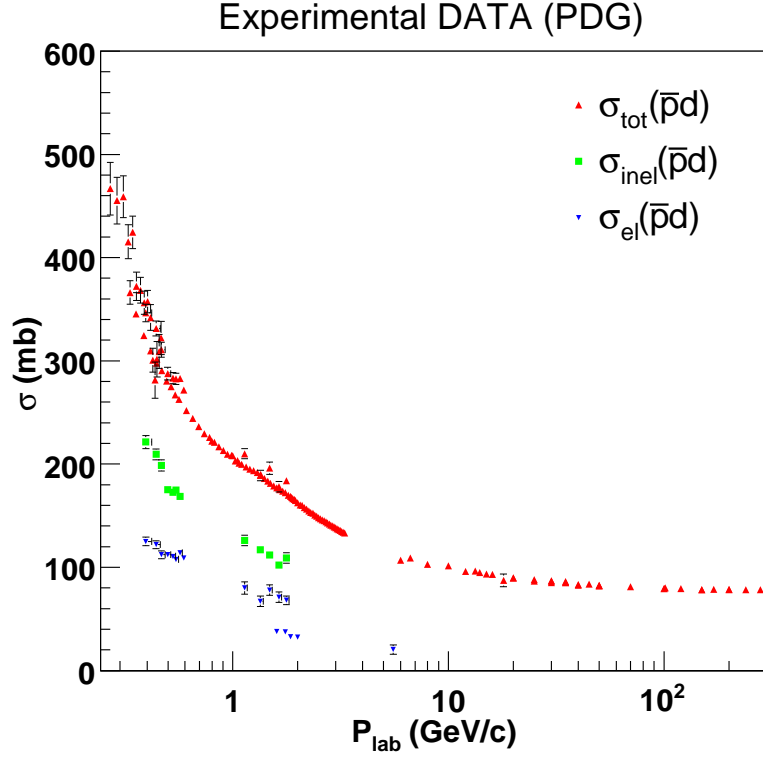
Figure 4.2: Experimental available data of total, inelastic and elastic cross section for antiproton-deuteron system [2, 84, 85, 86, 87, 88].

we obtain:

$$\sigma(\bar{d}, N_j) = \sigma(\bar{p}, d)A^{2/3} \ . \tag{4.4}$$

A good deal of experimental data is measured for $\bar{p}d$ total cross section [1], a lower statistic is available for elastic and inelastic cross section as is shown in figure 4.2, where all the present data are plotted with the relative experimental uncertainties.

The Tripathi parameterization was modified in order to be valid for antinuclei. Clearly the term related to Coulomb interaction is now positive and it produces a change in the shape of the cross section at very low energy. Due to their opposite electric charge nuclei attract each other increasing the probability of interacting. The phenomenon is particulary strong when the incident particle is slow. Also the Pauli blocking effect is removed in this case, because it is not supposed to influence the interaction. In addition the parameters regulating the trasparency are tuned *ad hoc* in order to fit real data up to a kinetic energy of 10 GeV. Above this energy a hyperbolic function is used both to mimic the total cross section of real data at a higher energy and to join the previous inelastic

---

[1] http://pdg.lbl.gov/2006/reviews/contents_sports.html
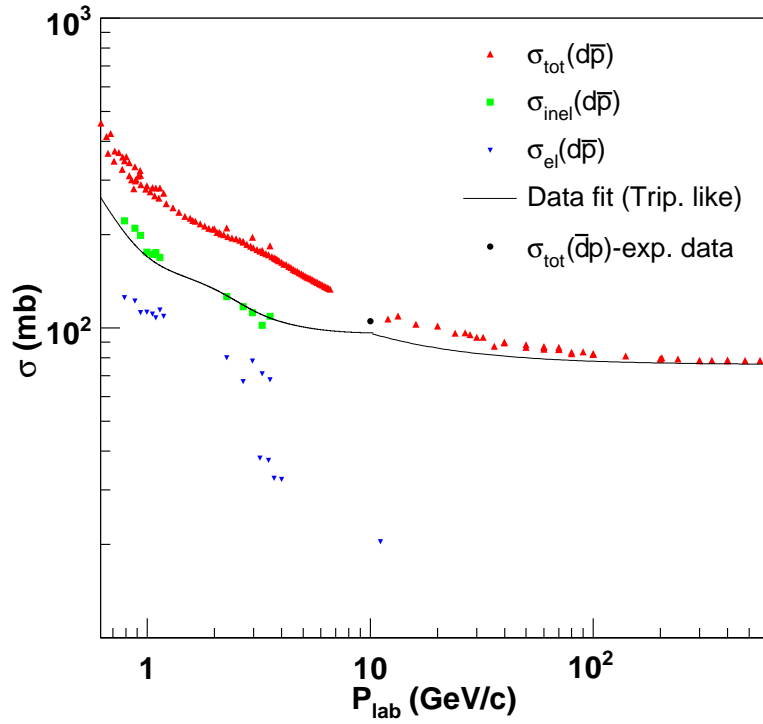
Figure 4.3: Experimental points are the same of figure 4.2, but considering deuteron as incident particle. The black curve is derived as descibed in the text.

cross section fit at 10 GeV. Indeed at high energy the cross section could be considered entirely inelastic. Finally the asimptotic inelastic cross section value is set at 76.5 mb. The complete curve introduced to reproduce the expected inelastic andideuteron-proton cross section is superimposed in figure 4.3.

4.3   Event generation

4.3.1   Generation volume

A representative sample of the Cosmic rays flux impinging on AMS-02 has to be simulated. The event generation strategy is to enclose the detector in an imaginary concentric cube of 3.9 m side. Events are generated as they come from a random point on one cube face with isotropic coverage of AMS-02 detector. To gain simulation efficiency it is possible to choose to produce a data sample containing events impinging the detector only from the top plane.

The AMS-02 geometrical acceptance [89] can be easily computed in the assumption

of isotropic flux intensity and is given by:

$$A_{\mathrm{AMS}}(E) = A_0 \times \frac{N_{\mathrm{acc}}}{N_{\mathrm{gen}}} \ . \tag{4.5}$$

A_0 is the geometrical factor for the planar aperture where the events are randomly generated. For one side of the cube this factor is expressed by:

$$A_0 = \int_\Omega \mathrm{d}\omega \int_S \mathrm{d}\sigma \, \hat{\mathbf{r}} = \int_\Omega \int_S \cos\theta \, \mathrm{d}\sigma \, \mathrm{d}\omega \ , \tag{4.6}$$

where $\mathrm{d}\sigma$ is the element of surface area S, $\mathrm{d}\omega = \mathrm{d}\phi \, \mathrm{d}\cos\theta$ is the element of solid angle Ω, with θ and ϕ polar and azimuth angle respectively.
Hence:

$$A_0 = 2\pi S \int_0^1 \cos\theta \, \mathrm{d}\cos\theta = \pi S \ . \tag{4.7}$$

The geometrical factor in this case is therefore equal to $\pi l^2 = 47.78 \ m^2 sr$.

4.3.2 CR simulated spectrum

To evaluate the AMS-02 detector performance the Monte Carlo code is able to simulate events according to cosmic ray power-law energy spectra or could be set in order to reproduce also sea level muons and undercutoff spectrum[90]. As a consequence of the typical power-law energy spectrum of cosmic rays, to simulate enough statistic in the highest part of the spectrum we obtain a corresponding sample at low energy which is several orders of magnitude bigger. To optimize the MC production, particles are generated following a uniform distribution in the momentum logarithm and they are generated separately in three momentum ranges: 0.5–10 GeV, 10–200 GeV and high 200–1789 GeV.

4.3.3 Fast trigger and LVL1 logics

When a particle enters the AMS-02 acceptance, fast sub-detectors, namely TOF and ECAL, are invoked to provide the fast trigger signal and if some LVL1 conditions are fulfilled the event could be stored. Also the trigger logic could be studied by means of MC simulation and different requirements could be set and implemented. For the purposes of this thesis, the used MC data are produced requiring very loose trigger criteria in order to deal with an unbiased sample. In particular both the MC event leaving a signal compatible with $Z \geq 1$ particle on at least three TOF planes out of four and events with a significant energy deposition in the ECAL are saved. The trigger issue is quite complex and a detailed description would go beyond the scope of this thesis. A simplified description of the fast trigger as well as LVL1 logic adopted for AMS-02 is reported below.

LVL1 Trigger	Selected species
TOF Z1 & VETO=0	p, p̄, d ...
TOF Z2	He, Heavy ions
TOF Z1 & Ecal activity	$e^{\pm}$
Ecal shower shape	γ

Table 4.1: Some examples of LVL1 trigger conditions will be used to select different physics channels, as explained in the text.

Three hints are given in input to fast trigger logic: TOF $Z1$, TOF $Z2$ and ECAL activity flag. All the PMT outputs of each TOF counter side are combined in OR to form an LT or HT signal, according to the threshold that has been passed. Indeed in the TOF readout electronics both a low and a high threshold (LT and HT respectively) are implemented for every PMT signal. Then the signal originated from one plane side is matched in OR (or AND if choosen) with one coming from the other side. The coincidence of three TOF planes out of four enables TOF $Z1$ signal or $Z2$. TOF $Z1$ signal corresponds to the transit of a particle compatible with $Z \geq 1$, passing the low threshold, whereas TOF $Z2$ is related to higher Z ions with $Z \geq 2$, passing the high threshold. Also the ECAL response is included in fast trigger, and an ECAL activity flag is enabled if the conditions on a defined function of the hit cells multiplicity in different layers are fulfilled. The fast trigger signal comes out from the OR of TOF $Z1$, TOF $Z2$ and ECAL activity or from a mask of them.

Fast trigger signal and Anti Coincidence Counter information could be matched to form LVL1 trigger, that should enable data acquisition with high efficiency and low dependence from energy and CR species. The LVL1 trigger rate should not exceed two kHz in order to keep the dead time long enough to wait for the slowest members of the readout system. For this reason no fired ACC is required by trigger logic, if the acquisition rate has to be reduced, as could happen when $Z \geq 1$ particles are selected because of the large abundance of protons in CRs (as reported in table 4.1). As learnt from the AMS-01 experience, this requirement could introduce some biases on trigger efficiency both depending on energy and on ion charge; this effect is particularly important for heavy ions. In addition to that, the requirement of no fired ACC could cause biases because of the presence of the ECAL in AMS-02. Actually eletromagnetic particles can produce back splash particles interacting with the ECAL, but luckily this effect does not always spoil the beta reconstruction. So, by removing ACC from the trigger, it is possible to save a non negligible number of electromagnetic events with good velocity measurement. Whereas for barions, this effect is not essential[91]. To conclude, the Anti Coincidence Counters veto is released when a typical EM particle is recognized in ECAL, and high Z particles are selected, as stated in table 4.1. The AMS-02 flexible trigger logic allows for the optimization of a search for a specific physics channel according to the survey strategy.

Chapter 5

AMS-02 Sensitivity to antideuterons

The goal of this analysis is to make an estimation of the sensitivity of the AMS-02 experiment to the antideuteron flux in Cosmic Rays. The antideuteron signal is very suppressed in CRs and its detection is a challenging task even for a large acceptance space detector like AMS-02. So far, antideuterons have never been found in CRs.

Since this analysis is performed on Monte Carlo data, it is important to assess reasonable selection criteria that are minimally dependent on MC. At the same time, cuts have to be quite elaborated to maximize such a faint signal acceptance and conversely minimize the background in order to select a clean sample.

The measurement of the particle velocity is provided by the TOF detector in the low energy region, where the exotic primary $\overline{\text{d}}$ component is expected, and by the RICH detector at higher energies. A good understanding of the TOF performance is therefore crucial in the search for primary antideuterons with AMS-02. The RICH detector will instead explore the region where the secondary flux is predicted.

5.1   Signal and background

As shown in figure 5.1, the secondary antideuteron signal is expected to be 10^{-11} orders of magnitude lower than that of protons, the most abundant CR species. Although protons have opposite charge signs, they can contaminate $\overline{\text{d}}$ search: because of their huge flux, a very small probability to badly reconstruct their charge sign and mass can produce a sizeable number of fake candidates. A direct MC estimation would require a huge amount of protons and therefore is not possible at the present time. An indirect estimation has been performed and presented in § 5.4.1. Similarly, the signal contamination due to deuterons, whose flux is expected to be about 2% of proton sample, has been evaluated.

Another source of background is represented by electrons, which have the same $\overline{\text{d}}$ charge and can mimic $\overline{\text{d}}$ signal because of their greater abundance. Their rejection is based on the velocity measurement, thanks to the much lower electron mass compared to that of antideuterons. In addition, one can take advantage of the TRD electron/hadron
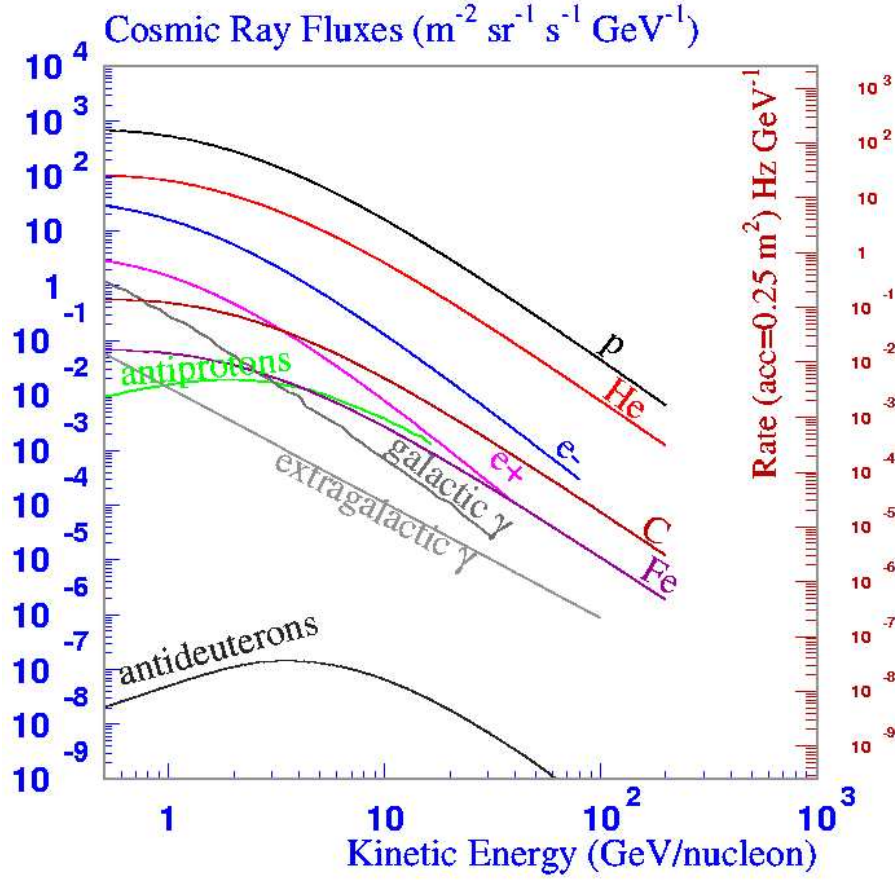
Figure 5.1: Cosmic Ray flux for different components.

separation power, which is essential to reach the required suppression of the level of $10^8 - 10^9$.

Finally, the antiproton background has to be taken into account, because they have the same momentum sign of antideuterons and so they could be rejected by mass measurement only. Due to the big $\overline{p}/\overline{d}$ flux ratio and finite velocity resolution, some $\overline{p}$ are expected to mimic $\overline{d}$. Tight quality cuts on velocity reconstruction are therefore required.

The available Monte Carlo data samples for different particles species used for this study are listed in table 5.1.

CR species	LVL1 statistics	Energy (GeV)
Protons	$\approx 1 \times 10^8$	0.5-200
Electrons	$\approx 4 \times 10^7$	0.5-200
Deuterons	$\approx 4 \times 10^6$	0.5-20
Antideuterons	$\approx 7 \times 10^6$	0.5-20

Table 5.1: The used simulated events were generated as coming from the upper face of an imaginary cube of side 3.9 m which contains the AMS-02 detector, and they follow a uniform distribution in momentum logarithm, as described in chapter 4.3.

5.2 AMS-02 geometrical acceptance

5.2.1 Preselection criteria

The LVL1 criteria demanded on the simulated events are minimal, in order to avoid possible biases for the different incoming particle types as discussed in § 4.3.3. Therefore, in order to deal with a smaller and cleaner sample, the first step of the analysis is to select a subset of data, called preselected sample, whose events satisfy the following basic conditions, defyining the AMS-Normal Particle:

- at least one reconstructed track in the Tracker, which implies that a rigidity measurement is provided;

- at least one reconstructed track in the TRD, which performs particle identification at high energy;

- a velocity measurement compatible with a downgoing particle ($\beta > 0$);

- the reconstructed charge is $|Z| = 1$.

Accidental coincidences of CR events or interactions in the detector structure could produce events with more than one associated particle, which are excluded requiring only events with one associated Normal AMS-Particle.

5.2.2 Geometrical acceptance for (anti)deuterons

The AMS-02 geometrical acceptance after preselection criteria is estimated for deuterons and antideuterons using the MC sample generated according to the new inputs for the inelastic cross section described in the previous chapter. In the two plots of figure 5.2 the computed geometrical acceptance is shown for d and $\overline{\text{d}}$. As already observed, the inelastic cross section for an anti-particle has a different shape with respect to the corresponding particle, particularly at low energies where annihilation processes dominate. So the greater
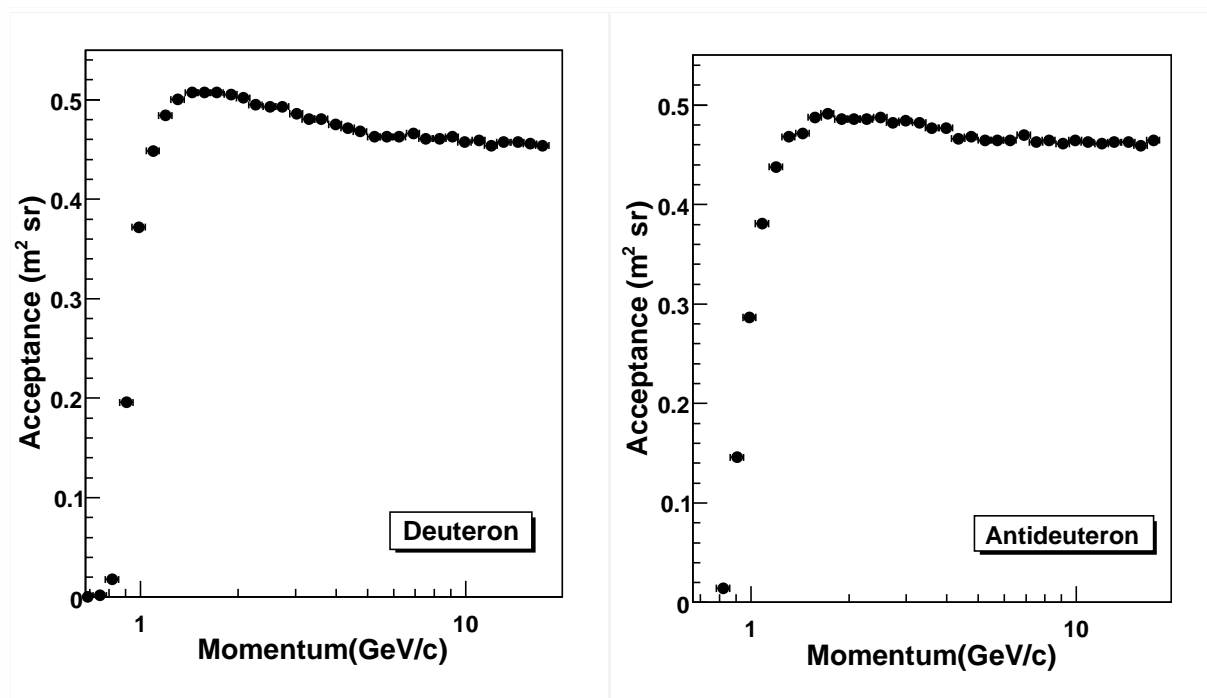
Figure 5.2: AMS-02 geometrical acceptance for deuteron (left) and antideuteron (right) determined from the preselected sample.

probability for $\overline{\mathrm{d}}$s to undergo inelastic interactions, increase their attenuation in crossing the detector matter. This effect results in a smaller geometrical acceptance for $\overline{\mathrm{d}}$ with respect to d, as it is shown in the plot of their ratio in figure 5.3. The correction factor so derived will be applied to deuteron final acceptance, to estimate the antideuteron one after the application of all the analysis cuts.

5.3   Event selection

In order to select a clean sample of antideuterons, we have to reject mis-reconstructed background particles making use of all subdetectors. In this section, some meaningful selection criteria will be presented among them which are applied in this analysis to suppress events spoiled by interactions inside the detector, to optimize rigidity reconstruction in the Tracker, to improve velocity measurement in the TOF and in the RICH according to the momentum range and to reject electrons.

5.3.1   Suppression of events with interactions

When a particle passes through the AMS-02 detector, some interactions could occur producing secondary particles, which can be partially measured by the subsequent subdetec-

Deuteron/AntiDeuteron Acceptance Ratio
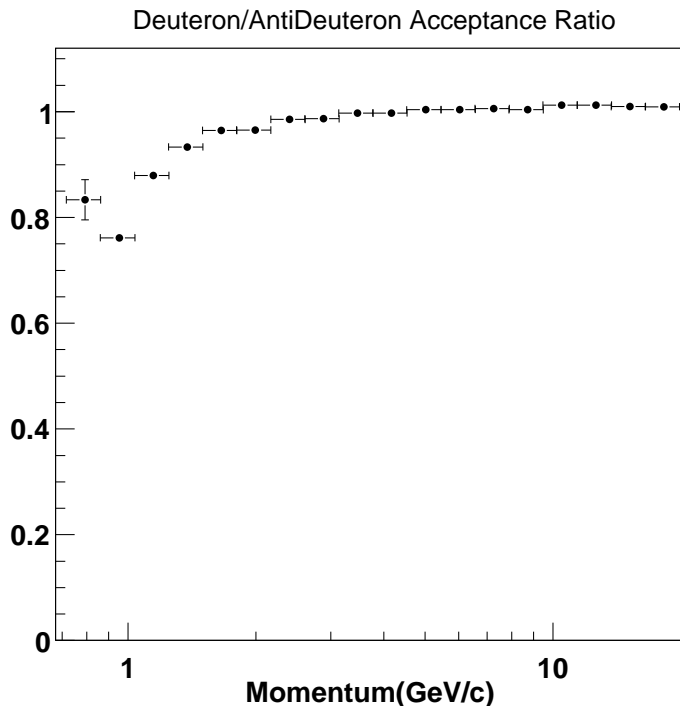
Figure 5.3: Correction factor for d with respects to $\overline{\mathrm{d}}$ for the AMS-02 geometrical acceptance as a function of the particle generated momentum.

tors spoiling the event reconstruction. To prevent this, events with a suspicious pattern compatible with an interaction have to be rejected. The main cuts implemented in the present analysis to reduce this effect are described below.

As underlined in chapter 4.3.3, the ACC signal is not included as standard veto in the first-level trigger logics. To eliminate events suffering from interactions, which produce secondaries at a large angle or deviate their track enough to hit ACC cylindrical area, we require:

- a number of Anti Cluster < 1 in case of no ECAL activity and < 2 otherwise.

A TOF counter is considered hit and a TOF-Cluster object is filled up when the signals coming from both sides of the same paddle overcome a fixed threshold, confirming the particle transit. If two adjacent paddles are hit, only one TOF-Cluster is built, with an associated trasversal coordinate corresponding to the overlapping of the two counters. The particle β is reconstructed using one TOF-Cluster per each fired TOF plane (at most four planes out of four). Additional counters not involved in β measurement could flag the presence of secondaries particles produced inside the detector. In order to reject these events we require:

- a number of unused TOF-Cluster = 0 .
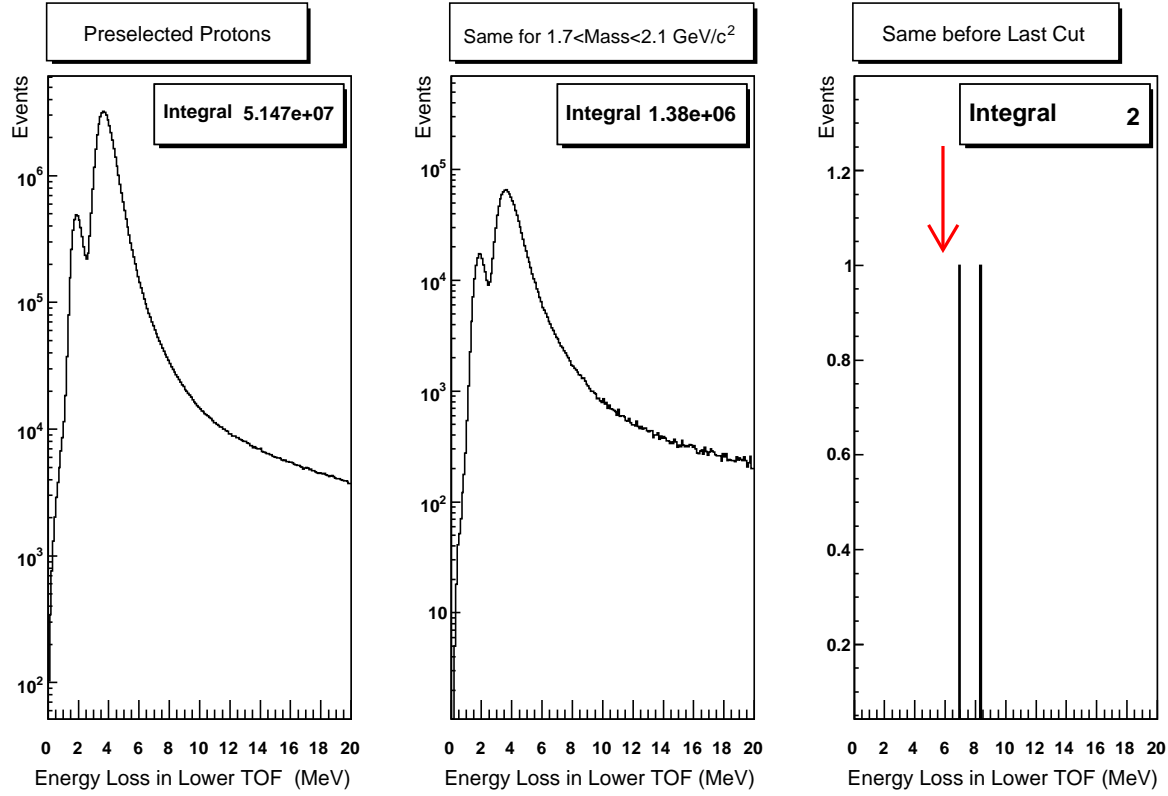
Figure 5.4: Left: distribution of the total energy lost in the Lower TOF by the preselected proton sample; center: the same as the previous plot, but for the preselected protons, which enter in the d ($\overline{\text{d}}$) mass window and therefore would potentially mimic $\overline{\text{d}}$; right: the same as the previous plot, but for events surviving all cuts except this one. The limit on the sum of the energy lost in the Lower TOF is set at 6 MeV, as indicated by the arrow.

In the case an interaction occurs in the proximity of a TOF plane, low energy particles could be produced locally and the energy released in the counter itself should be more than what is expected for the primary particle. The energy loss in one TOF counter for a vertical track due to a minimum ionizing particle (MIP) with charge $Z = 1$ is around 2 MeV and its dependence on β is described in § 3.2.2. The events for which:

- the sum of energy lost in the Upper TOF or in the Lower TOF is greater than 6 MeV,

are removed.

The distribution of the sum of energy lost in the Lower TOF by protons is presented in figure 5.4. The proton sample is chosen because of its greater availability in MC, but it is important to remark that these criteria, introduced to reject events spoiled by interactions,
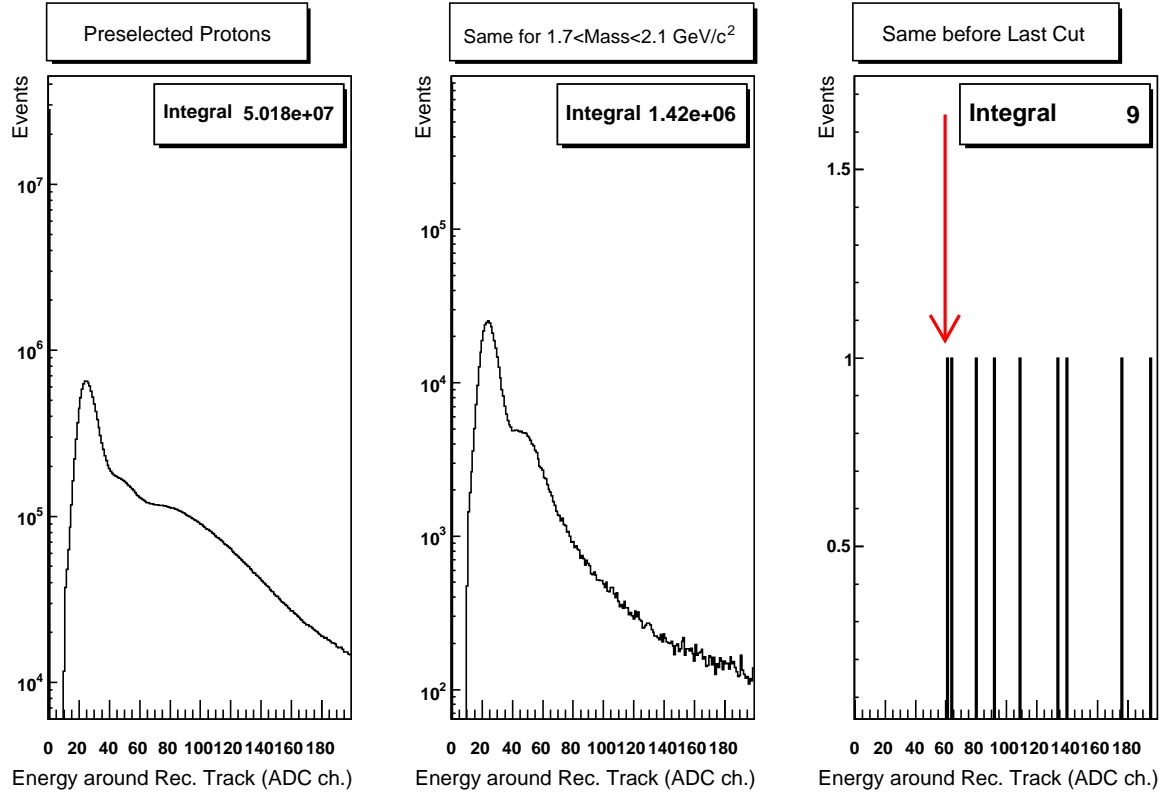
Figure 5.5: Distribution of the energy loss around the reconstructed track in the Tracker for the preselected proton sample (left plot). The effect of this cut on the surviving sample of bad events in shown in the right plot. The cut is applied accordingly to the red arrow.

have the same purpose for all kinds of CR species. In order to better appreciate the power of each cut, it is necessary to disentangle its proper effect from that of all the others. For this reason, all the cuts, which are displayed in figures throughout this chapter, will be presented with the same pattern: on the left plot the distribution of the chosen physical quantity for the preselected sample; in the central plot the same quantity for preselected events that without any additional cuts will mimic antideuteron signal (*bad* events), being reconstructed with the d ($\overline{\text{d}}$) typical mass ($1.7 < \text{Mass} < 2.1 \text{ GeV/c}^2$); in the last plot on the right the same distribution of the central plot is shown, but only for the events surviving all the cuts except that one under study.

Secondary production in the proximity of one of the Tracker planes could be recognized by an increase in the number of hits. The sum of Tracker hit amplitudes found in the vicinity of the reconstructed track is a sensitive indicator for this kind of process, hence we require to this quantity:

- to be below 60 ADC channel.

Figure 5.5 shows the distribution of this quantity for the preselected sample of protons, for preselected protons reconstructed as antideuterons and, in the last plot on the right, the power of this cut set at 60 ADC channels to reject badly measured events, which survive all the other cuts implemented in this analysis.

With the same goal a limit is set on the number of reconstructed TRD segments, which are sub TRD-tracks produced in sections of the detector. Considering the TRD detector formed by four main sections along the z axis, the TRD-track for a single particle would be formed at most by four segments, whereas a number of segments greater than four is probably connected to secondaries production. Hence we require that:

- the number of reconstructed TRD segments is at most 4.

5.3.2 Tracker quality cuts

The Tracker detector plays a critical role in the particle identification through both the reconstruction of the correct particle momentum and the determination of its electric charge sign. Indeed in the magnetic field, the sign of the particle charge decides the bending direction of its track.

Particles with a positive charge like protons and deuterons are also a source of background for the antideuteron signal, because of the finite space resolution of the Tracker detector and of possible deflections in the particle trajectory due to Coulomb scattering. At low energy, even if the particle curvature radius is big, the effect of the multiple scattering could not only bend its direction affecting the rigidity reconstruction, but also confuse its charge sign. Whereas, as soon as the particle momentum increases, its trajectory is bended less and less in the magnetic field and therefore the probability of mixing up a positive particle becomes increasingly higher. In addition, all particle species crossing the detector could undergo deviations along their path which spoil rigidity measurement. To maximize the AMS-02 rejection power in particular for abundant CR components like p and d, an improved rigidity measurement is necessary and therefore some quality cuts have to be applied to Tracker.

Possible ambiguities or discrepancies in the results of the track finding methods are important to point out this kind of bad events. A way that could be used to recognize a track kink is to measure independently the radius of the trajectory in the upper and lthe ower part of the Tracker. Actually, it is possible to reconstruct two sub-tracks, each one containing the half of hits forming the complete one. For good events, upper and lower rigidities (R_{1st} and R_{2nd}) are expected to be compatible within fluctuations. Indeed a scattering deviation or the presence of a spurius hit are expected to strongly affect just one of them. Hence:

- large discrepancies between normal rigidity and R_{1st} or R_{2nd} are not accepted.

The first step in the reconstruction of the particle rigidity is the Tracker Cluster formation. Along the bending side S, for a given ladder a cluster is made up of the

adjacent strips, which have the ratio signal over noise greater than a fixed threshold. The same thing is done for the non bending side K (but with a lower threshold). After that, in each plane all possible S(y) and K(x) hits belonging to the same ladder are combined into 3-D hits. Due to the peculiarity of the K cluster of having one readout channel corresponding to 6 or 8 geographical positions equally spaced, a single S–K cluster pair creates 6–8 3-D hits. Usually the track finding algorithm is applied to at least four 3-D hits (coreponding to four Tracker planes). But since K strips have a low S/N ratio, often only three 3-D hits are found and therefore a *False* K hit is created accordingly to the predictions obtained from the track. *False TOF* K clusters are always provided in all ladders, extrapolated from the position of the available TOF clusters, and so an additional rigidity called R_{TOF} is available. When sometimes no track with even three 3-D hits is found, then R_{TOF}, reconstructed as described above, becomes important being the only available rigidity measurement.

Three different methods are used to reconstruct rigidity, namely *fast*, based on 5×5 matrix inversion, *Kalman* based on the Kalman filter using the GEANE CERN Library program [92] and *path integral* by J.Alcaraz [93]. In order to avoid select only well reconstructed events :

- rigidity measurements obtained by Fast algorithm, Path Integral algorithm and R_{TOF} are required to be compatible.

The rejection power for p and d, that can be reached applying these cuts is shown in chapter 5.4.1.

5.3.3   Antiproton background: TOF based selection

Antiprotons have the same electric charge sign and value as antideuterons, therefore a very reliable measurement of particle velocity is fundamental to correctly reconstruct its mass and disentangle the two samples. The $\overline{\mathrm{p}}/\overline{\mathrm{d}}$ contamination is considered instead of the $\overline{\mathrm{p}}/\overline{\mathrm{d}}$ one, just for practical reasons (larger MC statistics for protons).

At low momenta, β is reconstructed using the time measurements provided by TOF clusters, found in the vicinity of Tracker Track, with the assumption of constant particle speed. Each couple of planes where one Cluster, confirmed by Tracker, is found, gives a β measurement. To have the greatest redundancy and so far as possible a realiable velocity measurement, the number of TOF layers used in β reconstruction is required to be equal to four, providing four β measurements. In addition to that, a reasonable upper threshold on the χ^2 resulting from beta fit is required.

Conventionally, a positive velocity is associated with down-going particles, whereas a nagative one is associated with up-going particles. The speed of light is the upper limit for all existing particles, but $1/\beta$, proportional to the time measured by the TOF system, has a Gaussian distribution and therefore statistical flactuations could result in a β value
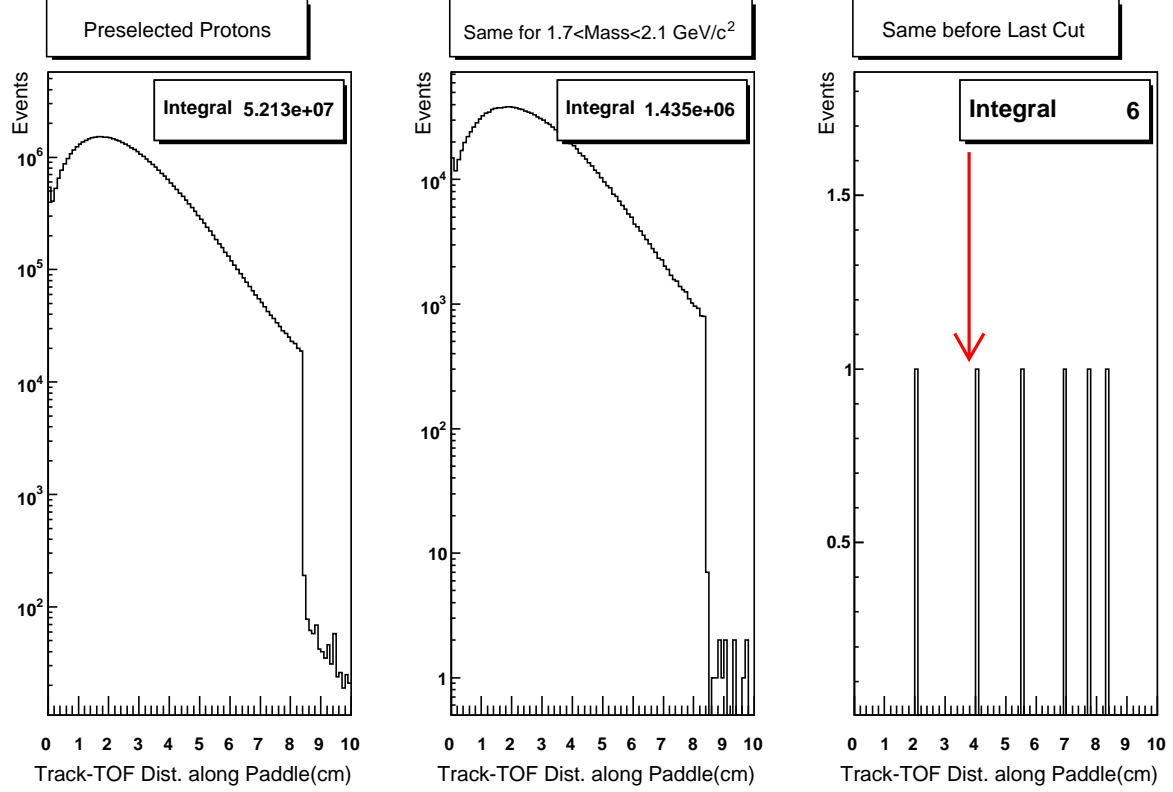
Figure 5.6: Distribution of the distance between the reconstructed position along the paddle for TOF used Clusters (plane one and four) and the coordinate derived extrapolating the Tracker reconstructed track to the examined TOF ladder for the preselected proton sample (left plot). The cut is set at 3.9 cm according to the red arrow in the right figure where the surviving bad events are plotted. The application of the cut for plane two and three (y coordinate) will suppress the remaining event. The proton sample is used instead of the antiproton one, but requiring positive momentum.

being greater than one. In the case of $1/\beta < 1$ a new β' is defined:

$$1/\beta' = 2 - 1/\beta \ , \tag{5.1}$$

and the resulting mass is redefined accordingly, whereas a negative sign is added to mark whether the transformation has occurred. The sense of this substitution is to make able to estimate the particle β from the tails of the TOF time distribution, and at the same time have $\beta < 1$ as physical limit.

It is possible to derive the position of the particle crossing point along the TOF paddle by the difference between the two sides signals with an uncertainty of about 3-4 cm for rectangular counters. To check consistency between TOF and Tracker, the maximum
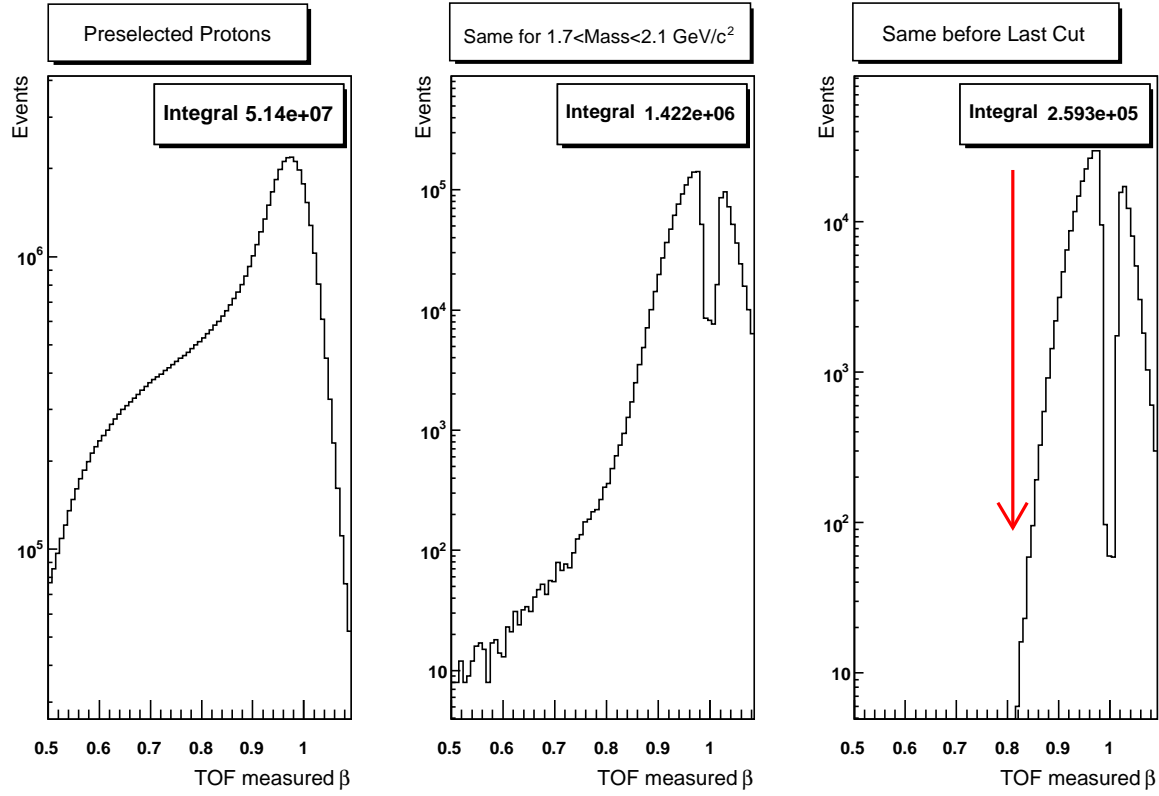
Figure 5.7: Distribution of the velocity measured by the TOF for the proton sample. Events passing all cuts have a quite Gaussian distribution around $\beta = 1$ and so can be removed requiring $\beta < 0.815$.

allowed distance between the reconstructed position of each used TOF Cluster along the paddle and the Tracker track extrapoleted to the considered TOF paddle is set at 3.9 cm for plane one and four (x bending direction) and it is set at 5 cm for plane two and three. The distribution of the distance, as defined above, along x for the proton sample is illustrated in figure 5.6. For brevity the application of the cut along y is not shown, but it will remove the unique event passing this threshold along x.

The distribution of particle velocity reconstructed by the TOF, for the surviving protons passing all cuts, seems to be quite Gaussian. No proton events (antiproton) are reconstructed in the mass window of deuterons (antideuterons) if the upper limit for the maximum velocity measured by TOF is set at:

$$\beta_{\text{TOF}} < 0.815 \ , \tag{5.2}$$

as shown in figure 5.7.
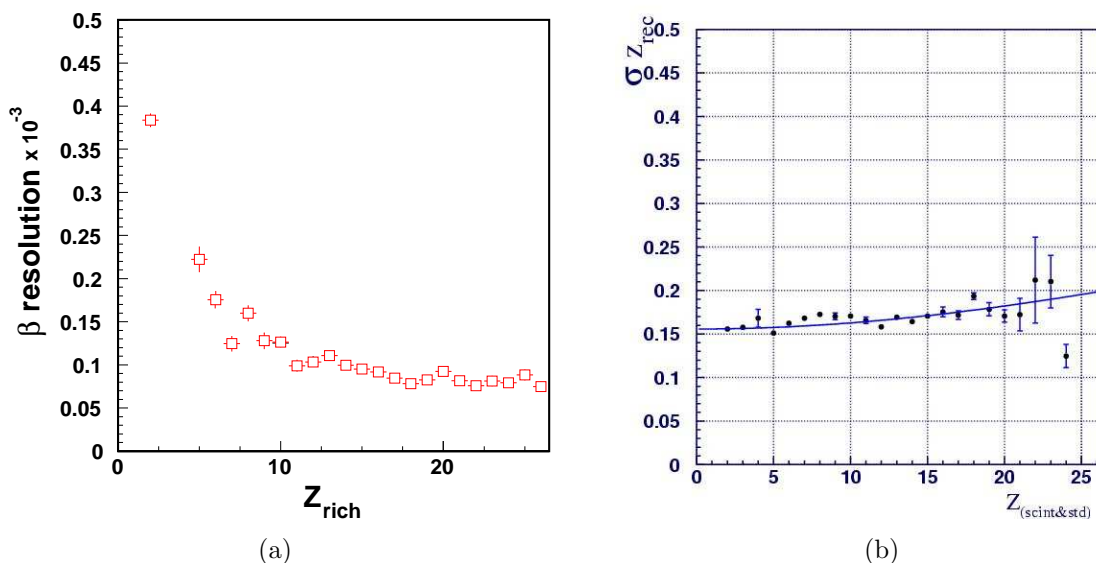
Figure 5.8: (a) RICH β resolution as a function of the ion charge Z and (b) RICH charge resolution for ions up to Fe ($Z = 26$) measured by the RICH prototype during the 2003 beam test[45].

5.3.4   Antiproton background: RICH based selection

Above the TOF momentum range, particle velocity is reconstructed by means of the RICH detector, which has a higher resolution but a smaller acceptance. In the interesting momentum region (1-3 GeV/c per nucleon) covered only by a Sodium Fluoride radiator, the velocity reconstruction is possible but with very low efficiency. As a matter of fact, Rayleigh scattering spoils the RICH β resolution and this effect is particularly relevant for Sodium Fluoride radiators, reducing the proton/deuteron rejection power of the detector to a level of 10^{-4}, which is insufficient for this analysis. The operating range of the Aerogel radiator starts from velocity $0.952c$, corresponding to a momentum of about 3 Gev/c per nucleon, and it extends up to the plateau placed at about 10 GeV/c, as was shown in figure 2.10(b).

The velocity of the incoming particles is determined using a two-step reconstruction algoritm [45, 47]. Firstly, knowing the particle track, a velocity is associated with each hit, except for those produced by the particle itself and not by Cherenkov light, called *hot spots*. Secondly, the hits are grouped in clusters and the most probable cluster gives the final velocity. The algorithm used to measure the absolute value of the particle charge [45, 47] is based on the estimator $Z_{\mathrm{meas}} = \sqrt{N_{\mathrm{ring}}/N_{\mathrm{exp}}}$, where N_{ring} is the number of photoelectrons detected in the ring and N_{exp} is the number of expected photoelectrons for an equivalent (same velocity and same track parameters) $Z = 1$ particle. The β
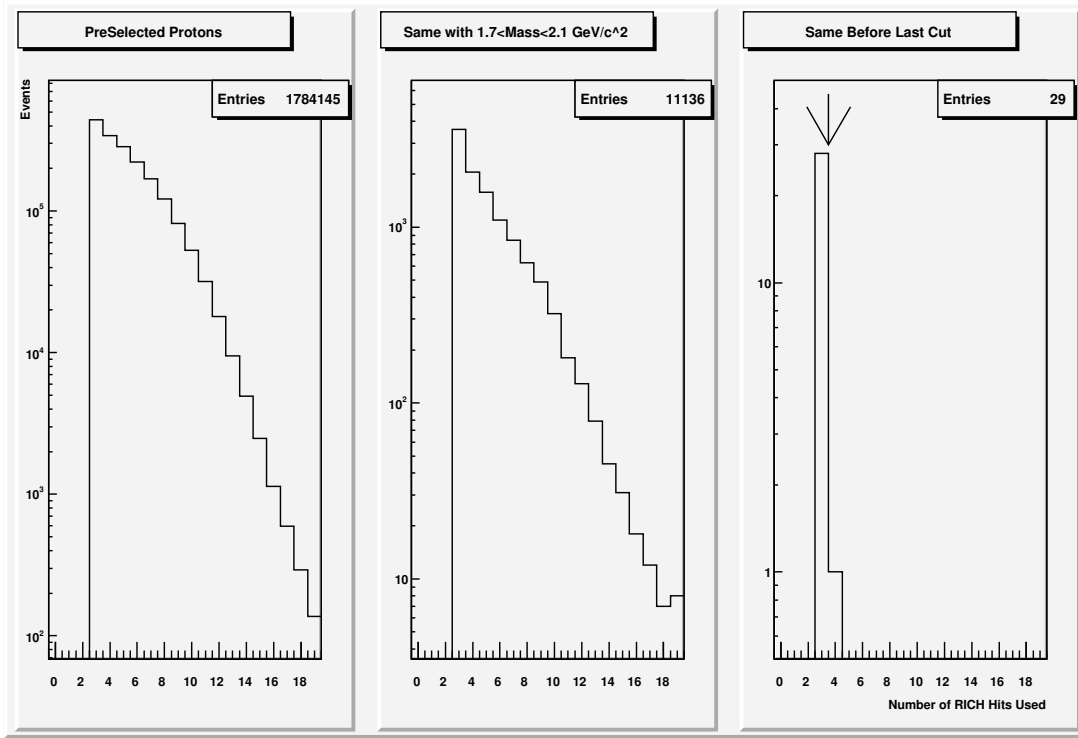
Figure 5.9: Distribution of the number of hits used to reconstruct the RICH ring for the proton sample. At least four hits are required and this selection rejects 28 events otherwise reconstructed as deuterons (antideuterons).

resolution measured during the beam test 2003 at CERN for different Z value is given in figure 5.8(a), while the measured charge resolution up to $Z = 24$ is shown in figure 5.8(b).

Whenever a β value is provided by the RICH detector, this measurement is preferred to that of TOF. To improve the RICH particle β reconstruction, a set of quality cuts are applied to the sample. In particular:

- at least 4 hits on the RICH detection plane, belonging to the used RICH ring,

are required in order to have enough points to reconstruct the ring for providing the particle velocity. The effect of this cut on the proton sample is shown in figure 5.9. As stated in the previous section, the proton sample is used instead of that of antiproton, but a positive momentum is required.

In addition, a lower limit on the probability of being a good ring is demanded and its effect is illustrated in figure 5.10.

If the particle β is correctly associated by the RICH detector, as well as its Z value, the number of collected photons N_{coll} recognized by the reconstruction algorithm as belonging to the ring is expected to be compatible with N_{exp}. Events badly reconstructed or affected by noise or secondary particles production can be reduced imposing a constraint for the
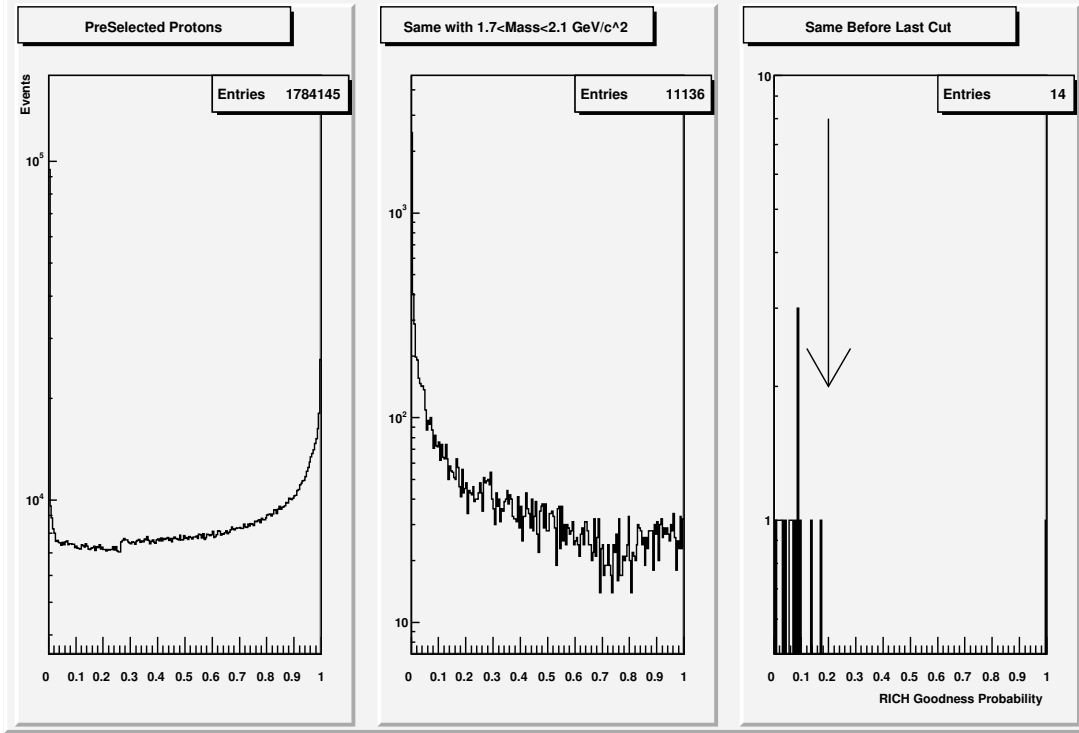
Figure 5.10: The probability to be a good ring is displayed for the proton sample. Only events with values greater than 0.2 are accepted.

quantity $K = N_{\exp}/N_{\mathrm{coll}}$. At the same time, these limits should not be too strict in order to take into account some structural effects. As a matter of fact, the determination of $N_{\exp}$ is not always trivial and has to take into account for instance photon loss in the ECAL hole or their reflection against the mirror. Finally, a reasonable compromise results in the following cut:

- $0.4 < \frac{N_{\exp}}{N_{\mathrm{coll}}} < 2$,

The relative plots are shown in figure 5.11(a).

Then, unused hits could reveal events with interaction. Excluding the *hot spots*, the selection requires that:

- the number of hits not considered for the β reconstruction algorithm should be limited to 3,

as illustrated in figure 5.11(b).

Moreover, sometimes some of these unused hits are located very closed to the reconstructed ring, but oddly not used by the algorithm. This strange behaviour of beta reconstruction algorithm is suspicious, so events are rejected if:

$$D_{\mathrm{UnusedHit}} = \sum \frac{1}{R^2} < 0.3 \text{ cm}^{-2} , \tag{5.3}$$
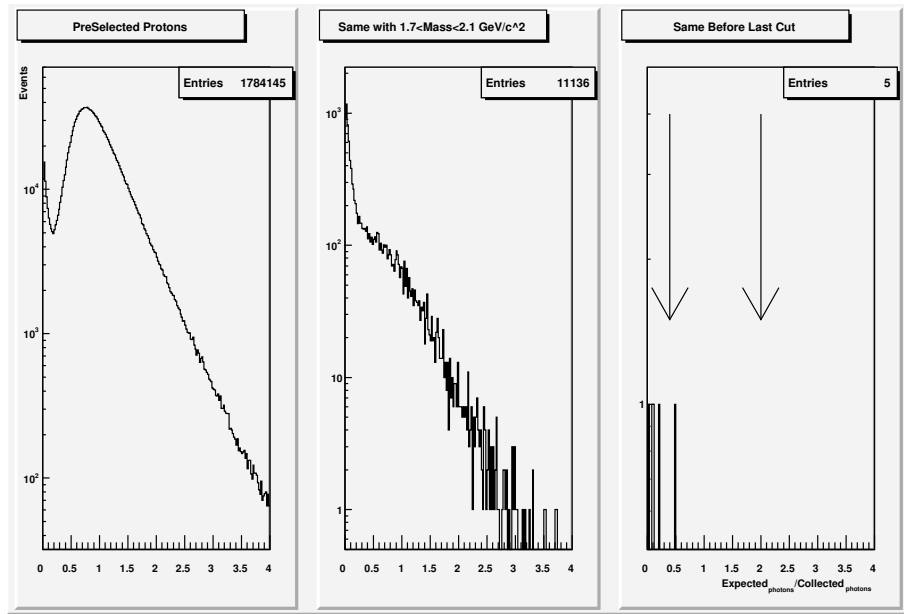
(a)
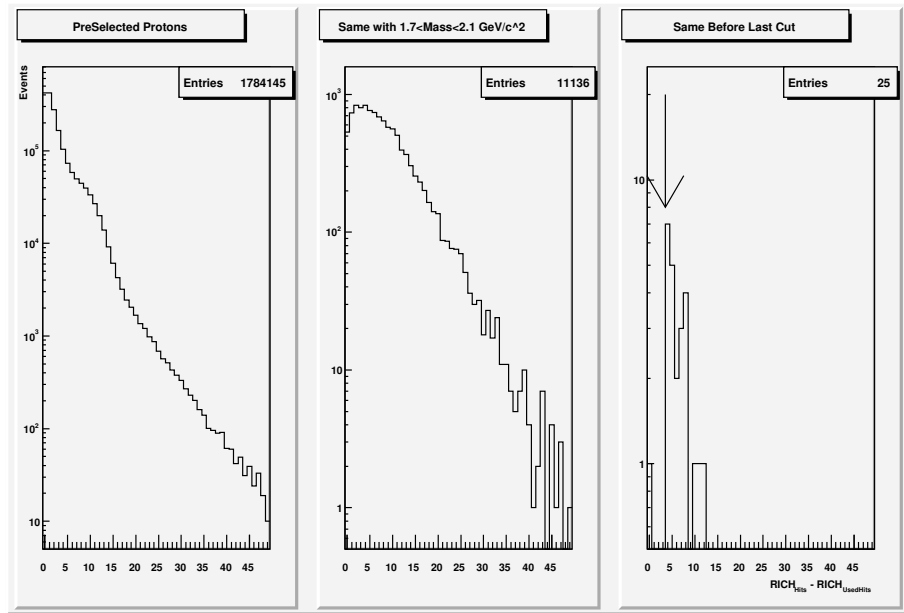
(b)

Figure 5.11: (a)The ratio between the expected and collected number of photoelectrons is plotted for protons. The eight events surviving all the other cuts are rejected by requiring this quantity to lay between 0.4 and 2. (b) The number of hits not used to measure the particle β is required to be at least 3.
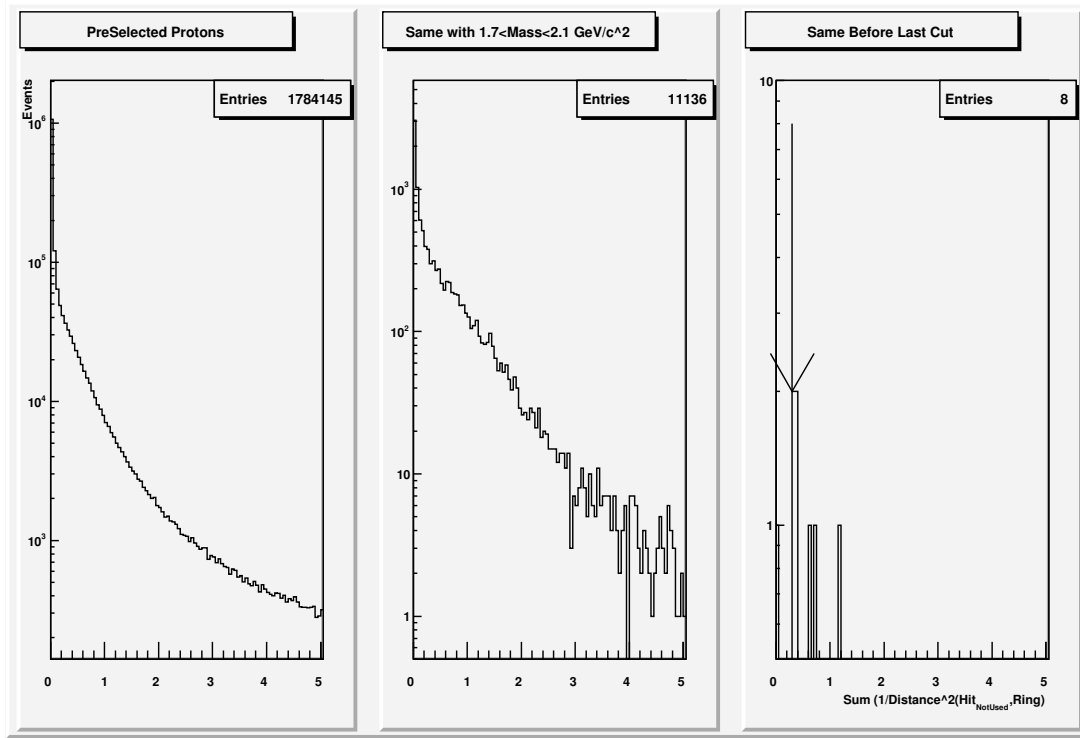
Figure 5.12: Distribution of $D_{\mathrm{UnusedHit}}$ described in the text for the preselected proton sample. Only one event out of eight passes the applied cut corresponding to $D_{\mathrm{UnusedHit}} < 0.3 \; \mathrm{cm}^{-2}$.

where R is the distance between the unused hit and the RICH Ring reported in figure 5.12.

Once all cuts are applied, the final distribution of the rigidity for the remaining protons is plotted in figure 5.13. Only one event survives below 10 GV, hence in the RICH range a threshold could be reasonably set:

$$R \; < \; 10 \; \mathrm{GV} \; . \tag{5.4}$$

This last event at 7.98 GV represents an irreducible background, which looks like a normal event, as can be seen in figure 5.14 and in figure 5.15 for a top view.

5.3.5 Electron background specific cuts

All the previous cuts are also important to reduce electron contamination to antideuteron signal, but to achieve the required rejection power at the level of 10^{-9} additional means are necessary. In particular, the contribution of the Transition Radiation and the Electromagnetic Calorimeter detectors, specialized to proton/electron separation is decisive.

78
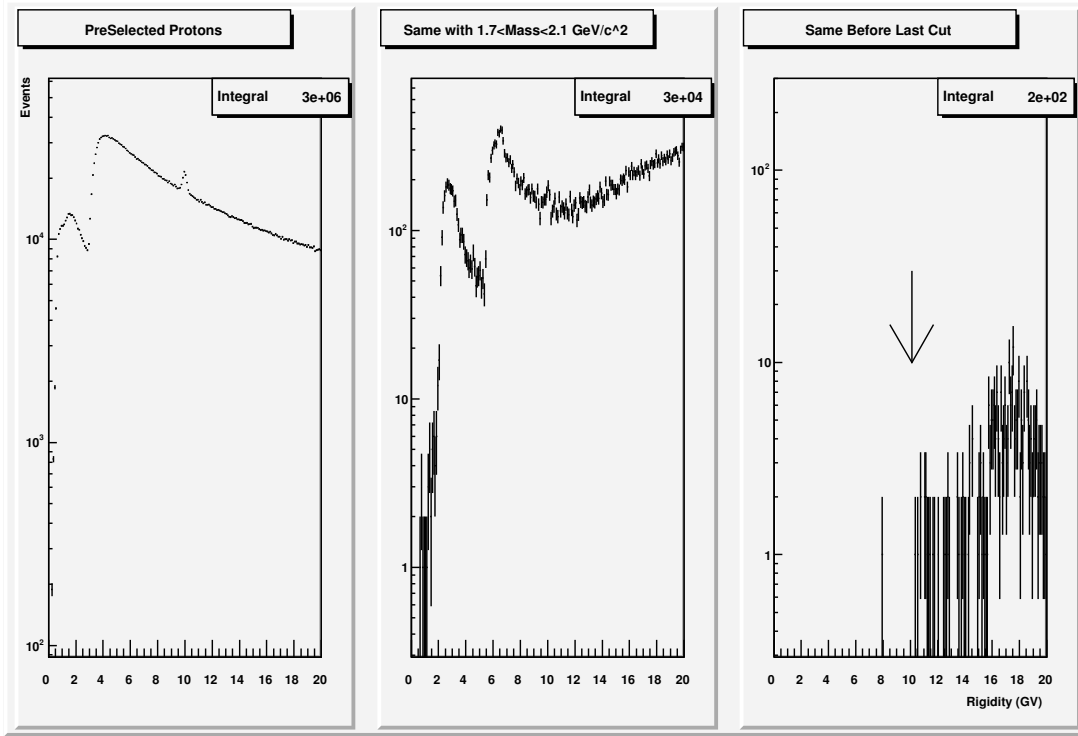
Figure 5.13: Rigidity distribution for the proton sample.

Their peculiarity is to trigger physical fenomena which prefer electromagnetic particles like electrons and positrons, instead of hadrons (like protons and deuterons).

When a photon or an electron enters the ECAL, an e.m. shower is produced and most of its initial energy is released inside the detector sensitive area. Other particles also interact with its material, but, since they do not generate an e.m. shower, they leave just a part of their energy according to the Bethe Block formula. Assuming for electrons that the energy loss in the ECAL (E_{ECAL}) is a good estimator of their proper energy, the ratio between E_{ECAL} and the momentum measuread by the Tracker (P_{Tracker}) is expected to be closed to one, being approximately equal to $1/\beta$. Otherwise if E_{ECAL} is far enough to be a correct measurement of the particle's total energy, $E_{\mathrm{ECAL}}/P_{\mathrm{Tracker}}$ is forced to be lower than one.

In general for protons and deuterons this quntity is lower than 1, except at low energies, for which the particle is not a minimum ionizing particle (MIP) and its energy loss becomes larger. So for reconstructed momenta above 2 GeV/c it is required:

- $E_{\mathrm{CAL}}/P_{\mathrm{Tracker}} < 1$.

So the capability of the ECAL, placed in the bottom of AMS02 experiment, to distinguish between these two cosmic rays components is important, despite of its reduced dimensions.
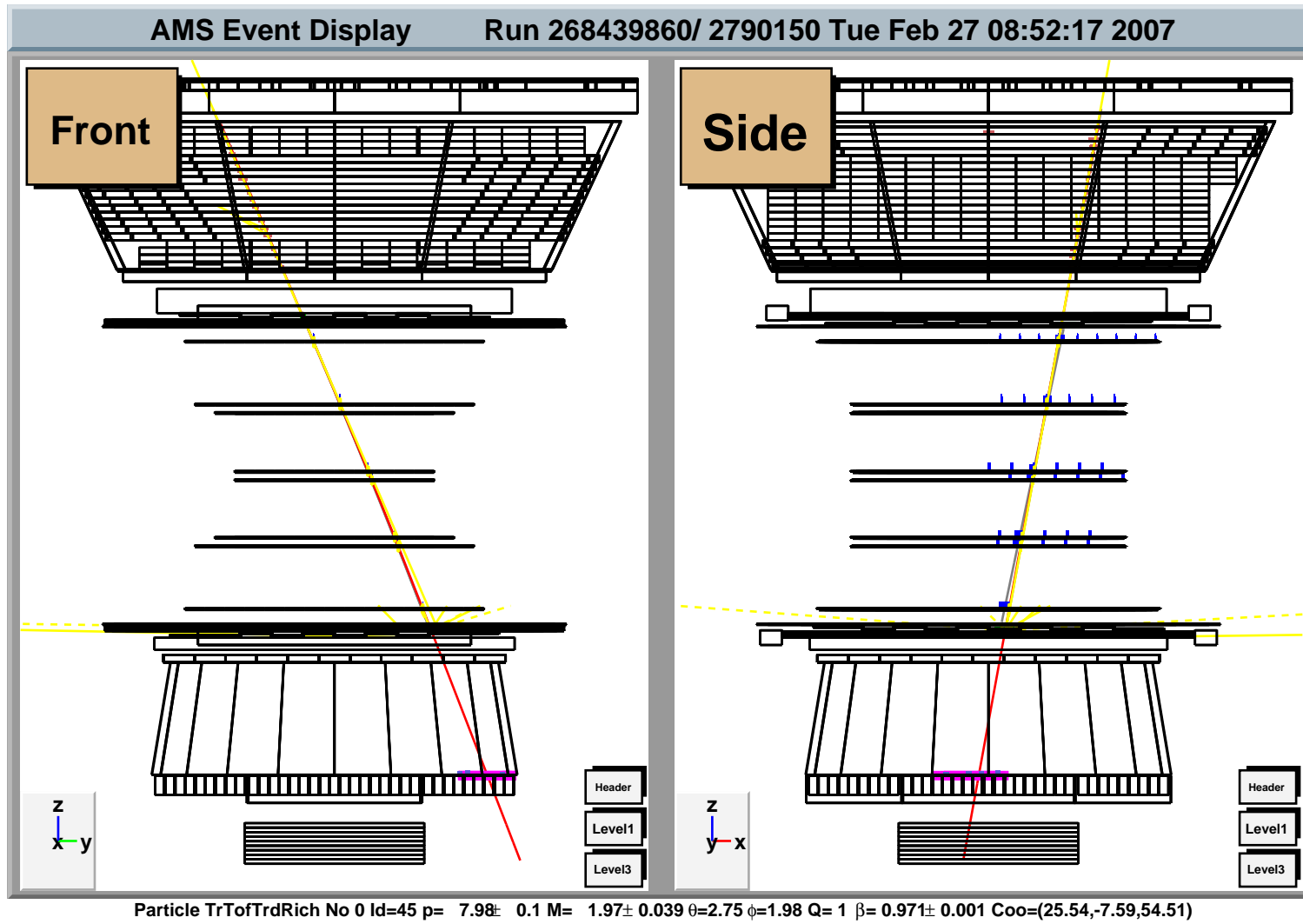
Figure 5.14: Side view of the event as shown by the AMS-02 event display program for the last irreducible proton (antiproton) background in the RICH region
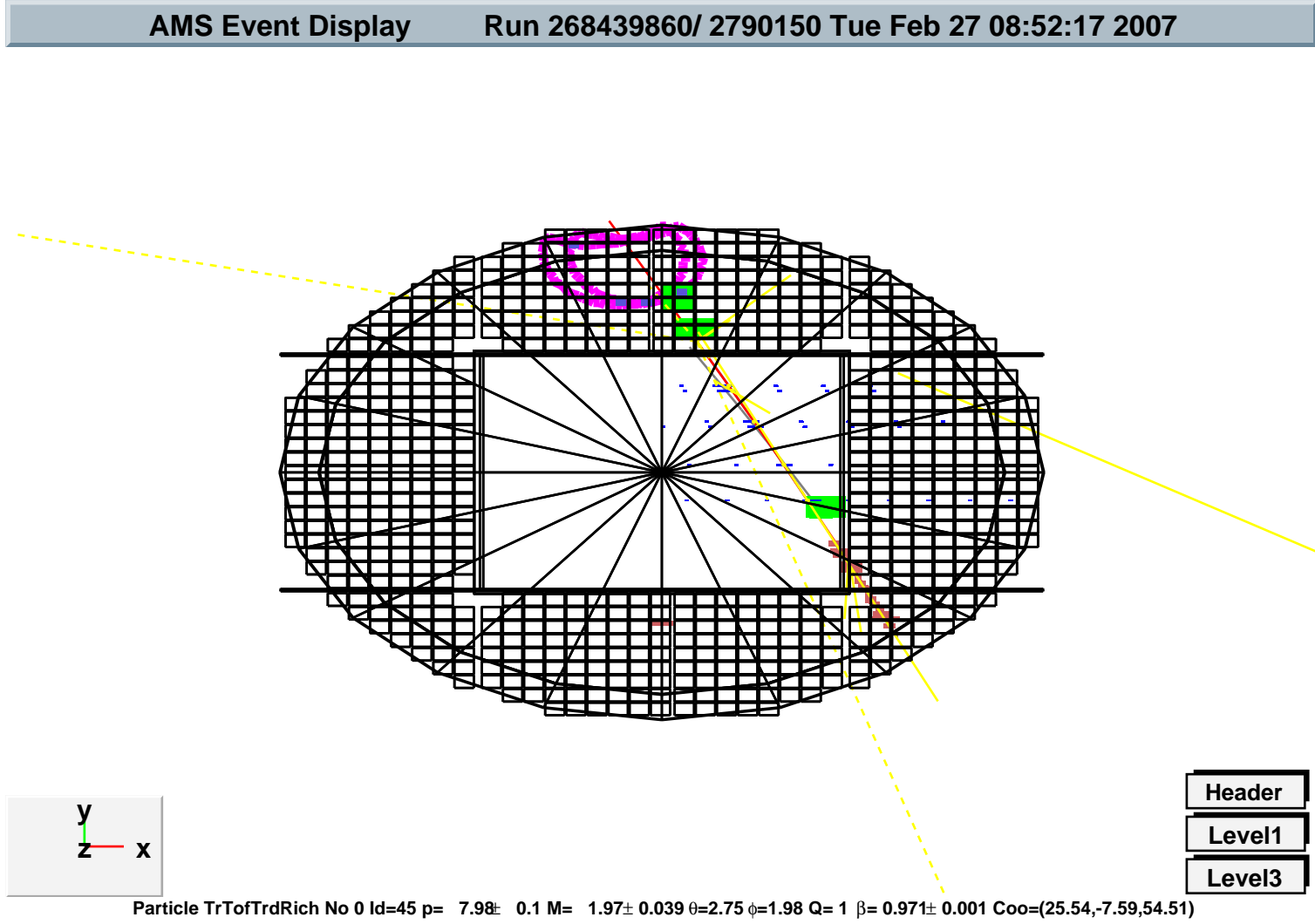
Figure 5.15: Top view of the RICH detection plane for the last irreducible proton (antiproton) background in the RICH region.
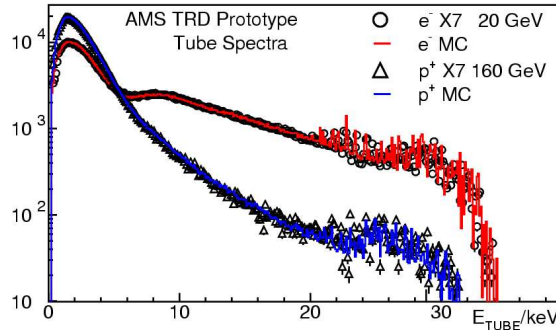
Figure 5.16: TRD response for electrons and protons [94].

The Transition Radiation detector takes on an important task, thanks also to its position above AMS-02 and its large acceptance. As described in chapter 2.1.5, the operating principle of this detector is that light particles, such as electrons and positrons, have a much higher probability of emitting TR photons than heavier particles such as deuterons. All particles traversing straw tubes undergo an ionization process and can produce a signal, as is clearly illustrated in figure 5.16, where the distribution of energy collected by one tube is peaked around 2 KeV for both electron and proton samples. From the same figure 5.16 it is possible to ascertain that electrons and positrons have an additional higher probability ($\sim$ 50%) of emitting collimated x-rays and thus to release a total energy larger than 6 KeV in the straw tube. The AMS-02 TRD, being built by 20 layers of TR modules, each one of 16 straw tubes, could give up to 20 independent measures of the energy loss. In order to have enough redundancy on TRD measurements it is required to the reconstructed event to have:

- a number of TRD Hits (multiplicity) along the track > 11.

An empirical evaluation of the energy loss as function of particle momentum for an hadron with $Z = 1$ is used [1] :

$$E_{\text{loss}}^* = \frac{0.3 \log p}{\beta^{5/3}} KeV \ .$$ (5.5)

In this analysis an event is also removed if:

- the number of TRD Clusters with $E_{\text{loss}} > E_{\text{loss}}^*$ is greater than 2.

The powerful effect of this selection on the electron sample can be better appreciated in figure 5.21 of § 5.4.3 where the estimation of the rejection power for electrons is addressed.

---

[1]V. Choutko, private comunications

5.4 Background rejection power

5.4.1 Proton and deuteron background

The huge protons flux and, conversely, the faint antideuteron signal in cosmic rays make the suppression of proton background a truly challenging task, which requires an excellent particle/antiparticle discrimination. In addition, a direct estimation of the AMS-02 rejection power for this species demands an unrealistic amount of MC data and this is impossible for the time being. Also the deuterons rejection experiences the same critical problem.

Both protons and deuterons could mimic antideuteron signal only if the sign of their tracks is reconstructed with the opposite sign. So the sample of suspicious events is formed only by protons that are reconstructed as negative particles and survive the selection made up applying all quality cuts on Tracker rigidity reconstruction and cuts devoted to suppress events with interactions (as explained in § 5.3.1 and 5.3.2), but without any request for the TOF and RICH velocity measurements optimization. In particular, remaining events with ratio R_{meas}, the measured rigidity, over R_{gen}, generated rigidity, closed to -2 are highly favoured to mimic antideuterons. But no events fall in the window 1.8–2.2 over the all available MC protons sample in the range 0.5–200 GeV of about 2×10^8 events.

Secondary K$^-$ and π^- particles produced by proton interaction in TRD and the honeycomb support structure before entering the tracking volume, due to kinematical reasons, are explicitly excluded from the fit. The final distribution of $-R_{\mathrm{meas}}/R_{\mathrm{gen}}$ is reported in figure 5.17.

Assuming that an exponential trend could be reasonably attributed to this distribution, the number of events expected in the window 1.8–2.2 ($N_{\mathrm{exp}}(\mathrm{p})$) is computed, to be conservative, using the exponential function with slope = -9.15+1σ=-7.15. The Rejection factor R_{f} for protons is therefore estimated:

$$R_{\mathrm{f}}(\mathrm{p}) \sim \epsilon \, \frac{N(\mathrm{p})}{N_{\mathrm{exp}}(\mathrm{p})} > 0.54 \, \frac{5.3 \times 10^7}{3.8 \times 10^{-5}} \sim \; 8 \times 10^{11} \; , \qquad (5.6)$$

where $N(\mathrm{p})$ is the preselected proton sample and ϵ is the efficiency of all the analysis selection criteria, inferred from the antiproton sample:

$$\epsilon = \frac{N_{\mathrm{sel}}(\overline{\mathrm{p}})}{N_{\mathrm{tot}}(\overline{\mathrm{p}})} \; , \qquad (5.7)$$

where $N_{\mathrm{tot}}(\overline{\mathrm{p}})$ is the number of antiprotons after preselection and $N_{\mathrm{sel}}(\overline{\mathrm{p}})$ is the number of antiprotons surviving all cuts applied in this analysis.

The same method can be used to estimate deuteron contamination assuming a similar behaviour for p/$\overline{\mathrm{p}}$ contamination with respect to d/$\overline{\mathrm{d}}$ one. In that case $N_{\mathrm{exp}}(\mathrm{d})$ is computed in the window 0.8–1.2, demarked in figure 5.17, and the resulting rejection factor is estimated:

$$R_{\mathrm{f}}(\mathrm{d}) > \; 1.5 \times 10^9 \; . \qquad (5.8)$$
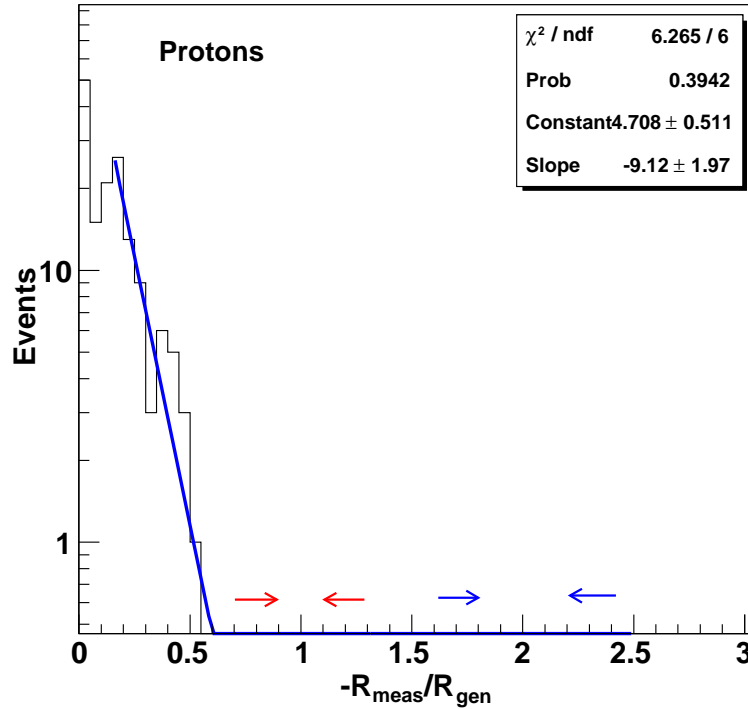
Figure 5.17: Negative ratio of measured momentum R_{meas} over the generated one R_{gen} for MC proton sample after the selection described in the text. The distribution is fitted with an exponantial function to make an estimation of the number of events expected in the ranges limited by arrows.

5.4.2 Antiproton background

Assuming the same rejection factor for antiprotons versus antideuterons and for protons versu deuterons, the MC proton sample is used to study antiproton contamination because of its wider availability.

In the TOF momentum range, no antiproton event was reconstructed as antideuterons after the described event selection, if an upper limit is fixed in the TOF reconstructed velocity corresponding to $\beta < 0.815$, as was shown in figure 5.7.

The distribution of the mass for the final clean sample of protons after all cuts (except mass) is reported in figure 5.18(a), which corresponds to the distribution of the reconstructed mass for the deuteron sample in figure 5.18(b). The rejection power for antiprotons is computed from the ratio between the number of protons in a chosen bin passing all cuts N_{sel} and the number of protons amomg them which are reconstructed as
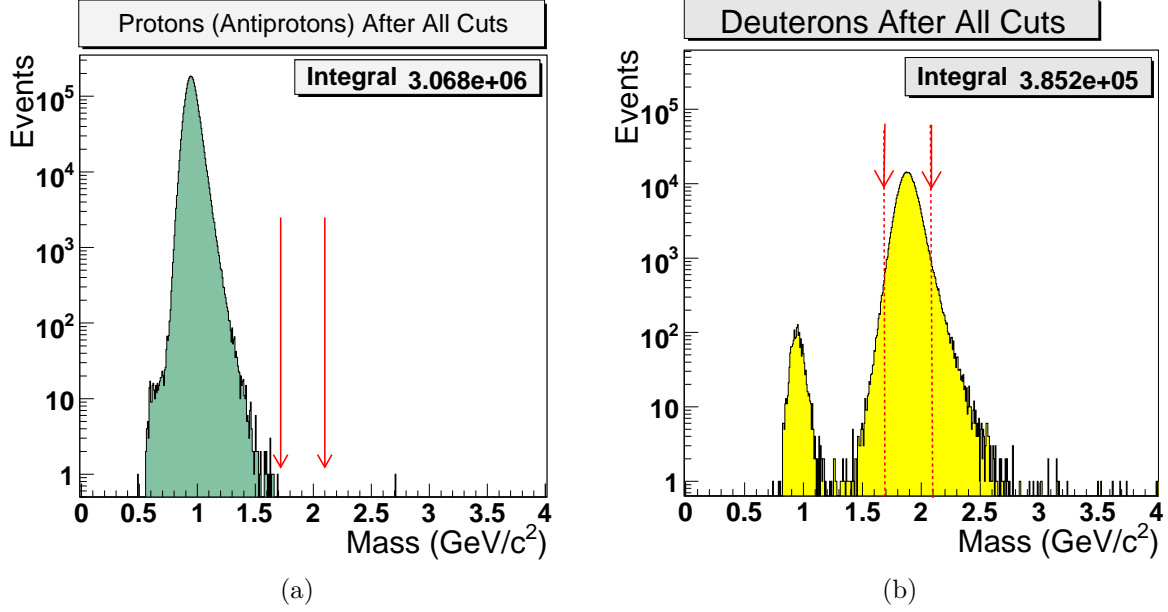
Figure 5.18: (a) Mass distribution for the selected proton (antiproton) sample and (b) for the selected deuteron (antideuteron) sample. No proton (antiproton) event falls in the deuteron mass window demarcated between the red arrows.

deuterons $N_{\text{sel}}(\text{p} \rightarrow \text{d})$:

$$R_{\text{f}}(\overline{\text{p}}) = \frac{N_{\text{sel}}(\overline{\text{p}})}{N_{\text{sel}}(\overline{\text{p}} \rightarrow \overline{\text{d}})} = \frac{N_{\text{sel}}(\text{p})}{N_{\text{sel}}(\text{p} \rightarrow \text{d})} \ . \tag{5.9}$$

The plot of the final values so inferred is shown in figure 5.19, where the rejection power for antiprotons is reported:

$$R_{\text{f}}(\overline{\text{p}}) \ _{\text{TOF}} \ \sim \ 6 \ \times 10^6 \pm 4 \ \times 10^6 \ , \tag{5.10}$$

up to 1.4 GeV/nucl kinetic energy, fastly decreasing at higher energies.

In the RICH momentum range the rejection factor for antiprotons is computed in the same way. The distribution of the reconstructed mass for the proton and deuteron sample is shown in figure 5.20. Only one event with reconstructed rigidity below 10 GV enters the deuteron mass window. The rejection factor for antiprotons in the RICH range up to kinetic energy 7.2 GeV, where one $\overline{\text{p}}$ event mimic $\overline{\text{d}}$ is so found:

$$R_{\text{f}}(\overline{\text{p}}) \ _{\text{RICH}} \ \sim \ 2 \times 10^5 \pm 1 \times 10^5 \quad (E_{\text{kin}} < \ 7.2 \ \text{GeV}) \ . \tag{5.11}$$

A lower value is derived at higher kinetic energy between 7.2 and 8.9 GeV:

$$R_{\text{f}}(\overline{\text{p}}) \ _{\text{RICH}} \ \sim \ 2 \times 10^4 \pm 1 \times 10^4 \quad (7.2 \ < E_{\text{kin}} < \ 8.9 \ \text{GeV}) \ . \tag{5.12}$$
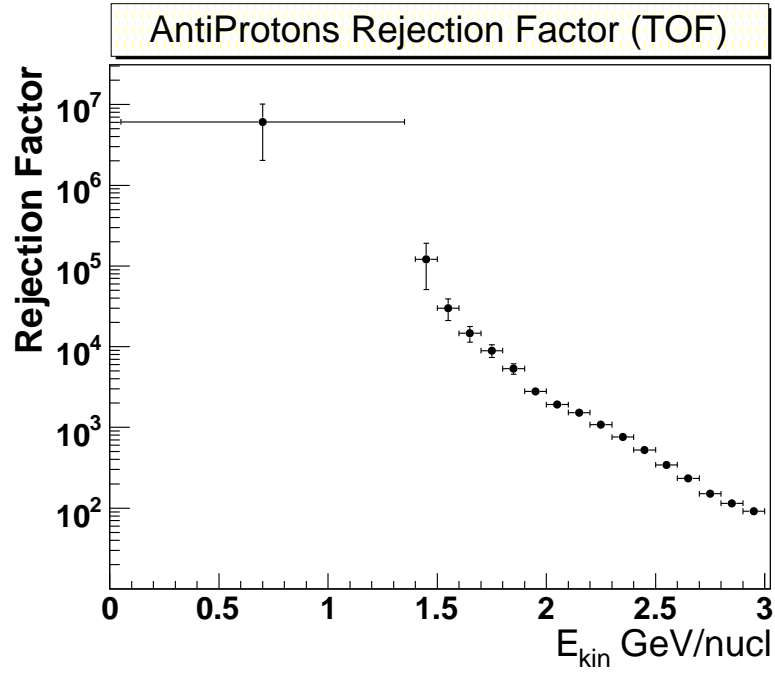
Figure 5.19: The rejection power for antiprotons versus kinetic energy. The lower uncertainty on $R_{Factor}(\overline{p})$ in the bin up to 1.4 GeV/nucl, where no events are found in the deuteron mass window, estimated at 90% CL.
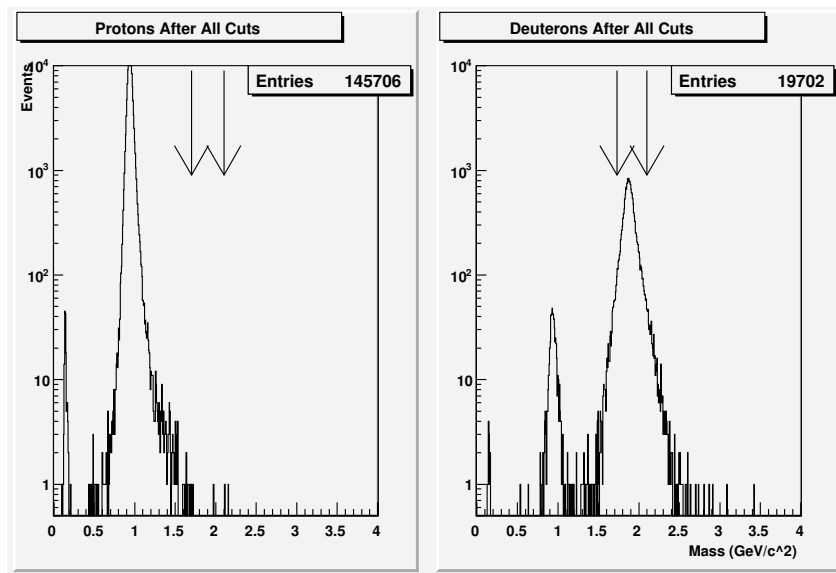
Figure 5.20: Mass distribution for the selected proton (antiproton) sample and for the selected deuteron (antideuteron) sample in the RICH momentum range. Only one proton (antiproton) falls in the deuteron mass window demarcated between the arrows.
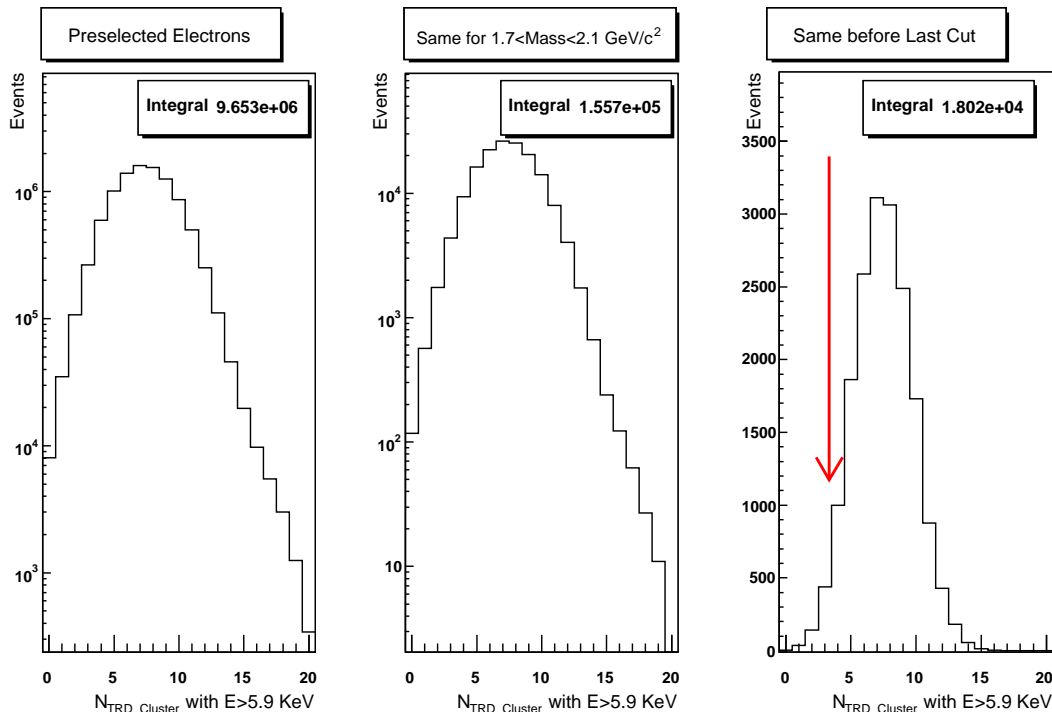
Figure 5.21: Distribution of the number of clusters with energy loss above ~ 5.9 KeV (depending on momentum as reported in the text in § 5.3.5) for electron sample.

5.4.3   Electron background

The last kind of background taken into account in this work is the electron contamination. The available MC electron statistics are not yet sufficient to make a direct evaluation of the rejection power that could be achieved for this source of background. Nevertheless a lower limit can be inferred by applying the TRD cuts, the velocity cut and the mass cut separately as the last cut. The rejection power for electrons is estimated by considering separately the TOF region and the RICH region by applying quality cuts respectively on TOF or on RICH particle β reconstruction.

First, a general observation can be made which is valid both for TOF and RICH region. We can see from figure 5.21 that the cut on the number of TRD clusters with energy loss above ~ 5.9 KeV is very powerful and so a factor 90 in rejection power is given due to TRD electron/hadron separation alone. Second, in the TOF region the distribution of the electron sample after all selection cuts, except TRD specific cuts and the mass cut is fully placed above $\beta = 0.815$, as shown in the left plot of figure 5.22, where the cut of the TOF velocity reconstruction is placed. Thus the whole final electron sample counting 1.6×10^6 events is rejected. Finally, the mass cut is applied giving an additional factor greater than 20 as derived from the right plot shown in figure 5.22 of the ratio between
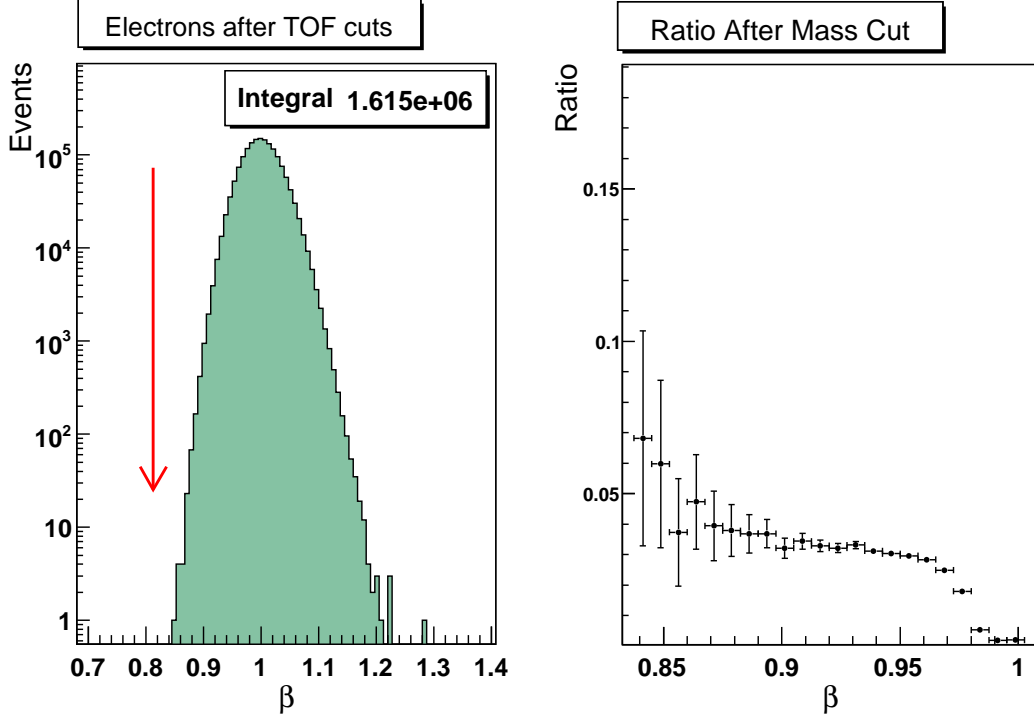
Figure 5.22: Left: distribution of the velocity reconstructed by TOF for the electron sample after all cuts except TRD, velocity and mass cuts. Right: ratio between the number of events before and after the mass cut, as a function of reconstructed β.

the number of events before and after mass cut falling in each bin. The rejection factor in the TOF region is given by:

$$R_f(e^-)_{\text{ TOF}} > 1.6 \ 10^6 \times 20 \text{ (MassCut)} \times 90 \text{ (TRD)} = 2 \times 10^9 \ . \qquad (5.13)$$

In the RICH region a similar method is adopted. The electron sample after all cuts except TRD consists of about 1×10^5 events. The velocity distribution of this final electron sample and its mass distribution are shown in figure 5.23. From the exponential fit of the right side of the mass distribution the number of events falling in the deuteron mass window is estimated and a factor 6 can be obtained.

To conclude the rejection factor in the RICH region is computed:

$$R_f(e^-)_{\text{ RICH}} > 10^5 \times 6 \text{ (Mass)} \times 90 \text{ (TRD)} = 5 \times 10^7 \ . \qquad (5.14)$$
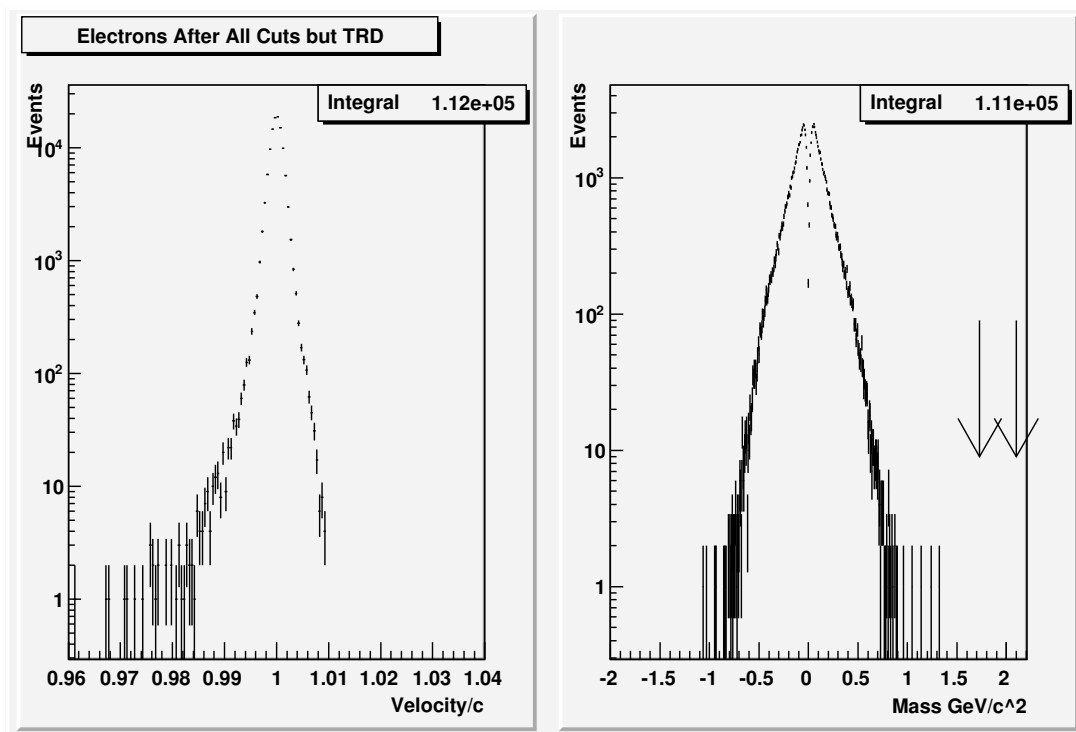
Figure 5.23: Distribution of the velocity measured by RICH on the left and, on the right, the plot of the electron mass for the selected sample.

5.5   Results

A flux of secondary antideuterons of standard astrophysical origin is predicted above 1.5–2 Gev/n, on the based of the considerations discussed under § 1.5.4. An additional primary component may be produced from exotic sources, like Dark Matter neutralino annihilation. This primary flux may reach up to $\sim 10^{-6}$ m^{-2}s^{-1}sr^{-1}GeV^{-1} and it is peaked below 1 GeV/n, where no standard component is expected [29]. Cosmic Ray antideuterons, in the low energy range, are considered a more sensitive signature than antiprotons for the existence of new primary sources.

5.5.1   AMS-02 antideuteron final acceptance

The cuts described along this chapter have been implemented in order to reduce all the possible sources of contamination to the very small antideuteron signal, which so far had not detected in Cosmic Rays.

The final AMS-02 acceptance for deuterons, resulting from the application of the selection analysis, is shown in the top plot of figure 5.24 as a function of the generated momentum. The antideuteron acceptance, shown in the bottom plot of the same figure,
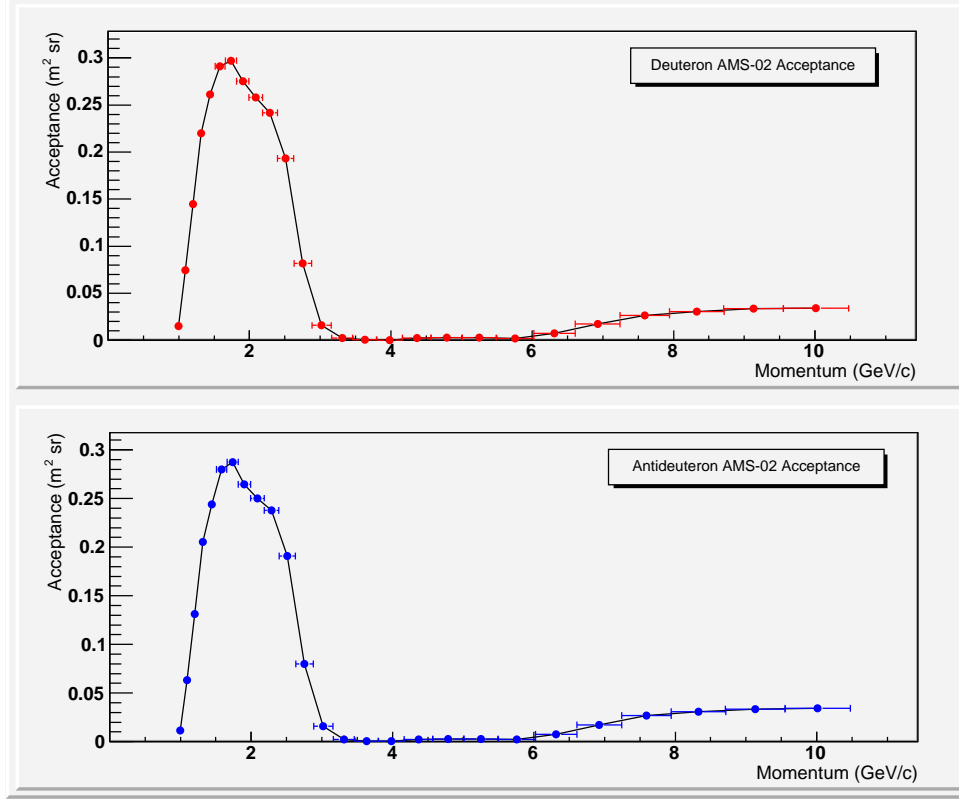
Figure 5.24: Final AMS-02 acceptance for deuteron (upper plot) and antideuteron signal (lower plot).

is obtained from the deuteron acceptance, knowing the correction factor that was derived in § 5.2.2 from the ratio $\mathrm{Acc_{geom}(d)/Acc_{geom}(\overline{d})}$.

In order to estimate the signal contamination an important quantity to be computed is the signal over background ratio (S/B):

$$S/B = \frac{\int_{E_{\mathrm{k,min}}}^{E_{\mathrm{k,max}}} \frac{\Phi_{\overline{\mathrm{d}}}(E_{\mathrm{k}})}{\Phi_{\mathrm{bg}}(E_{\mathrm{k}})} \mathrm{d}E_{\mathrm{k}} \ R_f(\mathrm{bg})}{\int_{E_{\mathrm{k,min}}}^{E_{\mathrm{k,max}}} \mathrm{Acc}(E_{\mathrm{k}}) \ \mathrm{d}E_{\mathrm{k}}} \ . \tag{5.15}$$

The S/B ratio has been estimated both for TOF and RICH regions for all the sources of background to antideuteron signal considered in this thesis, namely protons, deuterons, antiprotons and electrons and they are reported in table 5.2. The TOF kinetic energy operating range resulting from this analysis is between 0.2 and 1 GeV, while the RICH one goes from 2.1 up to 4.2 GeV.

The Signal over Background Ratio is greater than one for all background species. However, a larger amount of MC statistic is necessary and would help to estimate electron, proton and deuteron rejection power, that for the moment are derived indirectly and therefore just a lower limit on their values can be fixed.

Particle	S/B Ratio (TOF)	S/B Ratio (RICH$_{Agl}$)
Protons	> 15	> 800
Deuterons	> 1.6	> 60
Antiprotons	6	1.3
Electrons	> 1.2	> 3.3

Table 5.2: Signal over Background Ratio in TOF and RICH energetic ranges, for all kinds of background considered in this thesis.
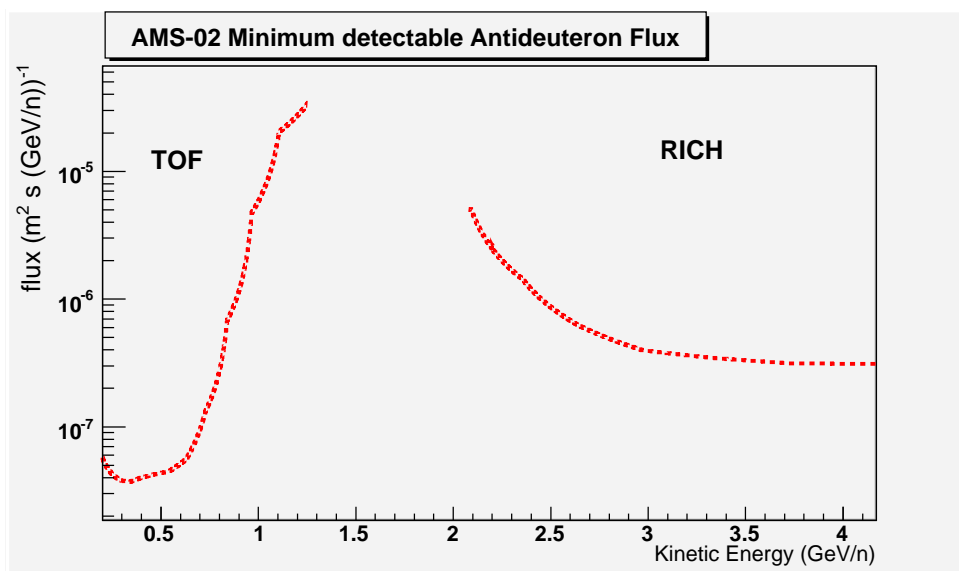
Figure 5.25: Minimum antideuteron flux detectable by AMS-02 experiment in 3 years of data taking as a function of the kinetic energy (GeV/n) both in TOF and RICH ranges.

5.5.2 Antideuteron spectrum measurement example

By means of the estimated antideuteron acceptance, it is possible to answer to the question on the possibility for AMS-02 to detect such $\overline{d}$ signal and in particular to search for indirect Dark Matter signatures throught this physics channel. The estimated minimum detectable antideuteron flux for AMS-02 in three years of data taking is reported in figure 5.25 as a function of the kinetic energy.

Figure 5.26 compares the sensitivity of the AMS-02 experiment to the expected primary and secondary $\overline{d}$ fluxes. In the energy range between 0.2 and 0.8 GeV/n AMS-02 will be able to detect primary antideuterons if their flux is greater than 5–6$\times 10^{-7}$ (m^2 s sr GeV/n)$^{-1}$. From data collected from BESS spectrometer during four baloon flights from 1997 to 2000, an upper limit of 1.9×10^{-4}(m^2 s sr GeV/n)$^{-1}$ was set for the

91

Case	m_χ	$P(\%)$	$\Omega_\chi h^2$	$N_{\text{AMS}-02}$
a	36.5	96.9	0.20	0.4
b	61.2	95.3	0.13	2
c	90.4	53.7	0.03	1
d	120	98.9	0.53	0.2

Table 5.3: The supersymmetric parameter values set for the correponding flux case are illustrated in table, where m_χ is the neutralino mass, $P(\%)$ is the parameter used to classify the nature of neutralino as explained in § 1.3.3 and $\Omega_\chi h^2$ is the neutralino energy density. In the last column the estimated number of events expected from AMS-02 in three years is reported.

differential flux of CR anti-deuterons in the range between 0.17 and 1.15 GeV/n [95].

The possibility to observe primary $\overline{\text{d}}$s depends strongly on the kind of SUSY model used, on the DM density profile, and on the choise of the Cosmic Rays propagation and fusion models adopted. Some reasonable assumptions on these paremeters were done as motivated in § 1.5.

Four cases of primary antideuteron fluxes, shown in figure 5.26, were computed varying for example the supersymmetric parameters considered in table 5.3 [29]. No obvious correlation between the flux and the neutralino mass is pointed out. For each example of primary $\overline{\text{d}}$ flux so derived, the number of events for AMS-02 in three years of data taking may be estimated:

$$N(\overline{\text{d}}) = \int \Phi_{\overline{\text{d}}} \, C_{\text{Geo\_CO}} \, \text{Acc} \, T \, \text{d}E_{\text{k}} \, , \tag{5.16}$$

where T is the exposure time in seconds, $C_{\text{Geo\_CO}}$ is the correction coefficient introduced to account the drop of the low energy particle flux caused by the geomagnetic cut off [96].

The results are reported in table 5.3, where in one case (flux labelled with b) about 2 events below 1 GeV/n are expected to be collected by AMS-02 in 3 years. However, as already remarked, the uncertanties on these fluxes, at present time, are substantial and mainly related to the fact that the sources of primary fluxes are located inside the diffusive halo, whose size is unknown. Therefore, the primary flux can be expected larger than one considered in this thesis [29] and a new work is in preparation about this [2].

---

[2] F. Donato, private communications
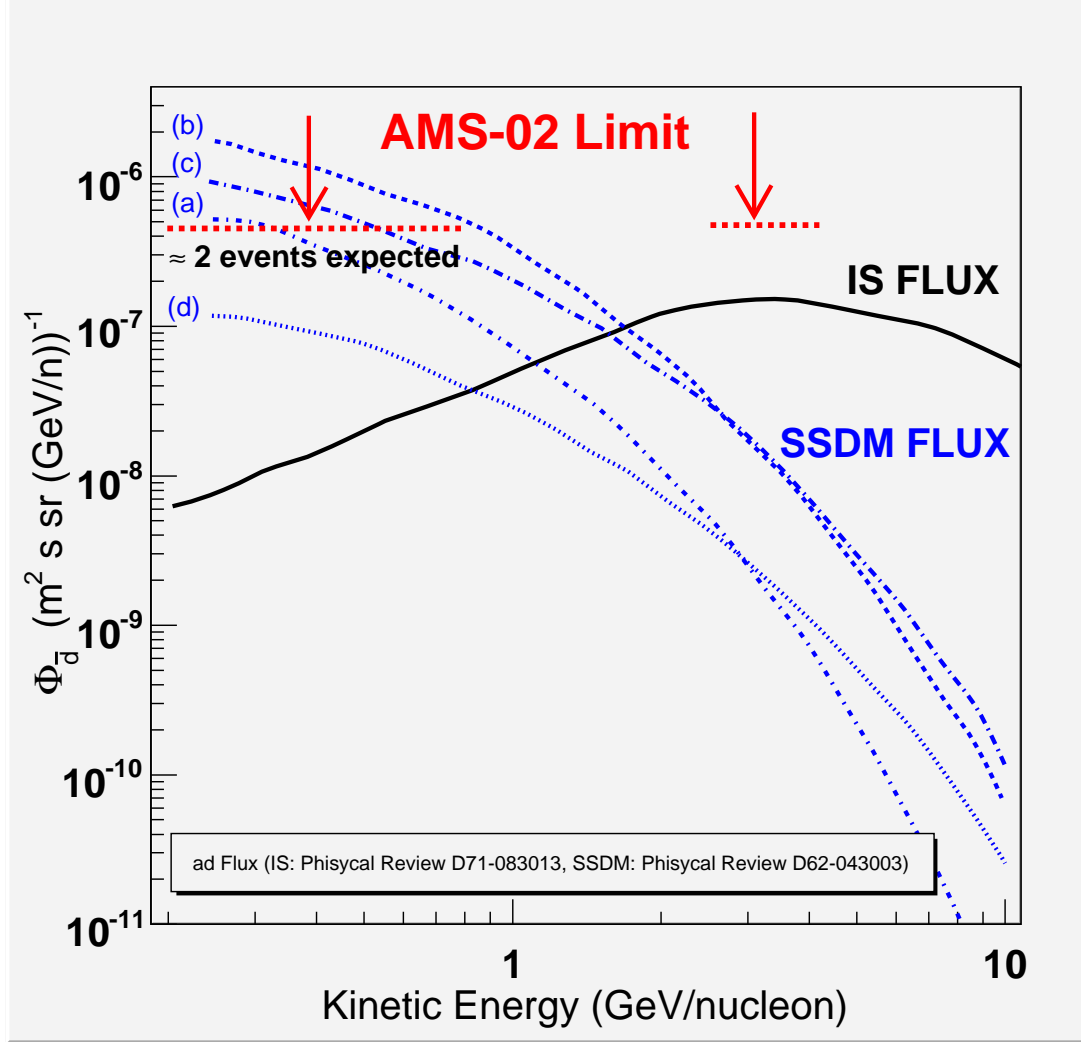
Figure 5.26: Extimated AMS-02 sensitivity limit for the antideuteron flux measurement compared to: the $\overline{\text{d}}$ secondary IS flux derived as discussed in § 1.5.3 [14]; the $\overline{\text{d}}$ primary flux coming from the neutralino Dark Matter annihilation as illustrated in § 1.5.4 [29] for different supersymmetric parameters (labelled with a, b, c, d) reported in table 5.3. The limit is reported separately in TOF and RICH energetic ranges. A number of about 2 events of antideuterons below 1 GeV/n are expected for AMS in three years of data taking considering the higher predicted flux corresponding to curve b.

Conclusions

The capability of the AMS-02 experiment to reveal antideuteron signal in Cosmic Rays (CR) has been explored. Cosmic Ray antideuterons, in the low energy range, are considered a sensitive signature for the existence of new primary sources, like Dark Matter neutralino annihilation in the galactic halo of the Milky Way. The weakness of the antideuteron flux makes this study particularly challenging even for an experiment like AMS-02, characterized by a large acceptance and a good particle identification.

The detection capability of the AMS-02 Time of Flight (TOF) detector, which measures the particle velocity below about 1.5 GeV/n, where the antideuteron primary component is expected, is crucial in the searching for this physics channel. The TOF performances have been evaluated on the basis of beam test data, which provide a time of flight resolution better than 180 ps for protons and about 100 ps for light ions. In addition, a good particle charge identification has been verified for light and intermediate ions. The study of the TOF behaviour and stability under space conditions was carried on showing no radiation damage effects within the maximum absorbed dose expected in ten years and a thermal dependence of the the detector response in agreement with literature. The space qualification test on the Lower TOF has been succesfully concluded and a similar test is in preparation for the Upper TOF.

This study on the AMS-02 sensitivity to the antideuteron signal has been performed on Monte Carlo (MC) data. To take into account the nuclear inelastic interactions of deuterons and antideuterons inside the detector, their relative cross sections have been implemented into the official AMS-02 MC code. The universal parameterization proposed by Tripathi and co-workers, which gives the best fit to most of the measurements of nucleus-nucleus inelastic cross sections, has been introduced to describe deuteron interactions. On the other hand, only few data are available on antideuteron cross sections particularly in the low energy range, where their probability to interact is expected to have a rapid rise mainly due to annihilation. Thus, making some reasonable assumptions, a model has been built and the $\overline{d}$ inelastic cross section has been parametrized on the base of the existing experimental data on $\overline{p}d$ collisions.

A set of selection criteria minimally dependent on MC has been studied and refined in order to maximize the AMS-02 acceptance to antideuteron signal and conversely minimize the background both in the TOF low energy range, where primary flux is expected, and in the RICH region, where the secondary flux, coming from standard astrophysical sources,

is distributed. All the main possible sources of background, namely protons, deuterons, antiprotons and electrons have been considered.

Although greater MC statistics are required to make a more careful estimation of the AMS-02 background rejection power, because of the larger abundance of the other CR species with respect than that of the antideuterons, the following conclusion can be drawn.

The AMS-02 experiment will be able to provide clean samples of antideuterons in the energy ranges between 0.2 and 1.2 GeV/n and from 2.1 up to 4.1 GeV/n.

In the energy range between 0.2 and 0.8 GeV/n, AMS-02 will be able to detect primary antideuterons if their flux is greater than 5–6×10^{-7} $(\mathrm{m}^2$ s sr GeV/n$)^{-1}$.

Accordingly to that, taking into account the primary antideuterons fluxes published in literature, derived in the Minimal Super Symmetric Model framework making some standard assumptions on the halo density profile and neutralino annihilation cross section, and chosing some points in the supersymmetric parameter space, about 2 events are expected at most to be collected from AMS-02 in 3 years. Since the present uncertanties related to antideuteron primary flux are substantial, mainly due to the fact that the sources of primary fluxes are located inside the diffusive halo, whose size is unknown, this flux can be larger than that considered in this thesis.

Thanks to the predicted depletion of the secondary antideuteron spectrum below 1 GeV/n, even the detection of one antideuteron in this region would be a strong signal for the existence of new primary sources.

Bibliography

[1] Malcolm S. Longair. *High Energy Astrophysics*, volume 1, 2. Cambridge University Press, 2 edition, 1992, 1994.

[2] W-M Yao et al. Review of Particle Physics. *Nucl. Part. Phys.*, 33, 2006.

[3] R. L. Golden et al. *Phys. Rev. Lett.*, 43, 1979.

[4] K. Yoshimura et al. *Phys. Rev. Lett.*, 75, 1995.

[5] J. W. Mitchell et al. *Phys. Rev. Lett.*, 76, 1996.

[6] M. Boezio et al. *ApJ*, 487, 1997.

[7] H. Matsunaga et al. *Phys. Rev. Lett.*, 81, 1998.

[8] S. Orito et al. *Phys. Rev. Lett.*, 84, 2000.

[9] P. Maestro. *Indirect Search for Dark Matter by measurements of the cosmic rays positron spectrum with the AMS-02 experiment*. Phd thesis, Universitá degli studi di Siena, September 2003.

[10] D. Casadei and V. Bindi. The Origin of Cosmic Ray Electrons and Positrons. *ApJ*, 612:262–267, 2004.

[11] M. Boezio et al. *ApJ*, 532, 2000.

[12] M. A. Duvernois et al. *ApJ*, 559, 2000.

[13] D. Maurin et al. Galactic Cosmic Ray Nuclei as a Tool for Astroparticle Physics. *arXiv:astro-ph/0212111*, 2002.

[14] R. Duperray et al. Flux of light antimatter nuclei near earth, induced by Cosmic Rays in the Galaxy and in the atmosphere. *Phys. Rev. D*, 71, 2005.

[15] F. Zwicky. *Helvetica Physica Acta*, 6:110, 1933.

[16] P. Salucci E. Corbelli. The Extended Rotation Curve and the Dark Matter Halo of M33. *astro-ph:9909252*, 1999.

[17] J. Oort. *Bull. Astr. Inst. Netherlands*, 6:249, 1932.

[18] J.P. Ostriker and P.J.E. Peebles. *ApJ*, 186:467, 1973.

[19] V.C. Rubin and W.K. Ford. *ApJ*, 159:925, 1970.

[20] C.L. Bennett et al. Cosmological Constraints from the SDSS Luminous Red Galaxies. *ApJ Suppl. Series*, 148, 2003.

[21] M. Tegmark et al. Cosmological Constraints from the SDSS Luminous Red Galaxies. *astro-ph:0608632*, 2006.

[22] L. Bergstrom. Non-Baryonic Dark Matter: Observational Evidence and Detection Methods. *hep-ph/0002126*, 2000.

[23] G. Jungman et al. Supersymmetric dark matter. *Physics Reports*, 267, 1996.

[24] M. Drees. An introduction to Supersymmetry. *hep-ph:9611409*, 1996.

[25] J. L. Lopez et al. A Layman's Guide to SUSY GUTs. *hep-ph:9611409*, 1996.

[26] A. Bottino, F. Donato and N. Fornengo. Which fraction of the measured cosmic-ray antiprotons might be due to neutralino annihilation in the galactic halo? *Phys. Rev. D*, 58, 1998.

[27] L. Bergstrom et al. Cosmic antiprotons as a probe for supersymmetric dark matter? *astro-ph/9902012*, 1999.

[28] F. Donato et al. Antiprotons in cosmic rays from neutralino annihilation. *Phys. Rev. D*, 69, 2004.

[29] F. Donato, N. Fornengo and P. Salati. Antideuterons as a signature of supersymmetric dark matter. *Phys. Rev. D*, 62, 2000.

[30] P. Chardonnet, J. Orloff and P. Salati. The production of anti-matter in our galaxy. *Phys. Lett. B*, 409:313–320, 1997.

[31] C.J. Hailey et al. Development of the gaseous antipartcle spectrometer for space based antimatter detection. *Nucl. Inst. Meth. B*, 214:122–125, 2004.

[32] J. Alcaraz et al. Search for Antihelium in Cosmic Rays. *Phys. Lett. B*, 461:387–396, 1999.

[33] J. Alcaraz et al. Protons in near Earth orbit. *Phys. Lett. B*, 472:215–226, 2000.

[34] J. Alcaraz et al. Cosmic Protons. *Phys. Lett. B*, 490:27–36, 2000.

[35] J. Alcaraz et al. Helium in near Earth orbit. *Phys. Lett. B*, 494:193–202, 2000.

[36] A. Ahlen et al. An antimatter spectrometer in space. *Nucl. Inst. Meth. A*, 350: 387–396, 1994.

[37] A.W. Strong and I.V. Moskalenko. Propagation of Cosmic Rays Nucleons in the Galaxy. *ApJ*, 509:112–128, 1998.

[38] A. Jacholkowska et al. An indirect dark matter search with diffuse gamma rays from the Galactic Centre with the Alpha Magnetic Spectrometer. *Phys. Rev. D*, 74, 2006.

[39] B. Blau et al. The Superconducting Magnet System of the Alpha Magnetic Spectrometer AMS-02. *Nucl. Inst. Meth. A*, 518:139–142, 2004.

[40] M. Bourquin on behalf of the AMS Tracker Collaboration. The AMS tracking detector for cosmic-ray physics in space. *Nucl. Inst. Meth. A*, 541:110–116, 2005.

[41] B. Alpat et al. Charge determination of nuclei with the AMS-02 silicon tracker. *Nucl. Inst. Meth. A*, 540:121–130, 2005.

[42] P. Zuccon on behalf of the AMS Tracker Collaboration. The AMS Tracker Performance. *Proceedings of 29th ICRC, Pune*, 2005.

[43] D. Caraffini. *Anti-proton Flux Detection and Indirect Search for Dark Matter with the AMS-02 Experiment.* Phd thesis, Perugia University, 2004.

[44] M. Aguilar Benitez et al. The Ring Imaging Cherenkov detector (RICH) of the AMS experiment. *Proceedings of 29th ICRC, Pune*, 2005.

[45] P. Aguayo et al. Prototype study of the Cherenkov imager of the AMS experiment. *Nucl. Inst. Meth. A*, 560:291–302, 2006.

[46] T. Ypsilantis and J. Seguinot. Theory of ring imaging Cherenkov counters. *Nucl. Inst. Meth.*, 343:30–51, 1994.

[47] B. Baret et al. In-beam tests of the AMS RICH prototype with 20 A GeV=c secondary ions. *Nucl. Inst. Meth. A*, 525:126–131, 2004.

[48] P. Aguayo et al. The AMS-RICH Prototype: Test Beam Results. *Proceedings of IMTC, Como*, 2004.

[49] G. Carosi for the AMS collaboration. Positron/Proton Separation Using the AMS-02 TRD. *Nucl. Phys. B (Proc. Suppl.)*, 134:63–65, 2004.

[50] B. Dolgoshein. Transition Radiation Detectors. *Nucl. Inst. Meth. A*, 326:434–469, 1993.

[51] A. Bartolini et al. Integrated test of the TRD Gas System electronics. AMS-TRD Internal Note, March 6 2006.

[52] F. Cervelli et al. A reduced scale e.m. calorimeter prototype for the AMS-02 experiment. *Nucl. Inst. Meth. A*, 490:132–139, 2002.

[53] F. Cadoux et al. The AMS-02 electromagnetic calorimeter. *Nucl. Phys. B (Proc. Suppl.)*, 113:159–165, 2002.

[54] L. Girard et al. Performances of the AMS-02 eloctromegnetic calorimeter. *Proceedings for 8th ICATPP Conference*, 2003.

[55] F. Pilo. *Diffuse Gamma Ray emission detection with the AMS-02 electromegnetic calorimeter*. Phd thesis, Siena University, March 2005.

[56] L. Amati et al. The TOF counters of the AMS-02 experiment: space qualification tests and beam test result. *Nucl. Phys. B (Proc. Suppl.)*, 150:276–280, 2006.

[57] L. Baldini. I contatori e l'elettronica per la misura del tempo di volo dei raggi cosmici dell'esperimento spaziale AMS, March 1998.

[58] M. Salvadore. Esperimento AMS02:Il nuovo sitema di acquisizione dati del telescopio per il test dei contatori a scintillazione, October 2002.

[59] L. Brocco at al. Behaviour in strong magnetic field of the photomultipliers for the TOF system of AMS-02 space experiment. *Proceedings of 27th ICRC, Hamburg*, 2001.

[60] G.Levi et al. Simulation of the fine mesh photomultipliers in the TOF of AMS-02. *Proceedings of the ICATPP-2003 conference, Como*, 2003.

[61] Hamamatsu Photonics K. K. *PMT Handbook*, 1999.

[62] L. Quadrani on behalf of the AMS TOF Collaboration. Optimization of Time Of Flight of the AMS-02 experiment. *Proceedings of 29th ICRC, Pune*, 2005.

[63] M. Buénerd e I. Efthymiopoulos. A high energy secondary beam of ion fragments for instrumental tests at cern. *Technical report*, CERN-AB-2003-052-ATB, 2003.

[64] F. Giovacchini. Studio degli ioni intermedi nei raggi cosmici primari mediante la misura combinata di TOF e RICH di AMS-02, July 2003.

[65] A. Oliva. Riconoscimento di raggi cosmici con numero atomico $Z < 20$ con gli scintillatori plastici del sistema TOF di AMS-02., July 2003.

[66] D. Casadei. *Direct Measurement of galactic cosmic ray fluxes with the orbital detector AMS 02*. Phd thesis, Bologna University, March 2003.

[67] W.R. Leo. *Thecniques for Nuclear and Particle Physics Experiment*. Springer-Verlag, 1987.

[68] V. Bindi on behalf of the AMS TOF Collaboration. Time of Flight read out system of AMS-02 experiment. *Proceedings of 29th ICRC, Pune*, 2005.

[69] C.N. Chou. The Nature of the Saturation Effect of Fluorescent Scintillators. *Phys. Rev.*, 87:904, 1952.

[70] Carlo Gavazzi Space SpA. TOF Thermal Test Procedure. *Technical report*, RICSYS-PR-CGS-009, 2006.

[71] Philips Photonics. *Photomultiplier tubes - Principles and applications*, 1994.

[72] K. Wick et al. Recovery and dose rate dependance of radiation damage in scintillators, wavelength shifters and light guides. *Nucl. Inst. Meth. B*, 61:472–486, 1991.

[73] W. Busjan et al. Shortlived absorption centers in plastic scintillators and their influence on the fluorescence light yeld. *Nucl. Inst. Meth. B*, 152:89–104, 1999.

[74] S. Ilie et al. Radiation-Damage measurements on PVT-based plastic scintillators. *Nucl. Phys. B (Proc. Suppl.)*, 32:384–391, 1998.

[75] Z. Li et al. Properties of plastic scintillators after irradiation. *Nucl. Inst. Meth. A*, 552:449–455, 2005.

[76] L. Quadrani. *Assembly and space qualification of the scintillator detector LTOF for the AMS-02 spectrometer*. Phd thesis, Bologna University, 2007.

[77] P.A. Aamio. FLUKA Users Guide. *CERN Report*, TIS-RP-190, 1990.

[78] H.L. Bradt and B. Peters. The Heavy Nuclei of Primary Cosmic Radiation. *Phys. Rev.*, 77:54–70, 1950.

[79] R.K. Tripathi, F.A. Cucinotta and J.W. Wilson. Universal Parameterization of Absorption Cross Section. Technical report, NASA, December 1999.

[80] R.K. Tripathi, F.A. Cucinotta and J.W. Wilson. Medium modified nucleon-nucleon cross sections in a nucleus. *Nucl. Inst. Meth. B*, 152:425–431, 1999.

[81] F. Binon et al. Absorption cross-section of 25 GeV/c antideuterons in Li, C, Al Cu and Pb. *Phys. Lett. B*, 31(4):230–232, 1970.

[82] S.P. Denisov et al. Measurements of antideuteron absorption and stripping cross section at the momentum 13.3 Gev/c. *Nucl. Phys. B*, 31:253–260, 1971.

[83] S.P. Denisov et al. Experimental comparison of $\bar{d}$p and $\bar{p}$d totatl cross-sections. *Phys. Lett. B*, 34(2):167–169, 1971.

[84] T. Elioff. Antiproton-Nucleon Cross Sections from 0.5 to 1.0 BeV. *Phys. Rev.*, 128: 869–884, 1962.

[85] R. Bizzarri et al. *Nuovo Cim. A*, 22:225, 1974.

[86] Z. Ming Ma and G.A. Smith. Antiproton-Deuteron Elastic Scattering between 1.60 and 2.00 GeV/c. *Phys. Rev. Lett.*, 27:344, 1971.

[87] P.S. Eastman et al. A formation study of N$\bar{\text{N}}$ interactions between 1.51 and 2.90 GeV/c. Topological and reaction cross sections. *Nucl. Phys. B*, 51:29, 1973.

[88] H. Braun et al. Study of the Coherent $\bar{\text{p}}$d$\bar{\text{n}}$dπ^- Reaction at 5.55 GeV/c. *Phys. Rev.*, 8:2765, 1973.

[89] J.D. Sullivan. Geometrical factor and directional response of single and multi-element particle telescopes. *Nucl. Inst. Meth.*, 95:5–11, 1971.

[90] P. Zuccon. *A Monte Carlo simulation of cosmic rays interactions with the near Earth environement.* Phd thesis, Perugia University, October 2002.

[91] E. Choumilov. MC simulation of AMS02 level-1 trigger. AMS Internal Note, June 2001.

[92] V. Choutko. On the alignement of the AMS Si Tracker by means of charged particles. AMS Technical Note, January 4 1996.

[93] J. Alcaraz. An alternative track fitting method for AMS. AMS Internal Note, March 18 2003.

[94] Th. Siedenburg et al. A Transition Radiation Detector for AMS. *Nucl. Phys. B (Proc. Suppl.)*, 113:154–158, 2002.

[95] H. Fuke. Search of Cosmic-Rays Antideuteron. *Phys. Rev. Lett.*, 95:081101, 2005.

[96] G.D. Badhwar et al. Validation of the galactic cosmic ray and geomagnetic transmission models. *Radiat Meas.*, 33:361, 2001.